INVESTIGATION ON ADVANCED INTERACTION STRUCTURES FOR MILLIMETER WAVE AND SUB-THZ VACUUM ELECTRON DEVICES

A

Thesis submitted

in Partial Fulfilment of the Requirements

for the Degree of

Doctor of Philosophy

by

Narugopal Nayek

Department of Electronics and Electrical Engineering
Indian Institute of Technology Guwahati
Guwahati - 781039, Assam, India
April 2022

In hopes that this work may contribute to future research,

this work is dedicated to all researchers.

Certificate

This is to certify that the thesis entitled “**Investigation on Advanced Interaction Structures for mm Wave and sub-THz Vacuum Electron Devices**", submitted by **Narugopal Nayek** bearing registration number 166102104, a research scholar in the *Department of Electronics and Electrical Engineering, Indian Institute of Technology Guwahati*, for the award of the degree of **Doctor of Philosophy**, is a record of an original research work carried out by him under our supervision and guidance. The thesis has fulfilled all requirements as per the regulations of the institute and in our opinion has reached the standard needed for submission. The results embodied in this thesis have not been submitted to any other University or Institute for the award of any degree or diploma.

Dr. Ramesh Kumar Sonkar
Dept. of Electronics and Electrical Engg.,
Indian Institute of Technology Guwahati,
Guwahati - 781 039, Assam, India.
Date:
Place: Guwahati

Prof. Ratnajit Bhattacharjee
Dept. of Electronics and Electrical Engg.,
Indian Institute of Technology Guwahati,
Guwahati - 781 039, Assam, India.
Date:
Place: Guwahati


भारतीय प्रौद्योगिकी संस्थान गुवाहाटी
Indian Institute of Technology Guwahati

Acknowledgements

First and foremost, I would like to express my deepest and most sincere gratitude to my supervisors Prof. Ratnajit Bhattacharjee and Dr. Ramesh Kumar Sonkar, for their continuous support of my Ph.D. study and research, for their patience, motivation, enthusiasm, and guidance. Their kindness, dedication, hard work, and attention to detail helped me in all the time of research, publishing research papers, and writing of this thesis. I could not have imagined having better supervisors and mentors for my Ph.D. study.

Besides my advisor, I am also thankful to my Doctoral Committee members Prof. Rakhesh Singh Kshetrimayum, Dr. Mahima Arrawatia, Dr. Nallam and Dr. Debabrata Sikdar for their encouragement, suggestions, and feedback.

My sincere thanks also go to the Head of the Department and other faculty members for their kind help in carrying out this work, including all the members of the research and technical staff of the department.

I would like to thank my parent organization, Society for Applied Microwave Electronics Engineering and Research (SAMEER), for permitting me to pursue for the doctoral studies.

My deepest gratitude to Dr. Sulabha Ranade, former Director General of SAMEER for her kind support and motivation.

My sincere thanks also goes to Dr. T Tiwari, Program Director of SAMEER, Guwahati, for his continuous support and motivation.

I thank my present and former fellow colleagues, Dr. Sandeep Vyas, Dr. Mohit Kr. Joshi, Mr. Manoj Kr. Phatangare, Mr Arvind Naik, Mr. Nandan Gowshami, Mr. Narendra Singh Shekhawat, Dr Darpan Mishra, Dr Akash, Mrs Prajna, Mrs Anil Patibandla and Dr Arjun Kumar, who have suggested and discussed research topics and helped me remain motivated. Particularly the contribution of Mr. Arvind Naik and Mr. Nandan Gowshami for fabricating and characterizing the width-modulated structure is unforgettable.

I would like to thank my parents Mr. Kashinath Nayek and Mrs Hira Nayek, for giving birth to me and instil me the requisite values in life which help me reaching where I am today.

My sincere gratitude goes to in laws Mr. Dwijendranath Kundu and Mrs Sandhya Kundu for their continuous motivation and encouragement throughout the tenure.

It is impossible for me to write the name of all the individuals who have helped me (both directly and indirectly) during my Ph.D., and for that, I apologize.

My deepest gratitude goes to my wife Rituparna for supporting me throughout this journey and bearing all the pain in her smiling face. Without her support and encouragement it would not have been possible to carry out the thesis work.

Last, but not least, I would like to thank my daughter Miss Aaditri, playing with her in the evening rejuvenates me to complete the all pending works. Love you my child.

(Narugopal Nayek)

Abstract

Vacuum Electron Devices (VEDs) find numerous applications due to their inherent merits, such as unmatchable output power, ruggedness, higher gain, and less heat generation at the junction in comparison to its solid-state counterparts. Traditional VEDs using a linear electron beam suffer from a severe decrease in power level as the operating frequency increases. The issues like unwanted reflection from the interaction structure, and, beam-wall interception become more predominant in sub-THz and THz frequency range. The magnetic focusing and cooling become more stringent at elevated frequency range. Therefore, various beam wave interaction mechanism is being explored by the researchers to develop highly efficient, powerful mm-wave, sub-THz, and THz radiation sources to tackle the above problem. Efforts are being made to design and develop novel interaction structures, efficient multi stage depressed collector, and high electron density electron gun etc. This thesis reports the study and design of a highly efficient medium power gyrotron for material processing application. The key subsystems of the gyrotron, such as, Magnetron Injection Gun (MIG), cavity, depressed collector and magnet system are studied. Two dimensional and three dimensional electro-magneto static simulations are carried out to optimize a MIG with minimum velocity spread. The output power of the gyrotron is obtained by using single mode time dependent approach. Particle-in-cell simulation is carried out to calculate and optimize various output parameters of the device. The mode competition in gyrotron is predominant as the device makes use of an over-moded interaction structure. An innovative interaction cavity is introduced to eliminate mode competitions for the operating TE_{02} mode. A three-staged depressed collector is employed to realize a high efficiency.

The thesis also reports study and design of wide-band sine waveguide (SWG) travelling wave tubes (TWT) at 0.22 THz and 0.65 THz. Various cold parameters are evaluated and optimized for a width modulated two-section SWG structure to obtain higher value of interaction impedance in comparison to conventional SWG structure. Higher gain per unit length is obtained in comparison to the other TWT's designed in this frequency band. The interaction structure is designed in two sections to reduce the reflection of RF power at the input coupler.

A truncated SWG structure is considered for 0.65 THz. The interaction impedance is evaluated at various points of beam tunnel area to choose rectangular beam of suitable aspect ratio.

Contents

List of Figures

List of Tables

List of Acronyms

2D	Two Dimension
2S	Two Section
3D	Three Dimension
AC	Alternating Current
BWO	Backward Wave Oscillator
°C	Degree Celsius
cm	centimeter
CNC	Computer Numerical Control
CW	Continuous Wave
CST	Computer Simulation Technology
CVD	Chemical Vapour Deposition
dB	Decibel
DC	Direct Current
DCWG	Double Corrugated Waveguide
DCWTWT	Double Corrugated Waveguide Travelling Wave Tube
DNP	Dynamic Nuclear Polarization
DNP-NMR	Dynamic Nuclear Polarization nuclear magnetic resonance
DRIE	Dry Reactive Ion Etching
DUT	Device Under Test
ECCD	Electron Cyclotron Current Drive
ECRH	Electron Cyclotron Resonance Heating
ECRM	Electron Cyclotron Resonance Maser

EDM	Electro Discharge Machining
EIK	Extended Interaction Klystron
EM	Electromagnetic
eV	Electron-volt
FWGTWT	Folded Waveguide Travelling Wave Tube
FWS	Fast Wave Structure
FFT	Fast Fourier Transform
GHz	Gigahertz
HFSS	High Frequency Structure Simulator
keV	Kilo Electron-Volt
LHCD	Lower Hybrid Current Drive
LIGA	Lithographie, Galvanoformung, Abformung
MB	Multi Beam
MIG	Magnetron Injection Gun
mm	millimeter
mm Wave	millimeter Wave
mW	milli-Watt
MW	Mega-Watt
ns	nanosecond
OFHC	Oxygen Free High Conductivity
PBG	Photonic Band Gap
PIC	Particle-in-Cell
PNA	Programmable Network Analyzer
PPM	Periodic Permanent Magnet
Q-factor	Quality factor
QOMC	Quasi-Optical Mode Converter
RADAR	Radio Detection and Ranging

RF	Radio Frequency
RLSWG	Ridge-Loaded Sine Waveguide
SB	Sheet Beam
SBD	Sheet Beam Device
SOC	Start Oscillation Current
SS	Single-Section
SWG	Sine Waveguide
SWS	Slow Wave Structure
TE	Transverse Electric
THz	Terahertz
TM	Transverse Magnetic
TWT	Travelling Wave Tube
UV	Ultra Violet
VED	Vacuum Electron Device
VNA	Vector Network Analyzer
VSAR	Video Synthetic Aperture Radar
μm	micro meter

List of Symbols

Δv	Velocity spread
e	Charge of electron
f_m	Magnetic compression ratio
Ψ	Work function
σ_D	Conductivity of the un-machined or smooth surface
p_c	Complex transverse momentum of the electron normalized to its initial absolute value
dz	Integrating a function with respect to the "z"
N_{el}	Number of electrons used in the single mode time dependent approach
R_0	Radius of the straight section of the gyrotron cavity
R_b	Radius electron beam
U_c	Beam voltage
m_e	Mass of electron
α	Beam velocity ratio
$\approx$	Approximately
β	Fundamental axial phase constant
$\beta_{\perp 0}$	Normalized electron velocity in the transverse direction
β_n	Axial phase shift constant of the n^{th} space harmonic
$\triangle$	Normalized cyclotron frequency mismatch

$\delta(z)$	Normalized frequency mismatch
Δf	3 dB bandwidth
Δh	Incremental width of the truncated cone (virtual cathode)
Δr	Incremental radius of the truncated cone (virtual cathode)
Δv	Velocity spread
δ_s	Skin depth
δ_t	Delay or time taken for the output power of gyrotron to obtain saturated value
ϵ_0	Permittivity of free space
ϵ''	Microwave power absorption coefficient
η	Electronic efficiency
η_c	Efficiency with depressed collector
η_{el}	Electron compression efficiency
γ	Relativistic factor
λ	Wave length
μm	Micro meter
μ	Normalized length of the interaction region
ν_{mp}	p^{th} root of the derivative of m^{th} order Bessel's function
ω	Angular frequency of RF wave
Ω_0	Cyclotron frequency
ω_{cut}	Cutoff angular frequency of the resonator
ω_{cyc}	Electron cyclotron frequency
ϕ	Phase in radian
ϕ_1	Input taper angle
ϕ_2	Straight taper angle
ϕ_3	Output taper angle
ϕ_c	Angle of slant surface of cathode with respect to axis
σ_{cu}	Conductivity of OFHC copper

σ_{eff}	Effective conductivity of the machined surface
τ	dimensionless or Normalized time
θ	Emission angle with respect to cavity axis
$\times$	Times (Sign of multiplication)
υ	Total velocity of emitted electron from virtual cathode
υ_a	Axial velocity of emitted electron from virtual cathode
υ_r	Radial velocity of emitted electron from virtual cathode
ς	Dimensionless longitudinal coordinate z
ϑ_g	Group velocity
^{0}	Degree
m, k	Azimuthal and radial mode numbers
m_e	Mass of electron
A	Ampere
a	Broader dimension of rectangular waveguide for SWG TWT
ah	Width-modulation amplitude
B	Magnetic field at cavity region
b	Narrower dimension of rectangular waveguide for SWG TWT
B_0	Applied magnetic field
B_c	Magnetic field at cathode
c	Velocity of light in free space
Cu	Symbol of copper
d	Narrower dimension of rectangular waveguide for truncated SWG TWT
D_{ac}	Distance between cathode and first (modulating) anode
d_s	Depth of the slot of slotted cavity of gyrotron
e	Charge of electron
E_n	Electric field
$E_{z,n}(0)$	On-axis longitudinal electric field of the space harmonic

f	Frequency
f_{c0}	Centre frequency
f_0	Initial RF field profile vector
$freq_{opt}$	Optimal frequency of the RF field
G_f	Gap factor
h	Amplitude of sine-wave profile for SWG TWT
h_s	RMS height of the surface
I_b	Beam Current
j	Imaginary number
$J'_m(x)$	Derivative of m^{th} order Bessel function
J_c	Emission current density
J_T	Current density
k	Boltzmann constant
$k_\perp$	Characteristic transverse wave number
k_n	Interaction impedance
k_z	Axial wave number
k_{zend}	Wave factor at the end of the resonator
L	Length of straight section of the cavity
n^{th}	Denoting an unspecified member of a series of numbers or enumerated items
P	Power flow through the structure
p	Length of a single Period of SWGTWT
P_0	Output power of gyrotron
P_a	Power absorbed per unit volume
P_{out}	Output power of TWT
P_r	Reflected power

$R(z)$	Radial profile of the cavity
R_b	Beam radius at cavity
R_0	Radius of straight section of the cavity
r_c	Mean radius of cathode
R_e	Radius of the electron beam
R_L	Larmor radius
r_{lc}	Larmor radius at cathode
s	Harmonic number
S_{11}	Return loss
S_{21}	Insertion loss
T	Temperature
t	Thickness of beam tunnel for truncated SWGTWT
t_{di}	Thickness of the dielectric
T_c	Cathode temperature
$v_{\perp 0}$	Velocity in the transverse direction
V_0	Beam voltage
V_a	Accelerating voltage
v_p	Axial phase velocity
v_r	Radial velocity of the electron beam
v_z	Axial velocity of the electron beam
w	Angular frequency of the RF wave
W	Stored energy per unit length

w_c	Cyclotron frequency of electron
w_s	Width of the slot of slotted cavity of gyrotron
z	Axis vector
%	Percentage
BW	Bandwidth
C_{mp}^2	Beam-wave coupling coefficient
G.p.U	Gail per unit length
GHz	Gigahertz
I_{soc}	Start oscillating current
kV	Kilovolt
kW	Kilowatt
P	Input power
P_{eff}	Effective input power
P_{mm}	Mm-wave power output
P_r	Total beam power recovery
P_{r1}	Beam power recovery at electrode-1
P_{r2}	Beam power recovery at electrode-2
P_{r3}	Beam power recovery at electrode-3
P_{sp}	Spent beam power
Pf-1s	Forward powers of one-section TWT structure
Pf-2s	Forward powers of two-section TWT structure
Pr-1s	Reflected powers of one-section TWT structure
Pr-2s	Reflected powers of two-section TWT structure
Q_{diff}	Diffractive quality factor
T	Tesla
V	Beam Voltage
W	Watt

Physical Constants

c	2.99792458×10^{8} m.s^{-1}
ϵ_0	$8.85418781 \times 10^{-12}$ F.m^{-1}
k	1.380649×10^{-23} J.K^{-1}
m_e	$9.1093837 \times 10^{-31}$ kg
π	3.141592653
e	$1.602176634 \times 10^{-19}$ C

List of Publications

Journal Publications

1. **N. Nayek**, M. K. Joshi, R. K. Sonkar, T. Tiwari, and R. Bhattacharjee, "Design and analysis of width-modulated two-section sine waveguide for G-band traveling wave tube," *IEEE Transactions on Electron Devices*, vol. 68, no. 12, pp. 6458-6464, Dec. 2021, doi: 10.1109/TED.2021.3117894.
2. **N. Nayek**, M. K. Joshi, R. K. Sonkar, T. Tiwari and R. Bhattacharjee, "Design and efficiency enhancement of a Ka-band industrial gyrotron," *IEEE Transactions on Plasma Science*, vol. 48, no. 11, pp. 3807-3814, Nov. 2020, doi: 10.1109/TPS.2020.3026696.
3. **N. Nayek**, R. K. Sonkar, T. Tiwari and R. Bhattacharjee, "Design and analysis of truncated velocity tapered sine-waveguide structure for traveling-wave tube in THz-band," IEEE Transactions on Plasma Science, vol. 50, no. 11, pp. 4759-4766, Nov. 2022, doi: 10.1109/TPS.2022.3211740.

Conference Publications

1. **N. Nayek**, M. K. Joshi, R. K. Sonkar, T. Tiwari and R. Bhattacharjee, "Design of truncated sine-waveguide structure for THz TWT," *2021 22nd International Vacuum Electronics Conference (IVEC)*, 2021, pp. 1-2, doi: 10.1109/IVEC51707.2021.9722470.
2. **N. Nayek**, R. Sonkar, M. K. Joshi, T. Tiwari, and R. Bhattacharjee, "H-plane loaded sine waveguide TWT in G-band," *IEEE Asia-Pacific Microwave Conference (APMC)*, 2019, pp. 1250-1252, doi: 10.1109/APMC46564.2019.9038322

3. **N. Nayek**, Ramesh Kumar Sonkar, and Ratnajit Bhattacharjee, ”Elimination of mode competition in TE_{0n} mode gyrotron,” *41st Photonics Electromagnetics Research Symposium (PIERS 2019)*, Rome, Italy, 17 - 20 June 2019

Other Publications not Included in the Thesis

1. **N. Nayek**, A. Naik, Manoj Phatangare, and T. Tiwari, “Development of MW sower S-band circulator for high energy linear accelerator” *DAE-BRNS International Symposium on Vacuum Science and Technology and its Application in Accelerators (VSTAA-2022)* , 16-19 February, 2022.

   N. Nayek received Shakuntala Bai Byabaharik Medals for the best poster awards for this paper.

2. **N. Nayek**, A. Naik, Manoj Phatangare, and T. Tiwari, “Design and development of high power S-band ferrite based RF load” *DAE-BRNS International Symposium on Vacuum Science and Technology and its Application in Accelerators (VSTAA-2022)*, 16-19 February, 2022.

3. **N. Nayek**, A. Naik, M. Phatangare, and T. Tiwari, “Design and development of high power broad band dry RF load”, *Defence Science Journal*, vol. 71, no.03, pp. 315-319, 2021, doi. https://doi.org/10.14429/dsj.71.16834

4. E. Radhika, **N. Nayek**, T. Tiwari, and D. Pamu, “Development and design of aluminium nitride disc for high power S-band dielectric window”, *Open Ceramics*, vol 8, 2021.

5. M. K. Joshi, **N. Nayek**, T. Tiwari, J. Pidanic, Z. Nemec, and R. Bhattacharjee, "Multiphysics and multipactor analyses of TE_{022} mode high power X-band RF window," *IEEE Microwave and Wireless Components Letters*, vol. 30, no. 3, pp. 272-275, March 2020, doi: 10.1109/LMWC.2020.2971652.

6. M. K. Joshi, **N. Nayek**, T. Tiwari, and R. Bhattacharjee, "Design and analysis of overmoded RF window for high power applications in X-band," *IEEE Transactions on Plasma*

Science, vol. 48, no. 1, pp. 127-132, Jan. 2020, doi: 10.1109/TPS.2019.2956763.

1

Introduction

Contents

1.1 Introduction

The modern era of human civilization demands a bit excessive microwave power and frequency for various civilian and strategic applications [1]- [9], such as, high-resolution imaging, spectroscopy, RADAR, remote sensing, space observation, high-speed data communications, electron cyclotron resonance heating [10] and processing of advanced materials [11]- [14]. The solid-state devices with group III–V semiconductors can produce only few hundred mWs of power in mm-wave band, which are inadequate for practical applications [15]- [16]. On the other hand, Vacuum Electron Devices VEDs can conveniently expands it horizon of both power and frequency either by changing the operation mechanism or by employing advance interaction structure. Vacuum electron Devices (VEDs) [17]- [18] utilize convection current generated by using a DC power source in vacuum atmosphere to generate or amplify RF power. There are various types of VED, such as, triodes, linear beam tubes, backward wave devices, cross field devices and gyro devices. A VED consists of an electron gun, an interaction structure, a magnetic focussing system, RF input and output couplers, and a collector [18]. The electron gun produces electron beam with desired shape and current density. The electron beam is injected into the interaction structure. The interaction structure may either be a slow wave structure (SWS) or a fast wave structure (FWS) depending on the operation mechanism. The magnetic focussing system focuses the electron beam, allowing it to travel in a desirable manner through the interaction structure. RF power of the appropriate frequency is injected through the input coupler onto the interaction structure for the case of an amplifier. The output coupler collects the RF power output. However, there is no RF input for vacuum electron RF sources. The electron beam in Travelling Wave Tube (TWT) is generated to travel with the RF signal at similar speed to have an interaction between them. The amplification in the RF signal takes place due to the energy transfer from the electron beam to the electromagnetic wave. As the name suggest, the role of collector is to collect the spent electron beam efficiently and dissipating the remaining energy. Gyrotron [19]- [21] is a cross field microwave tube which comes under fast wave vacuum electron tubes family. It is a high power, millimetre wave source capable of producing MW level power from centimetre wave to THz frequency range. The output power of mm wave gyrotron can be two to three order higher than linear beam tubes. Gyrotron employs a truncated conical cathode and a hollow cylindrical anode to produce hollow spiralling electron beam which travels through an open-ended waveguide cavity emerged in a strong magnetic field for beam–wave interaction. An applied magnetic field makes the electron beam gyrate at a cyclotron frequency close to eigen mode frequency of gyrotron for energy transfer from electron beam to RF field. Interaction structure of gyrotron can be made bigger even at higher frequency by operating it in higher-order modes. Therefore, it is capable of producing high power at high frequency. Gyrotron has got numerous applications in various technologies as the device can operate in a wide range of frequencies and power level. On the other hand, Travelling Wave Tube (TWT) [17]- [18] is a linear beam tube which has a periodic interaction structure where continuous beam–wave interaction takes place. TWT is a popular choice due to its unmatched linearity and wideband operation. However, at mm-wave or sub-THz frequency, the conventional TWT with helix Slow Wave Structure (SWS) is impractical as the helix becomes too thin and fragile to fabricate. Therefore, the TWTs, comprising of all-metal SWS, such as folded waveguide TWT (FWGTWT) [22], double-corrugated waveguide TWT (DCWTWT) [23], and sine waveguide TWT (SWGTWT) [24] are better solutions as they are not only realizable but also capable of handling much higher power in this frequency range. Among which, sine waveguide slow wave structure (SWGSWS) is the simplest interaction structure to fabricate as the same can be fabricated by means of a nano-CNC or CNC wire electro-discharge machining (EDM) technique. SWGSWS structure is basically a rectangular waveguide whose axis follows a sinusoidal path. Some modifications in the SWGSWS are incorporated to enhance the interaction impedance or to reduce attenuation in the structure which are extremely critical at elevated frequency.

1.2 High Power mm-Wave Devices

In the recent past, the development of high power mm-wave and sub-THz devices are driven by various applications, such as, communication technology, high resolution radar, magnetic resonance imaging, electron cyclotron resonance heating, table-top accelerators and radiation sources, plasma and material processing. The development of the VEDs at elevated frequencies has also been facilitated by advancement of both (a) numerical codes like CST [25], HFSS [26], Magic [27], etc. and (b) various advanced fabrication techniques like UV and deep x-ray lithography (LIGA), electro-discharge machining (EDM), diffusion-bonding, laser cutting, deep reactive ion etching (DRIE), etc. The dimensions of the interaction structure of linear beam tubes are dependent on frequency as they operate in fundamental mode. As the frequency goes high, the dimensions shrink. In order to have higher operating power at higher frequency, the interaction structure of TWT has been changed from conventional helix to all metal waveguide SWSs. On the other hand, the dimension of interaction structure of a gyro devices can be kept bigger at higher operating frequencies as the device is operated at higher order modes. Therefore, they can produce MW of power at THz band. The various THz VEDs are described in the literature review section.

1.3 Challenges in Design and Development Vacuum Electron Devices in THz band

The major challenges in the THz band arises mainly due to dimensional shrinkage of the VEDs at high frequency regime. The various issues faced by VEDs in the THz regime are briefly described below:

1.3.1 Attenuation

At higher frequency, the RF current tends to flow through the surface area due to skin effect [28]. The surface resistance become very high as the RF current flow through a narrow cross sectional area. The non-ideal machining surface also causes hindrance to propagation of RF wave. The elevated frequency coupled with uneven surface reduce the effective conductivity of the metal structure. Therefore, the attenuation per unit length is very high at this frequency band.

1.3.2 Reflection

Reflection of RF power happens mainly due to impedance mismatch at the input and output ports. The impedance mismatch occurs due to machining tolerance and mechanical misalignment between parts of the RF circuit. A little misalignment at THz band become substantial due to small wavelength of the RF wave.

1.3.3 Fabrication of Miniature Parts

The conventional machining techniques are not compatible with miniature tooling required to accomplish the due tolerance, surface finish and accuracy at THz band. Nano CNC (Computer Numerical Control) with higher than 20,000 rpm spindle speed can provide resolution up to 0.1 um. Nano CNC is successfully applied to fabricate the SWS at 0.346 THz [29]. However, there is enormous challenge to fabricate the micron size tool required beyond this frequency [29]- [32].

The lithographic microfabrication process LIGA which is German acronym Lithographie, Galvanoformung, Abformung (Lithography, Electroplating, and Molding), can produce the moulds on which the copper structure is grown by electroforming. The VED structure can be conveniently fabricated using this process [29]. However, the process requires specialized skills.

The integration of parts for conventional VEDs are done by using brazing. However, brazing is avoided in THz band as the undesired flow or the excess quantity of brazing material alter the key dimensions of the interaction structure. Micro-diffusion bonding [33] is rather used to join the parts. The parts are stacked together and subjected to a specified pressure and temperature closed to the melting point of the metals. The right combination of temperature and pressure make a vacuum tight bond.

1.3.4 Generation of High Electron Density Beam

In order to exhibit amplification after overcoming strong attenuation in THz band, the device needs relatively higher beam current in comparison to VEDs at lower frequency. The requirement of higher beam current coupled with narrow beam tunnel area demands very high current density emitter which the pierce gun with conventional dispenser cathode cannot meet. A higher emission density and greater value of magnetic compression is needed to achieve sufficient beam current in spite of a thinner beam diameter. A strong magnetic focussing is required to overcome the repulsive force in the high current density beam. A beam diameter as low as 40-micron is demonstrated by using pierce gun in [34]. However, the SWS in THz band exhibits wide interaction field distribution. There are sufficiently strong longitudinal component of electric field exists away from the centre of the beam tunnel. Therefore, it is felt necessity to have a wider beam or sheet beam to achieve (a) high output power from the SWS having wide interaction field distribution and to (b) inject more current. The sheet beam focussing system is not as matured as cylindrical beam. The sheet beam suffers from diocotron (E×H) effect [35], [36] which causes undesired rotation of the beam. The beam rotation above a critical angle leads to beam-wall interception.

1.3.5 Thermal management

Thermal management is one of the most critical challenges faced in a VEDs of THz band. Higher attenuation in THz band leads to greater RF loss in the interaction structure. Magnetic circuits are placed very closed to the interact structure for beam focussing to satisfy the requirement of strong magnetic field, leaving hardly any place for the cooling channel. The beam interception, if any, causes more heating and makes the situation worse. The excessive heating causes thermal expansion of the structure and consequently the shift in operating frequency. The heating is also causes out gassing which degrades the vacuum atmosphere in the device. The thermionic electron gun and the collector are the two hot region of VEDs where the thermal management is even more critical.

1.3.6 Evacuation

The VEDs operate under ultra-high vacuum to prevent undesired collision between residual gasses and electron beam. The collision generates the positive ions which accelerates towards the cathode which is subjected to negative potential. This deteriorates the life of the cathode. The evacuation is a major challenge in a compact, high power THz VEDs. Its is difficult to create exhaust port for evacuation in the tiny structure. Due care is required to be taken so that the exhaust hole does not affect the RF structure. The photonic bandgap structure (PBG) is perforated in nature where evacuation is relatively easy. However, there are fabrication issues associated with VEDs in THz band having PBG interaction structure.

1.4 Promising VEDs at mm-Wave and THz band

The researchers have been continuously thrived to find out suitable structure which suits THz band operation. The interaction structures are evolved to eliminate the issues arise at elevated frequency. The helix interaction structure of TWT is changed to waveguide based SWS to have more surface area and large interaction volume to reduce the surface resistance and also to enhance power handling capability of the VEDs. Waveguide interaction structures also allow better heat dissipation. Various overmoded structures [37] are also examined to increase the interaction volume. The cross-filed gyro-devices make use of an open-ended waveguide cavity which supports higher order mode operation which allows larger interaction volume. Therefore, the gyro-devices [10] can produce MW of power at Sub-THz band. In this section, the cross-field device gyrotron and the linear beam tube TWT will be discussed.

1.4.1 Gyrotron

Gyrotron [19]- [21] occupies a vital position as a high power source in the THz band. Gyrotron is called a cross field microwave tube as the operating electric field, magnetic field and the direction of beam propagation are perpendicular to each other. It has the capability to produce megawatts of power even at higher frequencies and hence it has received enormous interest among the researchers. Gyrotron can produce two order higher output power in comparison to the linear beam tubes. The electron gun of gyrotron consists of a truncated conical cathode and a hollow cylindrical anode. The electron beam is emitted from the slant surface of the truncated cone to form a hollow spiralling electron beam. The beam is injected to an open-ended wave guide cavity that is emerged in a strong magnetic field. The electron beam gyrates due to applied magnetic field. The applied magnetic field causes the beam to gyrate at a cyclotron frequency closed to eigen mode frequency of the cavity for fruitful interaction between the electron beam and RF field. Gyrotron is capable of producing high power at high frequency due to having oversized cavity operating at higher order mode [19], [20]. Gyrotron has been employed in plasma physics for various applications, such as, Collective Thomson Scattering, Electron Cyclotron Current Drive (ECCD), Lower Hybrid Current Drive (LHCD), Electron Cyclotron Resonance Heating (ECRH) and non-Inductive Current Drive [9], [10], [38]- [40]. The gyrotrons in Sub-THz band is being utilized in Dynamic Nuclear Polarization–Nuclear Magnetic Resonance (DNP–NMR) spectroscopy applications [7], [41], [42]. A tuneable CW gyrotron in this band can greatly intensify the NMR signal in DNP-NMR spectrometer. Such gyrotrons are also used in bio-medical application including medical diathermy for treatment of cancers tumour [43], [44]. Sub-THz gyrotrons are also considered to have potential for detection of concealed radioactive materials [45], [46]. When radioactive material is concealed in a container, there will be high ion density in comparison to the normal space. Therefore, if the intense electromagnetic energy from a THz gyrotron is focused to a centimetre sized spot, it gives rise to arcing due to high ion density in the vicinity of concealed radioactive material. However, these gyrotrons are too bulky and expensive.

1.4.2 Gyrotron for Material Processing

The CW gyrotrons are being applied for mm wave processing of materials [11]- [14]. Resistive heating for sintering of material is less efficient process as the material is heated from the outside. Hence, the outer area gets heated up in the beginning and the heat transfers to the central region of material through conduction. The heat transfer process is very slow due to poor thermal conductivity of the ceramic material. The non-uniform heating of material results non-uniform material property. The longer process time leads to grain growth which is undesirable. The processing of materials using RF is superior process as the same provides temperature uniformity in quick time. As the frequency RF increases the temperature become more uniform. Therefore, the material processing with millimeter wave is even superior in terms of heating uniformity, lower grain growth and to be a lower temperature process when compared to microwave processing.

The power absorbed per unit volume (P_a) by a dielectric material [11] is given by (4.3)

$$P_a = \pi f \epsilon_0 \epsilon''(f,T)\,|E|^2 \tag{1.1}$$

where ϵ_0, $\epsilon''(f,T)$, f, and T are the permittivity of free space, microwave power absorption coefficient, frequency, and temperature, respectively. Therefore, the absorbed power is proportional to frequency, input power and microwave power absorption coefficient of the material.

It can be noted that the ϵ'' is a function of frequency and temperature. Hence, as the frequency increases, power absorption by a dielectric material is also increased which leads to heating of the material. At higher temperature ϵ'' is increased further, resulting more absorption of microwave power [11]. Therefore, the advanced low loss dielectric material can be sintered by mm-wave to bring out various exotic properties. However, the mm-wave processing of material will be lucrative provided the process become economic or cost effective. The device should operate at medium voltage, magnetic field and with high efficiency.

1.4.3 Various Sub-systems of Gyrotron

A gyrotron consists of various sub-systems, such as, Magnetron Injection Gun (MIG), beam tunnel, interaction cavity, internal Quasi-Optical Mode Launcher (QOMC), beam collector, magnet system and dielectric window. The schematic diagram of a gyrotron is shown in Fig. 1.1.

1.4.3.1 MIG

The heart of a gyrotron is MIG [47]- [49] which produces hollow spiralling electron beam. It comprises of a truncated conical thermionic cathode to emit electrons and hollow cylindrical anode to pass the electron beam towards the interaction region. The electrons are ejected from a slanting surface of cathode to have both radial and axial velocities. The radial velocity component causes the beam to gyrate whereas the axial velocity component accelerates the beam towards interaction region. There is a modulating anode placed between cathode and main anode for triode type MIG. Triode MIG is preferred to have better control over the beam parameters. Cathode is subjected to maximum negative potential whereas main anode is subjected at ground potential. The combination electrode shape and potential forms equipotential lines so

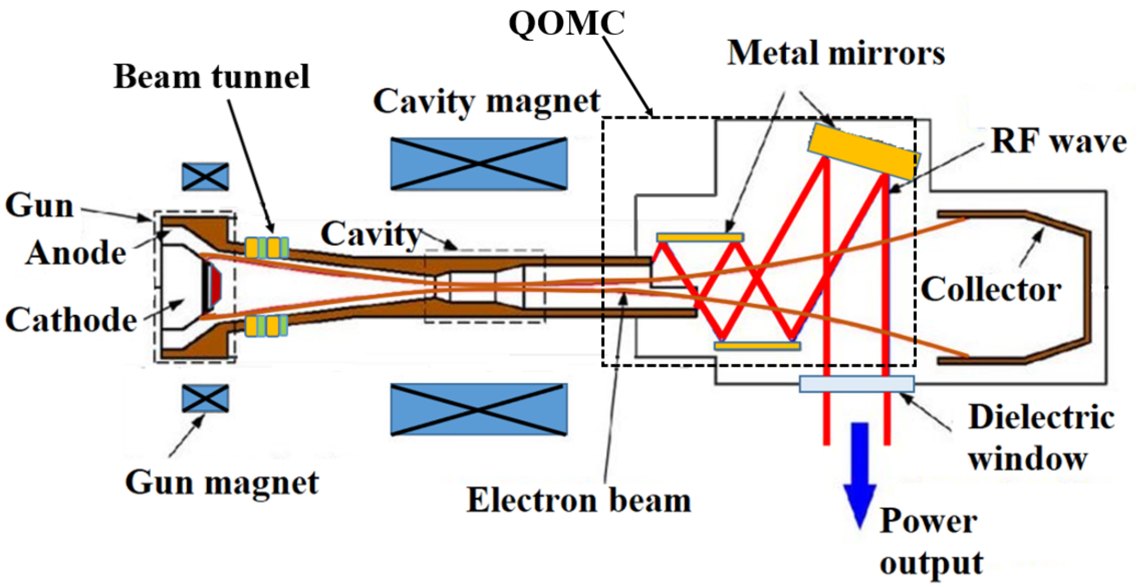

Fig. 1.1: Schematic diagram of a gyrotron.

as to focus the beam.

1.4.3.2 Beam Tunnel

Beam tunnel [50]- [52] is placed between MIG and cavity. Beam tunnel area is a stack of annular metals and lossy dielectric ring placed alternately. The primary aim of beam tunnel is to transport the beam from MIG to cavity without affecting its quality. The beam parameters of a gyrotron may get affected if the beam-wave interaction take place before the beam enters the cavity. The cyclotron frequency of the electron beam gradually increases in the beam tunnel area due to magnetic compression. The resonant frequency of beam tunnel should be different from the electron cyclotron frequency to avoid beam-wave interaction. The thermally conducting lossy dielectric is incorporated in beam tunnel to reduce the Q-factor so that the Start Oscillation Current ($I_s oc$) is increased. The chance of mode excitation is eliminated if the value of ($I_s oc$) is more than the beam current.

1.4.3.3 Cavity

The cavity [53]- [55] is the region where the beam-wave interaction take place. The cavity is a hollow cylindrical waveguide structure having three sections, such as down taper, straight section, and up taper. The beam-wave interaction occurs in the straight section. The diameter of the straight section is kept approximately equal to the cut-off diameter of the operating mode.

Therefore, the down taper does not allow the operating mode towards the gun region. The up taper is designed to partially couple out the RF power from the cavity. The eigen frequency of the operating mode and the cyclotron frequency of the electron beam are made close to each other. Gyrotron operates in Transverse Electric (TE) mode which interacts with the gyrating electrons for energy exchange from beam to field. The RF wave grows in the interaction cavity and come out of the structure radially or axially depending on the output structure of the tube.

1.4.3.4 QOMC

The internal quasi optical mode converter (QOMC) [56], [57] is placed after the cavity to extract the RF power radially from the device. QOMC is a vital component of gyrotron as is allows to separate out the RF section with the collector. This enables better thermal management in the tube. It consists of a launcher and sets of a metallic mirrors fabricated using Oxygen Free High Conductivity (OFHC) copper. The launcher is a spiral cut for TE_{mn} mode and step cut for axi-symmetric or TE_{0n} mode. The launcher radiates the higher order cavity mode towards the first mirror. There are periodic perturbation or dimple like structure in the launcher which converts the cavity mode to other modes, the superposition of which forms Gaussion like mode. The RF wave get reflected back and forth from the set of mirrors and finally emitted through a dielectric window. The mirrors are patterned for phase correction of the diffracted wave so that Gaussion or near Gaussion mode is produced at the output. The perturbation parameters and the mirror patterns are optimized for minimizing diffraction loss and improving mode conversion efficiency.

1.4.3.5 Collector

A collector [58]- [61] collects all the spent electrons safely. The magnetic field is decreased in the collector region so that the beam diameter is increased and finally collected at the collector surface. The spent electron beam has a wide energy spectrum. Therefore, it is a challenge to collect all the electron efficiently in the collector. The collector electrode is placed to collect the electron at grazing angle so that secondary electron emission is minimized. Collector is the hottest region of a gyrotron as the energized electrons strikes on the collector wall and cause lot of heating. It is important to collect the electron over a wide region to avoid excessive heat flux at a particular region. The collector electrodes are sometimes subjected to retarded potential in a depressed collector.

1.4.3.6 Magnet System

Magnet system [62]- [63] consists of a set of magnets and pole piece to guide the electron beam from cathode to collector. The magnets are mainly placed at gun, cavity and collector region. There should be uniform magnetic field in the region of electron emission to reduce the velocity spread. The uniform magnetic field at specified value at cavity is extremely important as the magnetic field determines the cyclotron frequency. In the collector region, the magnetic field is tailored to collect the electron beam over a wide area. Sometimes, sweeping coils are also used in the collector for this purpose. A time varying current is applied to the coil to vary the magnetic field over time.

1.4.3.7 Dielectric Window

The most critical and vulnerable component of a high power gyrotron is dielectric window [64]- [68]. The window allows the RF power to escape from the device with very low reflection while maintaining the vacuum atmosphere inside the tube. To realize a vacuum leak tight bakeable joint between dielectric and metal is the most challenging in the fabrication of dielectric window. The thickness of the dielectric is optimized to have enough mechanical strength and to provide smooth transmission of RF power. The dielectric material for a window should have the following properties: (a) low loss to absorb less power, (b) moderate dielectric constant to make the dimension less sensitive for reflection, (c) mechanically rugged to withstand differential pressure across the dielectric disk, (d) high thermal conductivity to dissipate the generated heat faster, and (e) easy join-ability to be able to make a reliable joint between the dielectric and metal.

1.4.4 Travelling Wave Tube

A Travelling Wave Tube (TWT) [17], [18], is a linear beam tube in which electron beam continuously exchange energy with the input RF wave. Since, it is not possible to achieve the

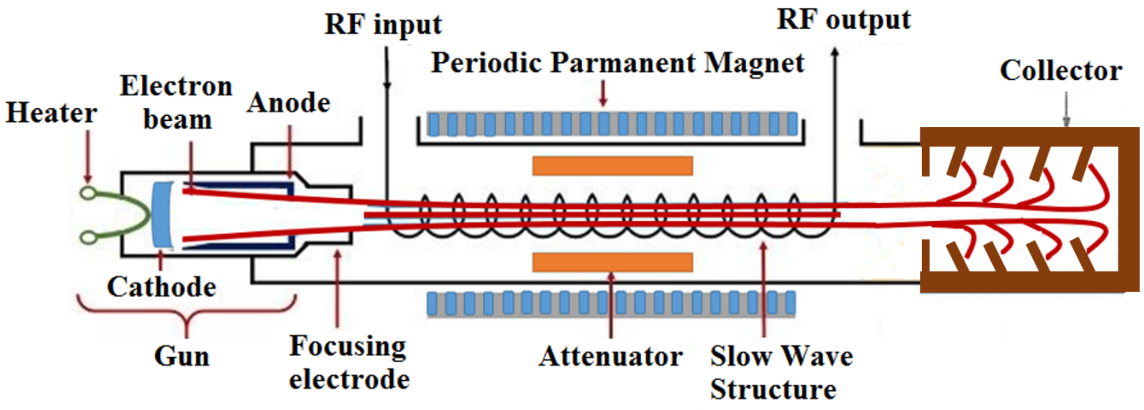

Fig. 1.2: Schematic diagram of a TWT.

electron velocity faster than the speed of light in vacuum, a Slow Wave Structure (SWS) is used to slowdown the velocity of RF wave. Shortly after world war II, the TWT was invented by Kompfner and Pierce independently in their respective country Britain and United States. They were not satisfied with the fleeting interaction structure in multi-cavity klystron. Therefore, they made use of the SWS to reduce the axial phase velocity of the RF signal. RF wave and electron beam can have prolonged interaction if they are with similar speed. Due to its low Q interaction structure, TWT is broadband device. TWT is extensively used as medium or high power amplifier. It has enabled several applications, such as, Radar, satellite communication, high data rate communication, electronic counter maser and defence. The schematic diagram of TWT is provided in Fig. 1.2.

The basic functional blocks of TWT includes an electron gun, the SWS, input and output couplers, magnetic focusing system, and collector. A Pierce type electron gun [69] is popularly used to generate a cylindrical electron beam. The electron gun consists of a cathode, beam forming electrode, and anode. It forms electron beam of desired shape and current density. The electrons are emitted from a spherically concave surface. Dispenser cathode are used in conventional TWT. The main constituent of dispenser cathode is porous tungsten. Barium compound is impregnated through the pore. The impregnated tungsten pallet acts as barium reservoir. When the cathode is heated, barium is migrated to the emission surface and forms a barium-oxide (BaO) mono-layer which reduces the work function. If the Bao layer evaporates after a certain time, it is replenished by the barium stored in the reservoir. It is very important to control the porosity of tungsten pallet to optimize and emission density and life of the cathode. The beam forming electron is placed at same potential as cathode which helps to give desired shape of the equipotential lines. The anode is placed at highest potential in the device to accelerate the electron towards the interaction structure. The beam is focussed to form a pencil beam.

Various kind of SWS is applied depending on frequency and applications. Helix SWS is the most popular at microwave frequencies due to its unmatched linearity, gain and bandwidth. However, at higher frequency, the dimension of the helix become too narrow to fabricate. The attenuation is also increased due to skin effect and subsequent surface loss in helix. Therefore, waveguide based SWSs are used in mm-wave and THz frequencies. The SWS is a periodic structure which makes the RF field to travel on a longer (helical, serpentine, etc) path thereby reducing the RF axial phase velocity. The velocity of electron beam is set at slightly higher than the phase velocity of the RF wave. The linear electron beam interacts with the axial RF field in the SWS. The electrons enter the SWS randomly and encounter the weak axial RF field produced by the input signal. The electrons, which face the accelerating phase, gain velocity as they receive energy from the RF field. On the other hand, the electrons facing the decelerating phase, loss their energy. Therefore, velocity modulation of electron beam takes place which leads to density modulation or formation of electron bunch. When the initial bunch arrives at the next period of the SWS, the RF phase at this region is such that it retards the bunch a bit further which helps to densify the bunch a little more. The electron beam and RF wave travels together and interacts continuously. The bunch become more and more pronounced at the output end simultaneously the RF wave grows to the maximum value.

A magnetic system is used to focus the electron beam from gun to collector. In TWTs, Periodic Permanent Magnet (PPM) is used to reduce the weight of the tube. PPM refers to the stack of permanent magnets and pole pieces attached in alternate fashion. The PPM acts like magnetic focusing lens placed periodically.

An input coupler is used to provide RF input to the device. On the other hand, the output coupler extracts the amplified output power. Both the couplers should be matched to minimize reflection. An attenuator is used in the SWS to suppress the backward wave in the tube as the generation of backward wave leads to oscillation which is undesirable.

The role of collector is to collect the spent electron beam safely and efficiently. A multistage depressed collector is used for increasing the efficiency of the tube.

1.4.5 Travelling Wave Tube in THz Band

There are various inherent merits of TWT that attracts the researchers to employ it at high frequencies. The output power of a Travelling Wave Tubes (TWT) can be 2 to 3 order greater than the power a solid state device can generate in the same frequency. TWT is also less sensitive to radiation and temperature fluctuations. There are various application areas people have envisaged in THz band which demands higher power out and broader bandwidth. Therefore,the need of developing a TWT in THz band has been arose for enabling various applications, such as, multi giga bits per second data rate satellite communication, wireless communication, plasma diagnostics, imaging, Video Synthetic Aperture Radar (VSAR) [70]- [74], etc. New fabrication tools, emerging technologies, design tools and new applications are fuelling a renaissance in high frequency TWTs.

1.5 Brief Review of Literature

Interaction structures of vacuum electron devices evolved since their inception. As the frequency increases, the dimensions of a linear beam tube shrink. Therefore, the surface loss increases, heat dissipation becomes a problem and as a result, power handling capability decreases. Therefore, researchers are exploring different modified version of interaction structures which can provide higher output power, broader bandwidth, increased efficiency, and higher frequency of operation etc. The different interaction structures reported by the previous researchers which suits for high frequency and high power operations are summarized below:

Gyro Devices

Gyro devices are cross field device which employs a truncated conical cathode and a hollow cylindrical anode to produce hollow spiralling electron beam which travels through an open-ended waveguide cavity emerged in a strong magnetic field for beam–wave interaction. The gyro devices can be broadly classified as source (Gyrotron) or amplifier (Gyro TWT, Gyro Klystron, Gyro Twystron, etc) [75]- [79]. The applied magnetic field in gyro devices makes the electron beam gyrate at a cyclotron frequency close to eigen mode frequency of the device for energy transfer from electron beam to RF field. Interaction structure of gyro devices can be made bigger even at higher frequency by operating it in higher-order modes. Therefore, they are capable of producing high power at high frequency.

Gyro klystron is a narrow band high gain amplifier which makes use of input, output and intermediate cavities. The input signal is fed at the input cavity in a particular mode. The gyro klystron is getting popular as a high power sub-THz source for radar as it operates in pulsed mode. In gyro TWT, continuous beam-wave interaction takes place in a dielectric loaded waveguide structure for amplification of wideband signals. The advantages of gyro klystron and gyro TWT are combined in Gyro twystron in which the input section is similar to gyro klystron and the out section is similar to a gyro TWT. Due to higher order mode operation, mode competition between the operating and the neighbouring modes are predominant in gyro devices.

Folded waveguide TWT (FWGTWT)

As the name suggest, in FWGTWT [22], [80], the interaction structure is a waveguide folded back and forth to realize the Slow Wave Structure (SWS). This type of TWT is conforms with mature cylindrical beam transportation technology as the structure supports cylindrical electron beam. It can withstand high power and has reasonable bandwidth. The interaction structure is also easy for construction and compatible with micro fabrication. Gain per period or interaction impedance of the structure is relatively low. Hence longer length is required to achieve high gain.

Groove-Loaded Folded Waveguide TWT

The gain per period value of FWGTWT is improved by providing additional rectangular groove in groove-loaded folded waveguide TWT [81], [82]. The groove itself acts as beam tunnel for sheet electron beam. In this structure, the axial electromagnetic fields exist in the groove region, which leads to higher interaction impedance and, subsequently, higher gain per unit length. This kind of structure provides less bandwidth in comparison to conventional FW TWT.

Multi beam (MB) FWG TWT

In Multi beam (MB) FWG TWT , multiple electron beams are simultaneously guided through a single FWG structure [83], [84]. Total beam current can either be multiplied by the number of beams to achieved higher output power or beam current may be distributed to multiple beams leading to low space charge effect. This type of tubes can also be operated in higher order modes like TE_{20}, TE_{30} etc. However, realization of electron gun and magnetic focusing with multiple beams are a major challenge.

Sheet beam (SB) Couple Cavity TWT

At millimetre wavelengths, there is a growing need for a small size and weight, high average power RF source. The sheet beam devices (SBD) ideally fit for many of these needs because they produce output power proportional to the beam width and reduced space charge effect [85]. The sheet beam conform with the wide interaction field in THz structure. It is also capable to provide the required current density of the device. Higher efficiency can be achieved due to the application of sheet electron beam. However, the focusing of sheet electron beam is a major challenge due to E × B or diocotron instability [35], [36].

Planar Helix SWS

The SWS is the vital part of TWT. The circular helix SWS is the most popular and widely used SWS. However, after a certain frequency, the dimension of circular helix of a conventional TWT becomes very small to realize. The fabrication of SWS will be cost effective provided printed-circuit or micro-fabrication techniques is adopted. This also eventually leads to miniaturization and low-cost mass production. Micro-fabrication techniques become important at high frequencies of operation where the dimensions become small. The fabrication and alignment becomes easy for planar helix SWS [86]- [87] in comparison to conventional helix SWS in the higher frequency regime. The thermal conductivity of CVD (chemical vapour deposition) diamond is approximately 5 times of copper. Hence, diamond supported helix [88] is also being developed for rapid heat dissipation.

Sine Waveguide TWT

Most of the SWS in THz band exhibits high transmission loss and strong reflection which is a serious problem. These problems severely prevent the existing devices from enhancing the power and expanding the bandwidth. In order to reduce the loss and reflection, a novel sine waveguide [24], [89], [90] interaction structure can be used. This kind of structure requires relatively higher voltage as the phase velocity reduction factor is less. A ridge-loading [91] on the SWG structure is done to increase the interaction impedance. This kind of structure is compatible with mature cylindrical beam as well as sheet beam.

Higher harmonic or frequency multiplier tubes

The input section of Higher harmonic or frequency multiplier tubes [92], [93] operates in fundamental harmonics whereas the output section operates in higher harmonics to provide frequency multiplication. In the input section, the beam velocity is modulated by the input signal. The electron beam enters into the drift tube and the velocity modulation is converted into density modulation. The beam bunch contains high harmonic current. The amplitude of higher harmonic current is controlled by adjusting the input power. Higher harmonic current induces higher harmonic electromagnetic wave and amplifies it in the output section. Thus, the high frequency millimetre wave is obtained with a low frequency millimetre wave as its driving source. Mode competition with fundamental harmonics is a concern for higher harmonic tubes.

Overmoded TWT

Typically, TWTs are designed to operate in the fundamental mode, but the power handling capabilities of these devices drops rapidly with frequency primarily due to the tiny interaction structure of the device. The small cavities lead to manufacturing difficulties and current limitations due to thin beam tunnel. If the TWT is operated in higher order mode [37], [94], [95], a larger cavity can be adopted which minimizes the difficulties associated with higher frequencies. The overmoded or oversized cavity allows a large beam tunnel for employing high beam current. Similarly, the requirement of magnetic field is not as stringent as in the case of fundamental mode. In addition, the oversized cavity can be directly machined with CNC milling instead of relying on nano-fabrication techniques. Mode competition with fundamental modes is a concern for overmoded tubes. The design of input output coupler is also a challenge for overmoded TWT.

Orotron

Orotron [96]- [98] was invented in 1960's, both theoretically and experimentally. The device is capable to produce 0.1-0.8 W of power up to 300 GHz band at relatively lower operating voltage. It is a resonant device which has the potential to generate power over THz band. Being a resonant device its bandwidth is relatively low. Orotron, can make use of pencil, sheet or hollow electron beams. Thin hollow beam can be used instead of sheet beam to increase the beam cross section and hence beam current and output power using oversized TM_{01}/TM_{02} cavity.

Clinotron

Although, gyrotron is the most powerful sources in THz band, it requires very bulky and expensive magnets that deters it from various applications particularly which requires low or medium powers. Clinotron [99]- [101] is an alternative source at THz band which is basically a modification of a resonant BWO with increased output power. Clinotron employs a thick electron beam which is slightly tilt with the axis. Higher output power is obtained due to thicker electron beam resulting higher beam current. The slow wave structure collects the electron beam as the beam is inclined fall on the SWS. It makes use of weakly inhomogeneous magnetic focusing field. Heating and subsequent dimensional change due to Beam interception in the SWS is an inherent problem associated with the clinotron. Efficient cooling mechanism is required to prevent the excessive heating.

Extended Interaction Klystron (EIK)

The Extended Interaction Klystron (EIK) [102]- [105] makes use of cluster of cavities instead of single cavity. It has got a multi-gap interaction cavity having high interaction impedance. Due to higher interaction impedance, the interaction length of EIK is short. Therefore, it allows to use a single period permanent magnet for focusing the electron beam. It is very compact and provides higher gain and broader bandwidth by combining the advantages of klystrons and traveling wave tubes. It can operate at millimetre-wave, sub-millimetre-wave or even in THz band. An EIK with sheet beam further provides several other advantages like higher peak power with lesser current density, reduced magnetic field for focusing of electron beam and reduced cathode loading. However, fabrication of EEK for mm wave, sub THz frequencies is a challenge due to its complicated structures. In addition, magnetic focussing is an issue associated with sheet beam. Folded-waveguide (FWG) resonant cavities is also tried as the same has mature fabrication technology in higher frequencies.

Double Corrugated waveguide TWT (DCW TWT

The all-metal DCW TWT [23], [106] is adopted as SWS by some research group to ease the fabrication challenges in THz frequencies. There are two rows of pillars in the rectangular waveguide structure. Electron beam is injected through the space between the rows of pillars. The axial field is concentrated in the central region of the SWS, where the beam is placed. The structure exhibits broad band properties and can be scaled up from mm wave to THz frequency. The structure has simple construction which can be fabricated using nano-CNC. However, micro fabrication technique is required for a frequency closed to 0.4 THz and beyond.

Photonic Bandgap (PBG) Structures

PBG [107]- [109] structure refers to the incorporation of engineered periodic materials to introduce appropriate electromagnetic band gap in the frequency band of interest and then introducing specific defects to break the periodicity of the lattice to allow certain band gap frequencies (defect states) to exist within the region of the defect. The fabrication challenges and power limitation of vacuum electron tubes at terahertz frequencies can be addressed by incorporating PBG material as a part of interaction structure. PBG structure enable larger beam tunnel and hence more beam current or relaxed magnetic focusing criterion. Thermal management issue can be successfully addressed due to larger space available in this kind of devices. At the same time, vacuum pumping also become easy as there are more areas available to the designer for creating vacuum channel. Fabrication difficulty at THz band is the main challenge to realize this kind of structure.

E- Plane and H- Plane loaded TWT

H-plane and E-plane loaded rectangular waveguide SWS [110] has received considerable interest for some research group. This kind of SWS incorporates an H-plane metal load in addition to the E-plane metal load in the straight rectangular waveguide. Due to an additional H-plane load, it exhibits enhanced value of interaction impedance and consequently higher gain per unit length of the device.

1.6 Thesis Motivation and Objective

From the survey of literature, the following areas has been identified for carrying out systematic study:

(a) Although, mm-wave processing of material is much more effective than cm-wave processing, the gyrotrons reported for industrial processing exhibits efficiency in the range of 30-40% [111], [112] without depressed collector. The efficiency is increased near about 60% with a depressed collector. However, in order to make mm wave material processing lucrative, the economic viability should be given utmost importance. A gyrotron system will be suitable for industrial application provided it is highly efficient.

(b) The Sine Waveguide (SWG) structure has gained popularity as Sub-THz TWT due to its simple fabrication, low reflection and moderate loss. The interaction impedance for the simple SWG structure is moderate which leads to longer length of the structure. Therefore, ridge loading is introduced to enhance the interaction impedance [91]. However, the accurate fabrication of thin ridge adds the fabrication complexity. Also, the SWG TWT without a sever/attenuator has reported to produce undesired reflection [89]. Therefore, there are scope to incorporate different structural modification on the SWG to increase the efficiency or gain per unit length of the device. In order to eliminate reflection of RF power at the input section, two-section SWG structure with attenuator can be designed.

(c) The SWG structure are mostly designed in the frequency range from 200-350 GHz [24], [89], [91]. The performance of the SWG structure can be verified at higher frequency. The velocity tapering [113] is a popular technique to enhance output power and efficiency of TWT. The technique is successfully employed in various SWS [113]- [115]. However, velocity tapering on the SWG structure is not tried before. Therefore, velocity tapering may be introduced for efficiency enhancement of THz SWG TWT.

1.7 Problem Statement

Based on the gap area identified in Section 1.6, the following problems have been identified for conducting detail study:

(a) Design and efficiency enhancement of medium power gyrotron for industrial application.

(b) Design and Analysis of Width-Modulated Two-Section SWGTWT structure at G-band

(c) Design and Analysis of a SWG structure at 600-700 GHz.

1.8 Thesis Contributions

Three different interaction structures have been studied and introduced in the thesis for obtaining enhanced output power and efficiency of a Ka-band gyrotron and two TWT's in THz band. The various points which summarize the contribution of the thesis are as follows:

- Design of a triode type low velocity spread MIG gun for 28 GHz medium power gyrotron.
- Design and Particle in Cell (PIC) analysis of the gyrotron cavity to study the high power behaviour of gyrotron.
- Estimation of output power using analytical equation as well as PIC.
- Introduction of a slotted cavity for elimination of mode competition for the TE_{02} operating mode.
- Design of magnet system and three-staged depressed collector for the gyrotron.
- Estimation of cold circuit parameters of a G-band SWGTWT for broadband operation.
- Introduction of width-modulation on SWG structure to enhance interaction impedance
- Hot analysis of the width-modulated G-band SWGTWT.
- Introduction of two-section SWS to eliminate reflected power at input port of the device.
- Fabrication and experimental characterization of cold parameters of scaled version of width-modulated G-band SWGTWT
- Cold and hot analysis of a truncated SWGTWT at around 650 GHz.

1.9 Thesis Organization

The thesis has been organized into the following chapters:

Chapter 1 Presents an overview the current status and challenges faced in the design of mm-wave and sub-THz Vacuum Electron Devices. Promising VEDs for mm-Wave, and THz are discussed.

Chapter 2 Explains the governing equations and beam parameters in connections to the design of Magnetron Injection Gun (MIG) for gyrotron. A 2D and 3D designs of a triode MIG are presented. The outside diameter of the MIG is optimized to be 50 mm. In spite of lower MIG diameter, a negligible beam velocity spread of 1.2% is achieved. Design of magnetic focussing system for beam guidance is discussed. There are seven magnets in the design for beam forming, guidance and collection. The axial position, dimensions and the ampere-turn are obtained for each magnet. A three-staged depressed collector is designed for collecting the spent electron beam with maximum energy recovery. The overall efficiency of 67% is achieved using a depressed collector.

Chapter 3 Gives an overview of the interaction structure of gyrotron. The elements of cavity design, such as, Start Oscillation Current (SOC) and beam-wave coupling coefficient are discussed. Estimation of output power through analytical and numerical technique are presented. The output powers obtained from analytical equations and PIC simulation are in good agreement. A slotted cavity is introduced for elimination of mode competition between the operating TE_{02} mode and neighbouring TE_{22} modes. The numbers and dimensions of slots are optimized. The duration of mode competition between TE_{02} and neighbouring TE_{22} mode is reduced by 55% by incorporating axially directed slots in the inside wall of the cavity.

Chapter 4 Discusses the various advantages of Sine Waveguide TWT (SWGTWT) at sub-THz frequency. Cold circuit analysis is performed to design a width-modulated SWGTWT in G-band. A flat dispersion and greater value of interaction impedance for the frequency range 200 -245 GHz are achieved by choosing width modulation amplitude of 50 μm. Particle-in-Cell (PIC) simulation of the single as well as two-section width-modulated SWGTWT are performed. The output power of 39.5 W is estimated at 215 GHz with an efficiency of 3.81% for the two-section design. The elimination of reflected power from of input port of the two-section TWT over single section is quantified to be 98.29%. Fabrication and experimental measurement of the scaled SWG structure are discussed.

Chapter 5 Explains the advantages of truncated SWG structure at sub-THz frequency. The cold circuit analysis is performed on the truncated SWG structure to obtain suitable space for beam transportation and to flatten the dispersion characteristic of the structure. Particle-in-Cell (PIC) simulation is performed to predict the power output and efficiency of the TWT. The effect of beam shape on the TWT Performance is also discussed.

Chapter 6 Concludes the thesis. The scope of future works are also discussed.

2

Beam Generation and Guidance in Gyrotron

Contents

2.1 Introduction

Vacuum electron tube employs electron beam generated using DC power to produce or amplify RF power [17], [18]. Electron beam is ejected from cathode surface and focused by specially designed electrode called anode. The electron beam having desired shape and current density is injected to the interaction structure for beam-wave interaction. The spent electron beam is collected in the collector. In order to have effective beam-wave interaction, the electron beam should have a specified shape, current, and velocity. Beam generation and guidance system is therefore played a vital role for the overall success of a VED. Gyrotron [3]- [9] makes use of a hollow spiralling electron beam generated by a MIG. The magnetic field applied in the cathode, cavity and collector region, not only focusses the beam but also obtains the required diameter and cyclotron frequency.

2.2 Beam Generation in Gyrotron using Magnetron Injection Gun (MIG)

Electron gun [47]- [49] is the heart of gyrotron which produces hollow spiralling electron beam of specified parameters, such as, diameter, current, energy and velocity ratio (α). Triode type MIG is preferred as the extra electrode helps to have better control over the electron beam. Gyrotron makes use of a truncated conical thermionic cathode which operated in temperature limited region. The cathode [116], [117] is made of porous tungsten which is impregnated with rare earth metals for reducing the effective work function. The cathode is applied maximum negative potential in the tube usually in the range -10 kV to -100 kV relative to the main anode, which is subjected to the ground potential. The current density J_T of a thermionic cathode follow Richardson-Dushman law and modified by Shottky effect as given in 2.1.

$$J_T = 120.165 {T_c}^2 e^{-\frac{\Psi}{kT_c}} e^{\frac{0.4404\sqrt{E_n}}{T_c}} \tag{2.1}$$

where Ψ, T_c, E_n, and k are given by the work function, cathode temperature, normal component of the electric field and Boltzmann constant, respectively.

Uniform temperature is applied to the surface of the cathode so that the electrons can overcome the work function of the surface and escape from cathode. As the electrons emits from the slant surface area of the truncated cone, it contains both radial and axial velocities. The positive voltage in the anode provides axial velocity whereas the magnetic field provides the cyclotron frequency as well as radial velocity. The beam eventually follows a helical path. The magnetic field is gradually increased from cathode to cavity region. The cavity is subjected to uniform axial magnetic field so that the electron cyclotron frequency becomes close to the Eigen mode frequency of the operating mode.

2.2.1 Various Elements of MIG Design

The design of a MIG starts with the desired output parameters of the device. Depending on the output power, the beam current and voltage are decided. The magnetic field at cavity is determined by the operating frequency and mode. The radius of the electron beam at cavity is decided based on the operating mode. The emitted electrons from the cathode surface follow the magnetic flux lines on helical orbit and accelerated towards cavity region. The increasing magnetic field from gun to cavity compresses the radius of the beam which results increase in cyclotron frequency and radial velocity component of the beam. The mean diameter of the cathode is therefore chosen based on the electron beam diameter at cavity.

There are limits of various MIG parameters for smooth functioning of gyrotron [20], [118] which are given in the Table 2.1

The parameters used in the Table 2.1 is defined below.

- f$_m$ is the ratio of magnetic field at cavity and cathode. The value of $f_m > 20$ may lead to reflection of electron beam from the cavity and hence avoided.

- Δv quantify the spread in beam velocity in percentage. The larger velocity spread causes reduction in output power and efficiency. Therefore Δv should be as low as possible. The MIG of gyrotron operates in temperature limited region to reduce the velocity spread.

- ϕ_c is the angle of slant surface of the cathode with the beam axis. The value of ϕ_c is considered between 25^0 to 30^0 for achieving a laminar beam.

- α is the ratio between the radial velocity component and axial velocity component.

- J$_c$ is the emission current density from the cathode surface. The value of J_c is kept below

Table 2.1: Limiting range of various MIG parameters.

Parameters	**Value**
Magnetic compression ratio (f_m)	$f_m < 20$
Velocity spread (Δv)	$< 5\%$
Cathode angle (ϕ_c)	$\approx 25^0 - 30^0$
Alpha (α)	<1.8
Emission current density (J_c)	1.5 A/cm^2
Gap factor (G_f)	> 3
Voltage breakdown limit in vacuum	$\approx$ 10 kV/mm
Relativistic factor (γ)	< 1.2

1.5 A. The higher value of J_c is achievable by increasing the cathode temperature as the MIG Gun operates in temperature limited region. However, the higher temperature leads to faster evaporation of active components (Barium) of dispenser cathode causing the degradation of the life of cathode and hence avoided.

- G_f is given by $\frac{D_{ac}}{r_{lc}}$, where D_{ac} is the distance between cathode and first (modulating) anode and r_{lc} is the larmor radius at cathode.
- (γ) is defined as 2.2

$$\gamma = 1 + \frac{eV_0}{m_e c^2} \tag{2.2}$$

e, V_0, m_e and c are the charge of electron, Beam voltage, mass of electron and velocity of light in free space, respectively. There are various equations which are essential for design of MIG. The equations are as follows:

The total velocity of electron v is given by 2.3

$$v = c\sqrt{1 - \frac{1}{\gamma^2}} \tag{2.3}$$

The axial velocity v_z and radial velocity v_r of electron is given by 2.4 and 2.5, respectively.

$$v_z = \frac{v}{\sqrt{1+\alpha^2}} \tag{2.4}$$

$$v_r = \frac{v\alpha}{\sqrt{1+\alpha^2}} \tag{2.5}$$

Magnetic field at cavity region (B) is given by 2.6

$$B = \frac{f(GHz)\gamma}{28s} \tag{2.6}$$

f is the frequency in GHz, s is the harmonic number.

The cavity radius R_0 and beam radius at cavity r_b are given by 2.7 and 2.8, respectively.

$$R_0 = v_{mp}\frac{\lambda}{2\pi} \tag{2.7}$$

$$r_b = v_{m\pm1,p}\frac{\lambda}{2\pi} \tag{2.8}$$

where v_{mp} and λ are given by p^{th} root of $J'_m(x)$ and wave length, respectively. $J'_m(x)$ is the derivative of m^{th} order Bessel function. The requirement of magnetic field at cathode B_c can be expressed in terms of B as per 2.9

$$B_c = \frac{B}{f_m} \tag{2.9}$$

Similarly, the mean radius of cathode r_c can be expressed in terms of r_b as per 2.10

$$r_c = r_b\sqrt{(f_m)} \tag{2.10}$$

2.2.2 2D and 3D design of MIG for a medium power gyrotron

A MIG gun is designed for a medium power TE_{02} mode gyrotron for material processing application. The 2D electro-magneto static analysis is performed in EGUN to obtain the beam trajectories. EGUN computes the trajectories of charge particles in electro-static and magneto-static field. It also takes into account of self magnetic field and space charge effects. The input parameters of MIG, such as, electrode geometries, emission area, electrode voltages, positions of magnets and their ampere-turn are provided by means of an input file. The software generates the output file, from which the geometry, equipotential lines, beam trajectories and magnetic field profiles are obtained.

The various input parameters and initial values are taken based on the Table2.1. The value of other parameters, such as, B, R_0 and r_c are calculated as 1 Tesla, 11.97 mm, and 3.141 mm based on 2.6, 2.7 and 2.8, respectively. The electron beam is considered to be launched at the first radial maxima of TE_{02} mode to have sufficient gap between the beam and wall so that the beam-wall interception can be minimized. The initial parameters for the MIG are given in Table 2.2.

Table 2.2: Initial parameters for the MIG design.

Parameters	**Value**
Frequency (f)	$\approx$ 28 GHz
Magnetic compression ratio (f_m)	$f_m \approx 13$
Velocity spread (Δv)	$< 5\%$
Cathode angle (ϕ_c)	28^0
Alpha (α)	1.4-1.8
Emission current density (J_c)	$\approx$ 1.0 A/cm^2
Beam current (I_b)	1 A
Beam voltage (V)	40 kV
Gap factor (G_f)	> 3
Voltage breakdown limit in vacuum	$\approx$ 10 kV/mm
Relativistic factor (γ)	1.0782

Various MIG parameters, such as, the modulating anode voltage, magnetic field at cathode, and magnetic field profile of the MIG are estimated with respect to its geometry. Two different MIG geometries are optimized through 2D simulation in EGUN. The length of emitting surface is taken 2.97 mm to limit transverse velocity spread Δv value. The electron beam trajectories,

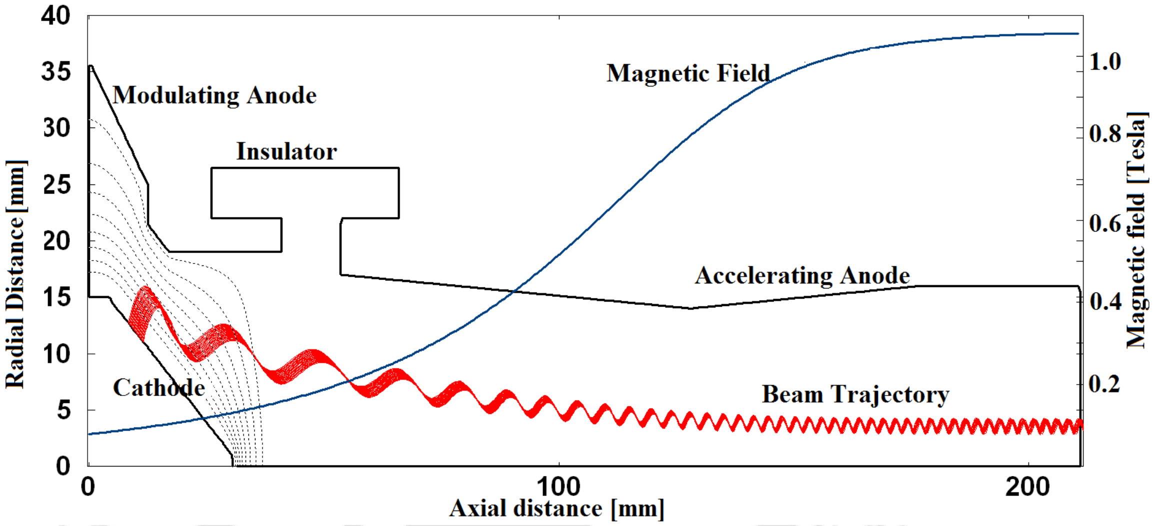

Fig. 2.1: 2D view of *geometry 1* of the triode type MIG, showing trajectory of electron beam, magnetic field profile and equipotential lines.

equipotential lines and magnetic field profiles of *geometry 1* and *geometry 2* are provided in Fig. 2.1 and Fig. 2.2, respectively.

The final MIG parameters for *geometry 1* and *geometry 2* are compared in Table 2.3.

The velocity spread (Δv) obtained for *geometry 1* is 0.11% whereas the velocity spread of *geometry 2* is 1.8%. The maximum gun diameters of *geometry 1* and *geometry 2* are 70 mm, and 50 mm, respectively. The Δv value for *geometry 1* appears to be idealistic as the same cannot be achieved in practical case. Therefore, both the MIG guns are re-simulated in CST Particle tracking solver for validating the EGUN results in 3D solver. The 3D geometries of the MIG are made in CST. The magnetic field profiles of EGUN are exported to CST. The potentials are applied to the electrodes as applied in EGUN. The Δv and α are calculated by post processing the CST results. The Δv values for *geometry 1* and *geometry 2* are obtained to be 0.67%, and 1.2%, respectively without considering initial kinetic and angular spread of electron beam. It is observed that the Δv value obtained for *Geometry-1* in CST is not as idealistic as in EGUN. The 3D Particle tracking solver calculates the velocity spread value more accurately. The values of α are estimated to be 1.38, and 1.43 for *geometry 1*, and *geometry 2*, respectively. The equipotential lines formed in *Geometry 1* are shown in Fig. 2.3. It is clearly seen that the equipotential lines are almost parallel near the emission surface. The potential is maximum towards the accelerating anode and minimum near cathode. The distribution of equipotential

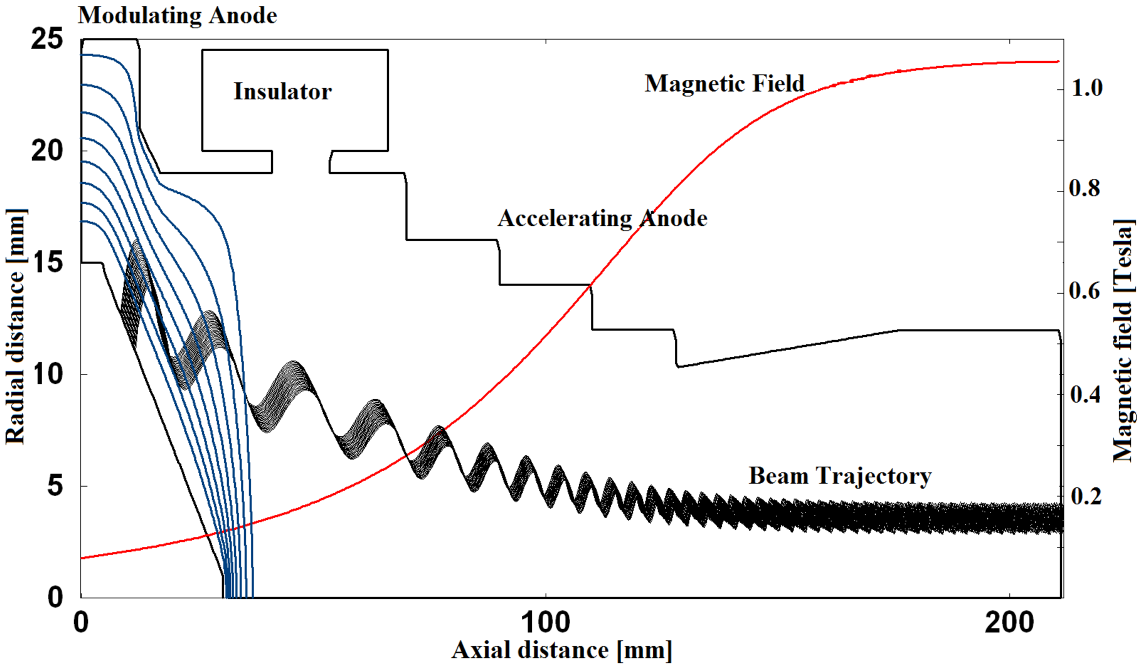

Fig. 2.2: 2D view of *geometry 2* of the MIG.

Table 2.3: MIG parameters for Geometry-1 and Geometry-2

Parameters	Geometry 1	Geometry 2
Maximum gun diameter (d_{max})	70 mm	50 mm
Cathode voltage (V_c)	-40 kV	-40 KV
Modulating anode voltage (V_m)	-18.5 kV	-18.5 kV
Accelerating anode voltage (V_a)	0 kV	0 kV
Magnetic field at cathode (B_c)	0.07 T	0.07 T
Beam diameter (D_{beam})	6.26 mm	6.26 mm
Δv	0.11%	1.8%
Mean velocity Ratio (α)	1.4	1.4
Mean larmor radius (r)	0.52 mm	0.51 mm

lines reveal a triode type MIG. The beam trajectory of *geometry 1* is shown in Fig. 2.4.

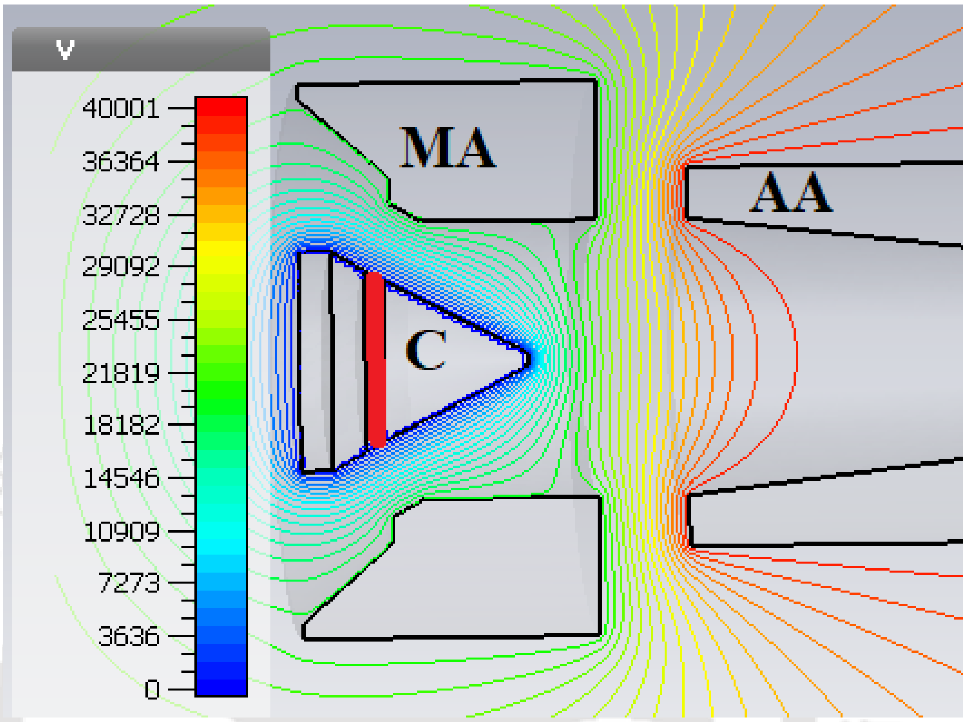

Fig. 2.3: Equipotential lines of *geometry 1*, C: Cathode, MA: Modulating Anode, AA: Accelerating Anode.

The Δv value is a crucial MIG parameter as wide spread of beam velocity deteriorates the output power and efficiency of a gyrotron [119]. There are various factors which affects the Δv value, such as, inhomogeneous electric and magnetic field in the vicinity of emitting surface, temperature variation on the emitting surface, peachy emission, surface roughness of the emitter, and variation of space charge due to reflected electron. Therefore, it is important to determine Δv value for a MIG considering the above mentioned scenario. The variation of temperature at on the cathode surface gives rise to kinetic energy spread of the emitted electrons. The other factors like surface roughness and inhomogeneous field distribution leads to angular spread. Therefore, the emitted electrons are assigned angular spread to simulate the velocity spread. The Δv obtained for different initial energy of electrons are plotted in Fig. 2.5.

It is observed that with the increase of angular spread Δv increases. However, the Δv value is restricted to 5%, if the initial energy of electron and angular spread value can be kept below 50 eV and 60^0, respectively.

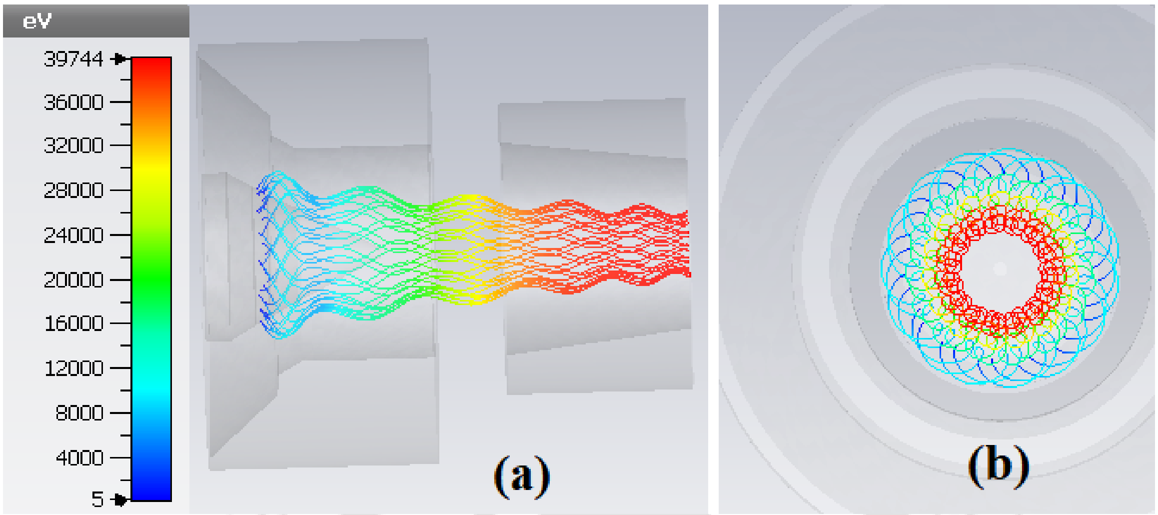

Fig. 2.4: Beam trajectory of *geometry 1*: (a) Front view and (b) Top view.

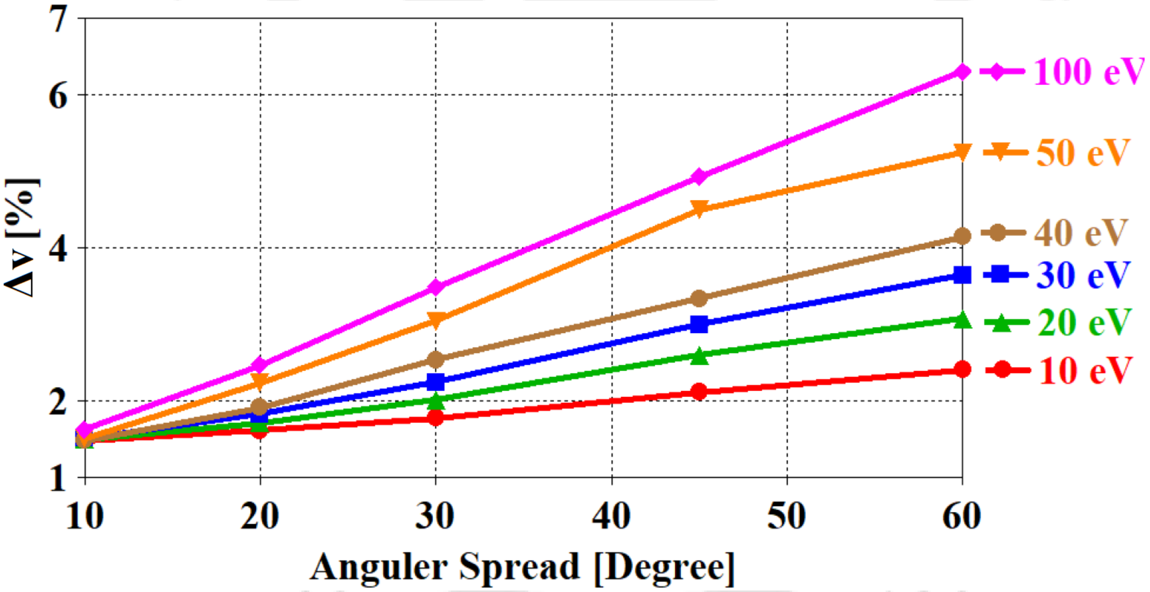

Fig. 2.5: Δv value of MIG *geometry 1* with angular spread for different emission energy.

2.2.3 Results and Discussions

Two MIG geometries are optimized in EGUN. The beam parameters obtained in EGUN are validated using 3D particle tracking solver of CST. The beam velocity spread is estimated by assigning angular spread of emitted electrons. Both the geometries provide acceptable velocity spread. The maximum inside diameter of *geometry 1* and *geometry 2* are 70 mm, and 50 mm, respectively. The lower diameter will allow lower magnet bore diameter at cavity. The lower magnet bore diameter will reduce the fringing field and helps to maintain homogeneity of magnetic field in the cavity. Therefore, *geometry 2* can be chosen.

2.3 Beam Guidance System of Gyrotron

The beam guidance system of a gyrotron consists of a set of magnet [62], [63] which can be categories as gun magnet, cavity magnet and collector magnet. Presence of suitable magnetic field at all the three region serves a specified objective, for example, the homogeneity of magnetic field at gun region is very essential for achieving low velocity spread and lower spread in velocity ratio. A specified value magnetic field in this region also determines the beam diameter in the cavity which is vital for maximizing the beam-wave interaction. In fact, the profile of magnetic field from gun to cavity should be smooth enough to avoid reflection of beam. The requirement of magnetic field at cavity is the maximum among the other two regions. The uniformity and appropriate value of magnetic field at cavity is extremely vital as it determines the cyclotron frequency. A little deviation of the magnetic field value in this region leads to reduced efficiency or excitation of undesired modes. On the other hand, the purpose of magnetic field at collector is to disperse the beam over a wide area. A weak magnetic field with specific profile is required in this area. The gun and cavity magnets are generally made of copper solenoid whereas the cavity magnet is made using high field superconducting solenoid. In some cases, a combination of high temperature superconductor and low-temperature superconductor magnets have been used to reduce the operational cost of the gyrotron. However, the liquid cooled superconducting magnets [120] requires continuous supply of liquid Helium (He) and liquid Nitrogen (N). The superconducting magnets have higher operational cost and longer turn on time as well.

On the other hand, permanent magnets [121] can provide up to 1 Tesla constant DC magnetic field without any consumption of power or resources. However, the magnetic field of a permanent magnet cannot be controlled. Also, those magnets are very heavy and bulky which makes it difficult for handling during installation. Pulsed solenoid [122], [123] which utilizes simple copper coil, is another solution for very short pulse operation of gyrotron. It can induce a very high magnetic field for very short duration. Due to thermal inertia, the material heats up during operation and therefore increase its resistance thereby decreasing the current flow and also the magnetic field. Therefore, the pulse width of such gyrotron is limited to few milliseconds.

2.3.1 Design of Magnetic Focusing System of a Medium Power Gyrotron

The magnetic focusing system of the medium power gyrotron for material processing application is designed in EGUN. The outline of the geometry, position of magnets and the optimize magnetic field profile are shown in Fig. 2.6. There are seven magnets M1 to M7 in the magnetic focusing system in which M1 is the gun magnet, M2, M3 and M4 are the cavity magnets, and M5, M6 and M7 are the collector magnets. The magnetic field at cathode is 0.07 T generated due to combined effect of gum and cavity magnets. The magnetic field obtained at cavity is 1.05 T which is required to have beam-wave interaction between the spiralling electron beam and TE_{02} cavity mode. A uniform magnetic field at cavity is achieved due the combined effect of M2, M3 and M4. The M2 and M4 both have 8 solenoid turns with 5200 A current flow whereas the M3 has 33 solenoid turns with 3550 A current flow. The beam diameter is minimum in the cavity due to strong magnetic field in this region. As the magnetic field is decreased at collector the beam diameter starts increasing. The collector magnet M5 is placed to avoid a sudden decrease of magnetic field after the cavity which cause a beam interception with the metallic mirrors in radial output gyrotron. The function of M6 and M7 are to tailor the magnetic field in the collector region so that the beams are dispersed and collected over wide collector areas which is essential to limit the heat flux density at a particular area. It is seen from Fig. 2.6 that the beam gets collected over 800 mm to 1000 mm axial distance. The magnetic field profile obtained in EGUN is considered to design a depressed collector for the gyrotron in CST particle tracking solver which is discussed in the next section.

2.4 Collector

After the beam-wave interaction in the cavity, the spent electron beam is required be collected in the collector. The interaction efficiency of a typical gyrotron is around 35%. Therefore, the spent electron beam sill has sufficient kinetic energy to manage in the collector. Due to beam-wave interaction, most of the electrons loss their energy and a few gain. This causes a

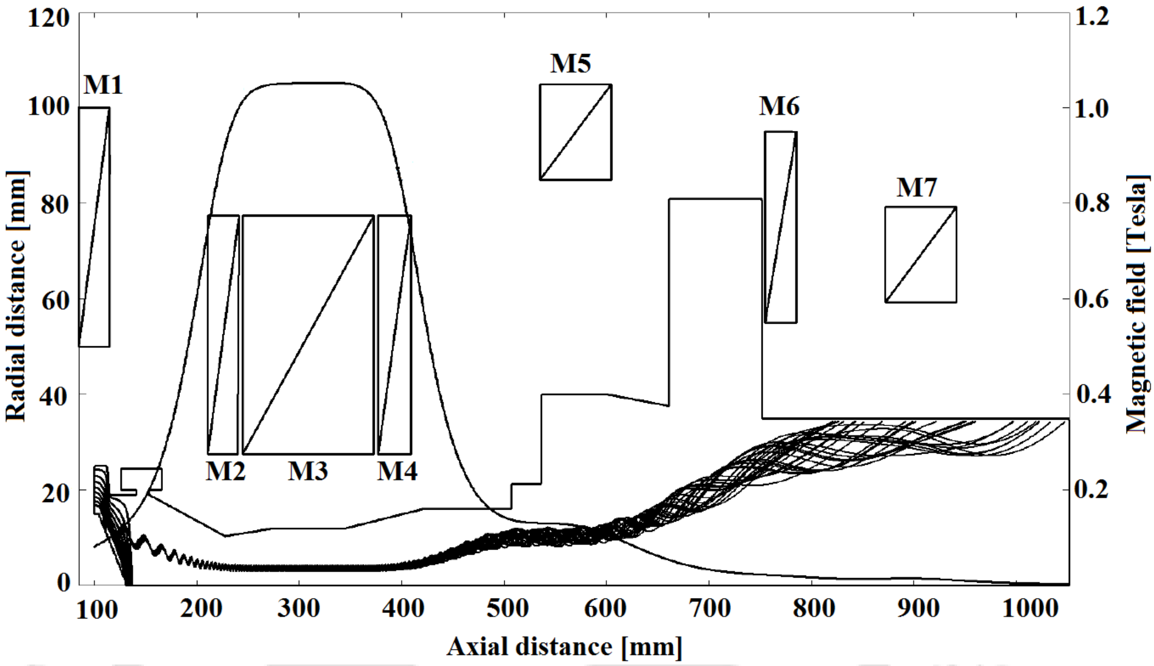

Fig. 2.6: 2D geometry of the gyrotron showing axial magnetic field, beam trajectory and equipotential lines.

wide energy spectrum of the spent electron beam.

The kinetic energy of the interacted electron beam can be recovered to some extent by means of a depressed collector and the rest energy is converted into heat at the wall of the collector. The electron beam should be collected over a wide area to minimize the wall loading for ensuring longer life of the collector. The maximum allowable beam loading for pure copper is 0.5 kW/cm^2 [20]. The collector can be manufactured using either pure copper or copper based metal matrix composite added with a fraction of aluminum oxide powder [124]. This greatly increase the mechanical strength of the material even at higher temperature while maintaining the thermal and electrical conductivity. The outside body of the collector is force convection cooled. In order to increase the surface area, the outer surface of the collector is grooved radially or axially and the water flow is directed perpendicular to the groove for achieving fluid turbulence. Vaporization cooling is also performed to obtain high convection efficiency.

2.4.1 Design of a Depressed Collector for Medium Power Gyrotron

Depressed collector [58]- [61] is used to retard the electrons before being collected. The depressed collector can be single-stage or multi-stage. The collector electrodes are subjected to negative potentials to repel the electrons so that they land softly on the collector and cause less heating. In multi-stage depressed collector, the first collector is subjected to lowest depressing potential and the last electrode is applied highest depressing potential. The shape of electrode, applied potential and the magnetic field is optimized in such a fashion that the lower energy electrons are collected at lower depressing potential and vice versa. This increases the energy recovery and lessen the collector heating which are the primary merits of depressed collector. In case of depressed collector, less effective input power is required and hence efficiency is increased. The magnetic field profile in the collector region is tailored to sort the electrons based on their energy.

A three-staged depressed collector for the medium power gyrotron is designed in 3D particle tracking solver in CST. The magnetic field obtained in EGUN is imported to CST to trace the path of electrons as discussed in the previous section. The hot analysis of the gyrotron is discussed in Chapter 3 where the spent beam energy spectrum from the phase spaced monitor is obtained. The percentage of electrons for various energy levels are quantified by analyzing the data of phase spaced monitor of CST. The spent electron beam energy spectrum is plotted in Fig. 2.7.

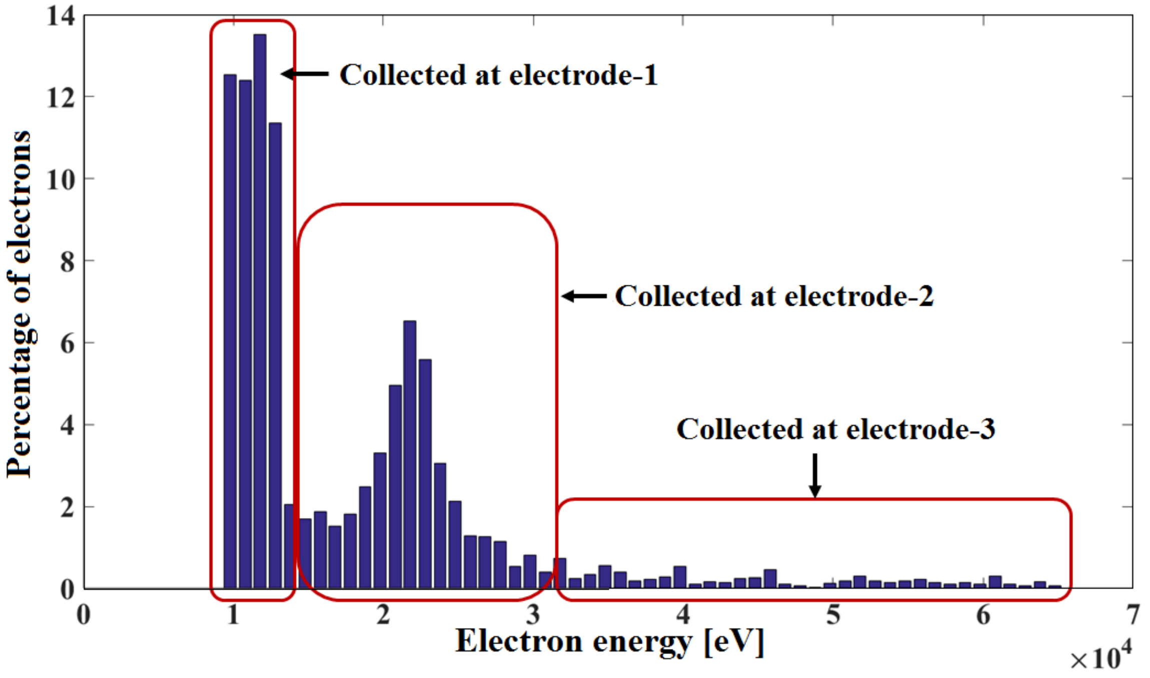

Fig. 2.7: Spent electron beam energy spectrum.

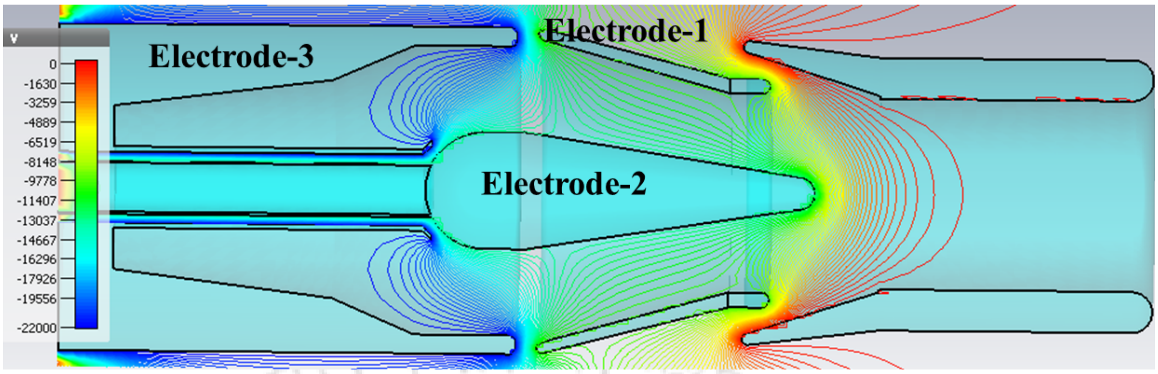

Fig. 2.8: Formation of equipotential lines inside the three stage depressed collector.

The electron beam enters the cavity with a constant 40 KeV energy. However, after interaction most of the electrons losses their energy. The minimum energy of the spectrum is 10 keV whereas the maximum energy component is 67 keV.

A truncated conical virtual cathode is placed at the end of the cavity to generate hollow spiralling beams of specified energy and velocity ratio. The beams of various energies in the energy spectrum are tracked in the collector region with the objective to collect the higher energy electron at higher depressing potential and vice-versa. The shape of the electrodes and the potential are optimized for the same. The potential of electrodes 1, 2, and 3 are finalized to be -6 kV, -13 kV, and -22 kV, respectively. The cross sectional view of the collector electrodes and the equipotential lines are shown in Fig.2.8.

The magnetic lenses formed by the equipotential lines guide the electron beam in the collector region. The beams with different energies are emitted at the virtual cathode and the beam path is traced till the collector end. It is observed that the electrons up to 14 keV energy are collected at collector-1 which is at -6 kV potential. There are 51.85% electrons in the beam having up to 14 keV energy as calculated from the phase-spaced data. The energy level of the electrons ranging from 15 keV to 31 keV are collected at electrode-2. There are 40.42% electrons in this energy range. The electrons beyond this energy which accounts for 7.70% of the total electrons are collected at electrode-3. The trajectories of electron beam with various energy level are shown in Fig.2.9.

The amount of energy recovery at the particular electrode is calculated by multiplying the

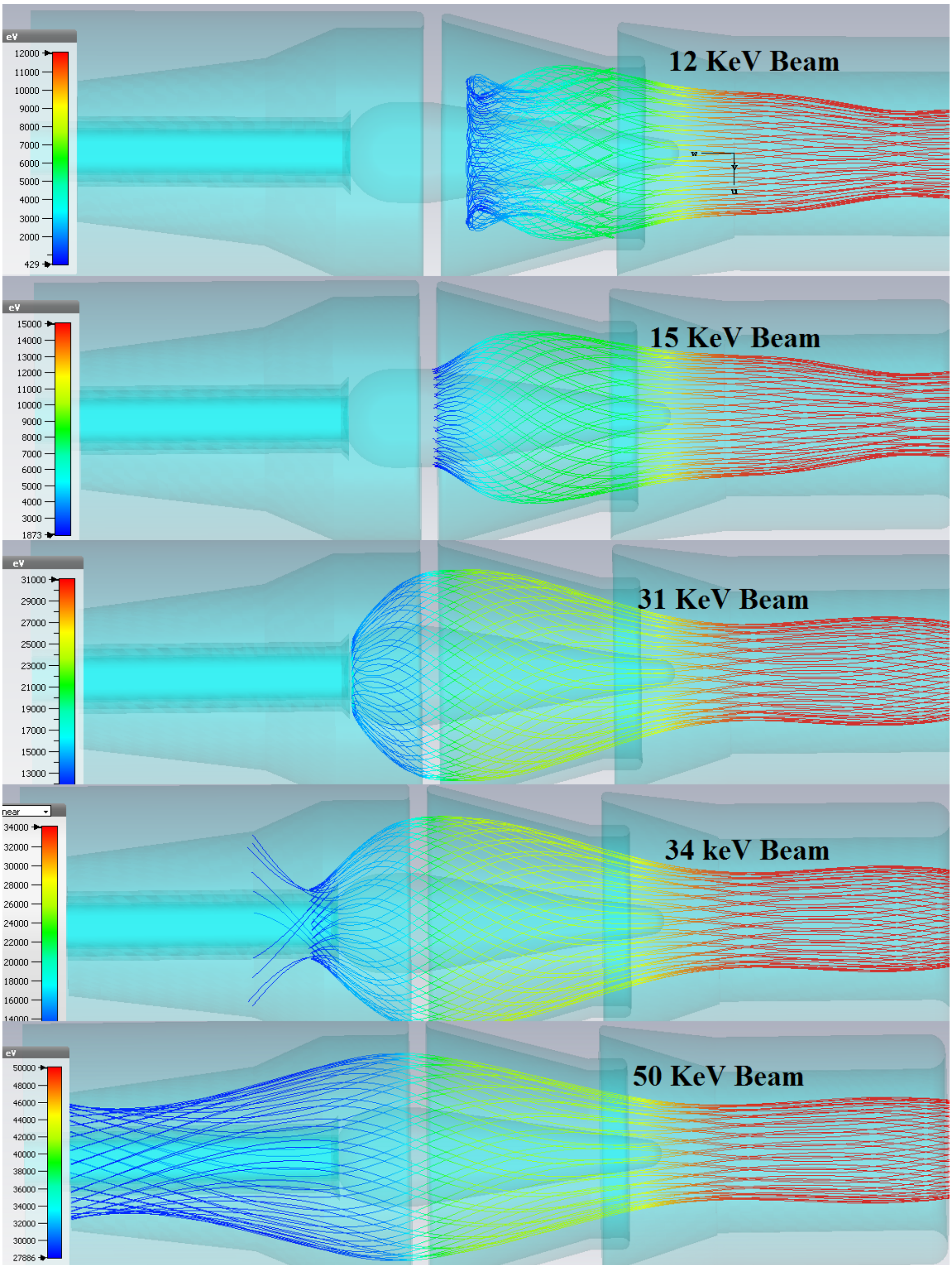

Fig. 2.9: Five electron beams with fixed energy level, 12 keV, 15 kev, 31 keV, 40 keV and 50 keV are shown. The figure depicts that lower energy electrons are getting collected at lower depressing potential and vice versa.

depressing potential with beam current collected in the electrode.

The efficiency of depressed collector is calculated in Table 2.4.

Table 2.4: Calculation of collector efficiency.

Parameters	**Value**
Input power (P)	40 kW
Mm-wave power output (P_{mm})	20.08 kW
Spent beam power (P_{sp}) =(P-P_{mm})	19.92 kW
Beam power recovery at electrode-1 (P_{r1})= 51.85×6/100	3.11 kW
Beam power recovery at electrode-2 (Pr2) = 40.42 × 13/100	5.25 kW
Beam power recovery at electrode-3 (P_{r3})=7.70 ×22/100	1.69 kW
Total beam power recovery (P_r) = (P_{r1} +P_{r2} +P_{r3})	10.05 kW
Effective input power (P_{eff}) =(P- P_r)	29.94 kW
Efficiency with depressed collector (η_c)= (P_{mm}/P_{eff}) ×100	67.06 %

2.4.2 Results and discussions

DC input power of 40 kW is applied for generating a 1 A, 40 kV electron beam. The RF output power of 20.08% is estimated in the Particle-in-Cell analysis described in the next chapter. The power for the spent electron beam is calculated by subtracting the RF power from the DC input power. The RF loss in the cavity and other parts of the tube is neglected in the calculation. It is estimated that the electrode 1, 2 and 3 collect 518.5 mA, 404.2 mA and 77.3 mA of beam current, respectively. The power recovery at each electrode is calculated by multiplying the collector current with depressing potentials.

2.5 Summary

The beam guidance system of a 20 kW CW gyrotron operating at 28 GHz in TE_{02} mode is designed. The 2D design of two triode type magnetron injection guns are optimized in EGUN. The electron beam parameters are estimated for both the geometries and compared. The 2D design in EGUN is validated using 3D particle tracking solver in CST. The optimum magnetic field profile for the whole geometry of the gyrotron is evaluated in EGUN. The positions of various magnets for realizing the magnetic field is obtained. There are 7 magnets in the design. The spent electron beam energies as obtained in PIC phase spaced monitor are analysed and plotted. The data is utilized to design and calculating the efficiency enhancement by a 3 staged depressed collector. The 3D electro-magneto static analysis is carried out in CST particle tracking studio to finalize the design of a 3 staged depressed collector. The particle tracking simulation shows that the spent electron beam contains a wide energy spectrum, which are sorted in the collector and gets collected at 3 depressing potentials. The depressed collector recovers almost 10.05 kW of input power. The energy recovery causes a substantial enhancement of efficiency of the gyrotron. The depressed collector also brings down the requirement for collector cooling. The net efficiency achieved for the gyrotron is 67.06%. The higher efficiency of the CW gyrotron will be viable for industrial application. The findings of the current study are expected to contribute for the future development of high efficiency gyrotron for industrial applications.

3

Interaction Structure of Gyrotron

Contents

3.1 Introduction

The spiralling electron beam and transverse electric mode of RF wave interacts in a open-ended waveguide structure is called interaction structure or cavity of gyrotron. The cavity has a straight section in the middle and two taper sections at both end. The input taper is also called down taper as the diameter is decreased linearly in this section. The down taper prevents backward propagation of RF wave as it is a cutoff section. The beam-wave energy exchange takes place at the uniform section of the cavity. The third section of cavity is output taper or up taper where the diameter is increased linearly and connects with either a non-linear taper section for an axial output gyrotron [125] or an internal mode launcher for a radial output gyrotron [19]- [21]. In order to minimize the mode conversion at the junction of two section, parabolic smoothing [20] is done. The straight section operates just above the cut off of the operating mode. The cyclotron frequency of the electron beam is made slightly lower than the eigen frequency of the operating mode for net energy transfer from beam to field. As the gyrotron operates in TE mode, the radial velocity component of electron beam contributes to energy exchange. The electron beam is ejected from a slant surface of cathode so that the electron has axial as well as radial velocity component. Due to the increasing magnetic field from gun to cavity region, the cyclotron frequency increases and this leads to the increase of radial velocity. The electron traverse on a helical path encircling the magnetic lines of force. The hollow gyrating electron beam can transfer its energy to the electromagnetic wave provided the electrons are bunched in phase in their cyclotron orbit. The phase bunching of the electrons are possible as the electron cyclotron frequency is a function of electron energy. The electron cyclotron resonance condition between the electrons and RF wave is satisfied based on

$$w - k_z v_z = s w_c \tag{3.1}$$

where w is the angular frequency of the RF wave, k_z is axial wave number, v_z is the axial velocity of the electron, s is the harmonic number and w_c is the cyclotron frequency of electron.

The electron beam of gyrotron attains a velocity which is a fraction of c (velocity of light) due to the applied potential and therefore the beam becomes weakly relativistic. The relativistic effect come into play in the beam-wave interaction. A frequency shifts ($k_z \times v_z$) which is known by relativistic Doppler effect occurs in the RF. However, in case of gyrotron $v_z < v_r$ and thus (3.1) becomes:

$$w \approx s w_c \tag{3.2}$$

Gyrotron is Electron Cyclotron Resonance Maser (ECRM) as it generates electromagnetic energy by using gyrating electrons. The cyclotron frequency w_c is given by (3.3)

$$w_c = \frac{eB_0}{m_e \gamma} \tag{3.3}$$

B_0 is the applied magnetic field, m_e is the mass of electron, e is the charge of electron and γ is the relativistic factor. It may be noted that, B_0 determines w_c. Because of this reason the interaction structure of gyrotron is simple waveguide structure whose dimension is not limited by the operating frequency. The interaction volume can be made larger by operating the device at higher order mode. Therefore, the power handling capability of gyro-devices are many fold in comparison to the linear beam tubes which suffer from dimensional shrinkage at higher operating frequency.

The helical beam generated by the MIG gains higher cyclotron frequency due to increasing magnetic field from gun to cavity region. The gyrating beam interacts with the waveguide mode (TE_{mn}) when the cyclotron frequency and the frequency of the EM mode are approximately equal. The dispersion of the waveguide mode is given by 3.4.

$$w^2 = c^2({k_z}^2 + {k_\perp}^2) \tag{3.4}$$

Where, c is the velocity of light, $k_\perp$ is the characteristic transverse wave number which is given by 3.10.

$$K_\perp = \frac{\nu_{mp}}{R_0} \tag{3.5}$$

ν_{mp} and R_0 are given by p^{th} root of $J'_m(x)$, and radius of waveguide cavity, respectively. The interaction region of gyrotron for fundamental as well as harmonic operation is shown in Fig. 3.1.

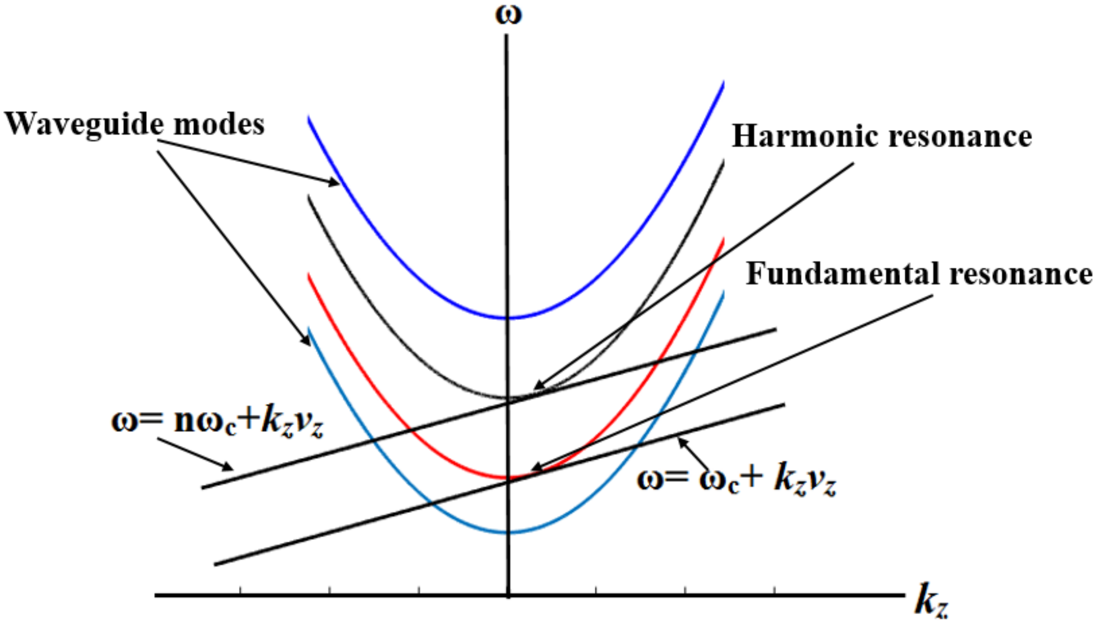

Fig. 3.1: Fundamental and harmonic interaction zone of gyrotron.

At the resonance point the beam line and waveguide mode intersect. The harmonic resonance occurs at point where harmonic beam line and waveguide mode meet.

The 3 stages of beam-wave interaction [126] is depicted in Fig. 3.2.

In the first stage, the electron orbit is displaced due to the accelerating field as shown in Fig. 3.2(a). Some electrons gain energy while the other electrons which face the decelerating phase loss energy. However, the energy of electron ring increases as the electrons gain net energy from the EM field.

During the second stage, the relativistic effect comes into play. The effective mass of higher energy electron increases and vice versa. Higher effective mass leads to lower cyclotron frequency. This results in formation for electron bunch. If the frequency of EM wave is made little higher than the electron cyclotron frequency or its harmonic ($w > sw_c$), the bunch can be formed in the decelerating phase of the EM field.

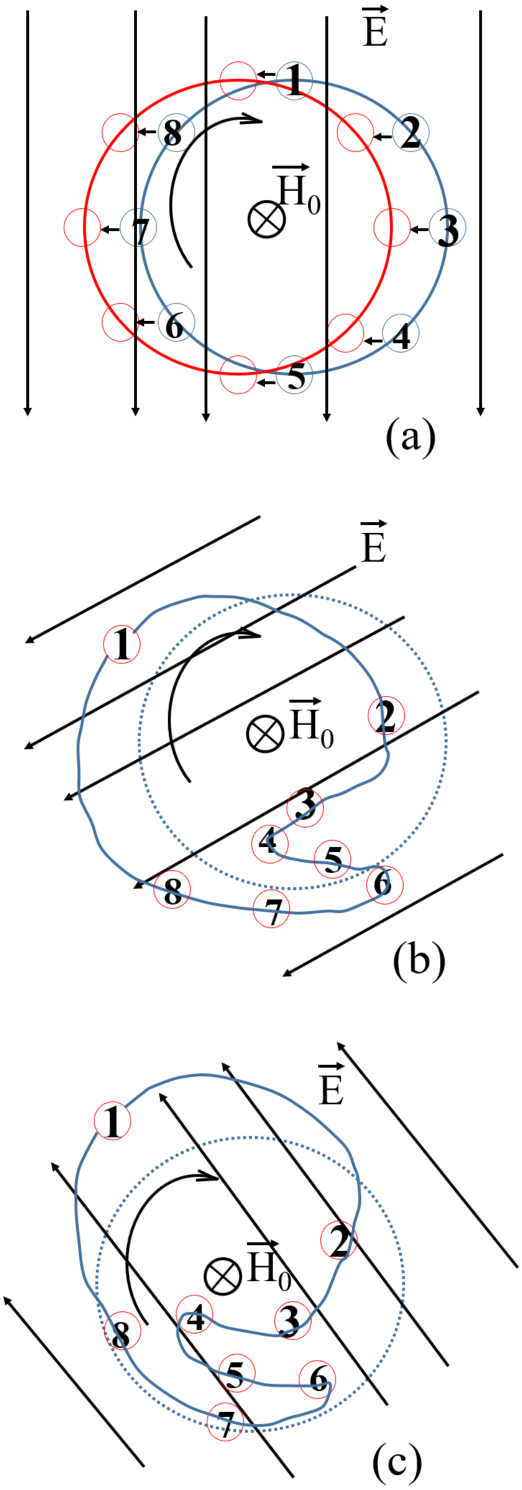

Fig. 3.2: 3 stages of beam-wave interaction in gyrotron [126]: (a) energy modulation, (b) orbital bunching, and (c) deceleration of bunch.

Finally, during the third stage the whole bunch decelerated as the electrons transfer energy to the EM field.

3.2 Cavity Design for Gyrotron

Gyrotron makes use of a cylindrical waveguide cavity comprises of a down-taper, resonant section and up-taper. The beam-wave interaction take place in the resonating cavity. The dimension of the cavity is very critical as it determines frequency of operation. The radius of straight section of the cavity R_0 is given by 2.7, so that the cavity is operated just above cut-off for the operating mode.

The resonating behaviour of the cavity comes from the taper section in which down-taper fully reflects the operating mode and up-taper partially transmit the generated RF wave. A cavity is designed for a medium power gyrotron aimed for material processing. The operating frequency and mode are considered to be 28 GHz, and TE_{02} mode, respectively. Eigenmode analysis is carried out in CST Microwave Studio [25] to inspect the various electromagnetic modes and corresponding frequencies existing in the cavity.

Down-taper angle is optimized at 2°. The angle is sufficient to prevent backward propagation of TE_{02} operating mode. The angle greater than this value will increase the risk of beam-metal interception. The transient analysis is performed in CST Microwave Studio to calculate the diffractive Q (Q_{diff}) of the cavity as per [127].

A discrete current port is used to excite the cavity for a frequency range 26 to 30 GHz to calculate the Q_{diff} of the cavity. A field probe is placed at the first radial maxima of TE_{02} mode of the cavity for recording the electric field spectrum of excited TE_{02} mode. Q_{diff} is given by $\frac{f_{c0}}{\Delta f}$, where f_{c0} and Δf are the centre frequency, and 3 dB bandwidth, respectively. The output taper angle can control the value of Q_{diff}. The Q_{diff} is found to be 933 for the output taper angle of 3° which is acceptable for a gyrotron. The dimensional parameters of the cavity are given in Table 3.1.

The axi-symmetric TE_{02} mode is chosen for the gyrotron because the same exhibits minimum wall loss and considerable mode separation between the operating and neighbouring

Table 3.1: Cavity parameters.

Parameters	**Value**
Frequency (f)	28 GHz
Cavity radius	11.97 mm
Cavity length	70 mm
Down taper angle	2^0
Up aper angle	3^0
Down Taper length	48 mm
Up Taper length	75 mm

modes, such as, TE_{12}, TE_{22}, and TE_{13}. It may be noted that, the cavity of gyrotron is an over moded structure and therefore it supports various modes. In order to ensure a single mode operation, proper operating condition has to be satisfied. The Start oscillating current (I_{soc}) [20] helps to identify the magnetic field to excite a particular mode.

3.2.1 Start Oscillation Current

Gyrotron works as a millimetre wave source, oscillating at desirable mode and frequency. However, the self-excitation is possible provided a number of conditions to be fulfilled. The minimum current at which a gyrotron starts oscillating is called starts oscillation current (I_{soc}). Therefore, I_{soc} is the threshold current above which the device needs to be operated. The knowledge of I_{soc} for the operating as well as the neighbouring modes are essential to obtain the operating magnetic field that can eliminate the competing modes and paves the way for the desired mode of operation.

The I_{soc} depends on various beam parameters, resonator geometry and magnetic field. The beam parameters include beam voltage, beam radius, velocity ratio, etc. Individual modes supported by an interaction structure of gyrotron has a unique I_{soc}. The I_{soc} for the desired as well as co-existing modes should be plotted and compared to find out the suitable magnetic field to excite the operating mode with maximum efficiency and suppressing the competing modes. The start oscillation current is expressed analytically as the minimum current at which the rate of change of output power $\frac{dP}{dt} > 0$, when, P → 0.

The start oscillation current, I$_{soc}$, can be written as 3.6.

$$I_{soc}(\triangle,\mu) = 8.56 \times 10^4 \frac{exp[\frac{\mu\triangle^2}{8}]}{\mu^2(\mu^2 \triangle -4s)}(\frac{\gamma_0}{Q})\beta_{\perp 0}^{2(3-s)}(\frac{L}{\lambda})C_{mp}{}^{-2} \tag{3.6}$$

Where μ is the normalized length of the interaction region given by 3.7

$$\mu = (\frac{\pi L}{\lambda})(\frac{\beta_{\perp 0}^2}{\beta_{z0}}) \tag{3.7}$$

$\triangle$ is the frequency mismatch detuning parameter and expressed as 3.8

$$\triangle = (\frac{2}{\beta_{\perp 0}^2})(1 - \frac{s\Omega_0}{\omega\gamma_0}) \tag{3.8}$$

C$^2_{mp}$ is the beam-wave coupling coefficient and given by 3.9

$$C_{mp}^2 = \frac{J^2{}_m(k_{mp}R_b)}{(\nu^2{}_{mp} - m^2)J^2{}_m(\nu_{mp})} \tag{3.9}$$

The various variables used in 3.6 to 3.9 are as follows:

s is the harmonic no, γ_0 is the relativistic factor, Q is the quality factor, $\beta_{\perp 0}$= $(v_{\perp 0}/c)$, is called the normalized velocity in the transverse direction. L is the straight section of the cavity, λ is the wavelength, β_{z0}= (v_{z0}/c) is the normalized axial velocity, Ω_0 is the cyclotron frequency and R_b is the radius of the electron beam.

The I$_{soc}$ is computed for all the co-existing modes along with the operating TE$_{02}$ mode for the proposed medium power gyrotron operating at 28 GHz. The I$_{soc}$ is plotted in Fig. 3.3. It is seen that TE$_{01}$, TE$_{12}$, TE$_{22}$, and TE$_{13}$ modes are coexisted along with the TE$_{02}$ operating mode. However, TE$_{22}$ mode being closely spaced with the TE$_{02}$ mode, has maximum probability to compete with the operating mode. The I$_{soc}$ for each mode has a minima for a magnetic field value. The I$_{soc}$ for TE$_{02}$ is minimum at 1.055 T. Therefore, the gyrotron should be operated at nearly 1.055 T to suppress the competing modes.

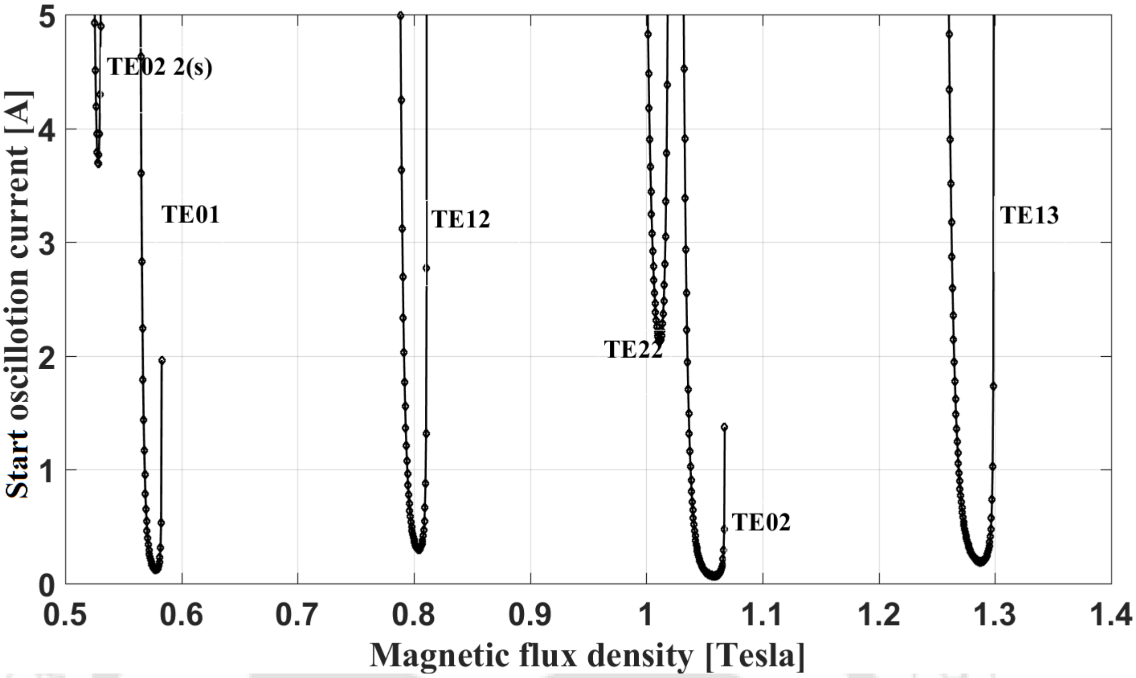

Fig. 3.3: Start Oscillation Current (I_{soc}) for TE_{02} and neighbouring modes.

3.2.2 Beam-Wave Coupling Coefficient

Coupling coefficient (C^2_{mp}) is an important parameter which provides the optimum diameter of electron beam for obtaining maximum output power and efficiency. The expression for C^2_{mp} is provided in 3.9. C^2_{mp} is plotted for the operating TE_{02} mode in Fig. 3.4. The X-axis is normalized with cavity radius. It is observed that the plot has two maxima which are based on the two radial maximas of TE_{02} mode. The first maxima is greater than the second maxima which appears at $R_b/R_0 = 0.2617$. Launching the beam at the first radial maxima allows to have sufficient gap between the beam and cavity wall. Therefore, electron beam radius is calculated to be 3.13 mm based on above.

3.3 Single mode Time Dependent Approach for Gyrotron

The single mode time dependent equations [128], [129] are solved to compute the output power and efficiency particularly for low or medium power gyrotron. In the current study, the same approach is adopted to calculate the evaluation of output power of the medium power gyrotron operating in TE_{02} mode at 28 GHz. The longitudinal and transverse views of cavity are shown in Fig. 3.5, and Fig. 3.6, respectively. The dimensional parameters can be described

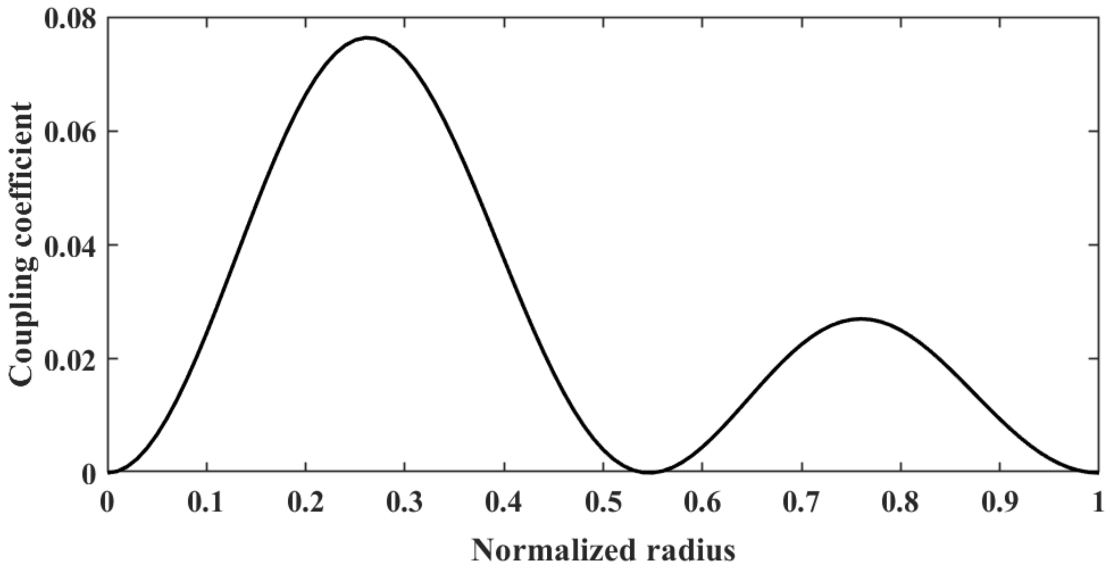

Fig. 3.4: Coupling coefficient of TE_{02} mode.

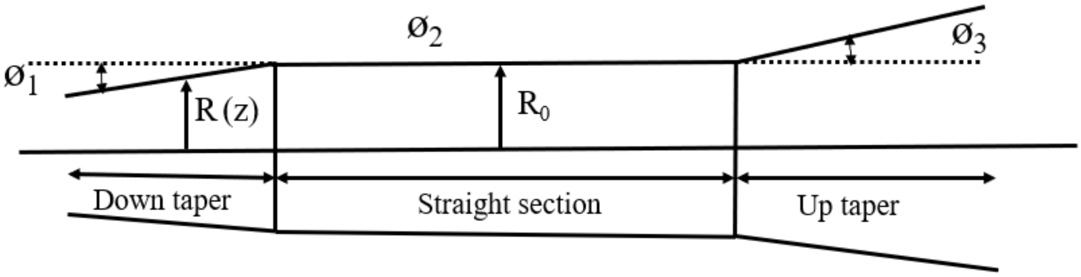

Fig. 3.5: Longitudinal section of the cavity

as follows: $R(z)$ is the radial profile of the cavity. R_0 is the radius of straight section of the cavity. ϕ_1, ϕ_2 and ϕ_3, are the input, straight, and output taper angle, respectively. The beam and larmor radius are denoted by R_b and R_L, respectively.

In single mode analysis, the dependence of the relativistic factor of electron on axial coordinate and the dependence of magnetic field on the axial coordinate are neglected. These two factors are usually very week, and can be neglected particularly for low or medium power gyrotrons [128].

The governing coupled equations (3.10) and (3.11) can be written as [128]:

$$\frac{d^2 f}{d\varsigma^2} - i\frac{df}{d\tau} + \delta f = I_b \frac{1}{2\pi} \int_0^{2\pi} p_c d\theta, \tag{3.10}$$

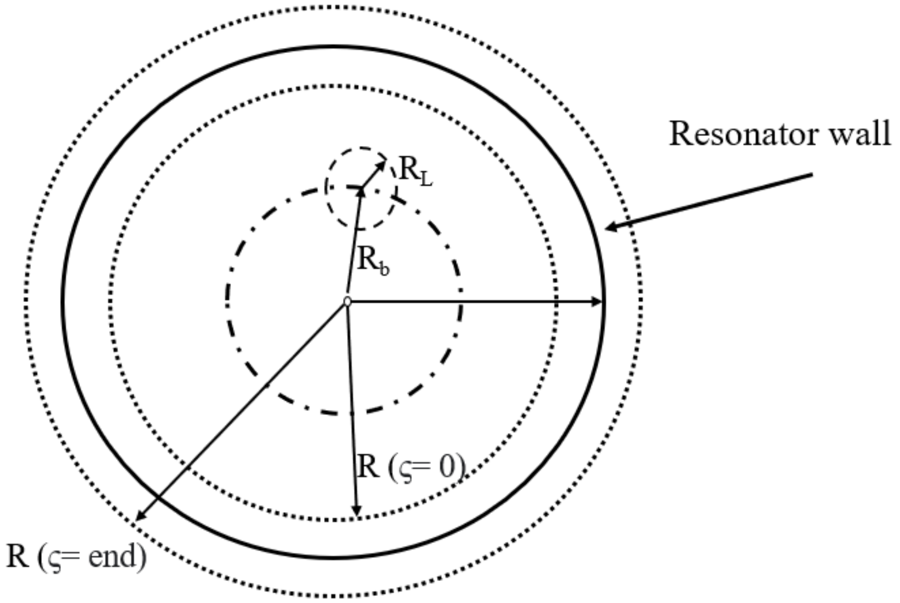

Fig. 3.6: Transverse section of the cavity

$$\frac{d^2 p_c}{d\varsigma^2} + i(\Delta + p_c^2 - 1)p_c = if(\varsigma, \tau) \tag{3.11}$$

The various variables used to solve (3.10) and (3.11) can be defined as follows:

Input variables

- p_c - Complex transverse momentum of the electron normalized to its initial absolute value.

- m, k - Azimuthal and radial mode numbers

- z- Axis vector.

- α - Velocity ratio or pitch factor. It is defined as the ratio between perpendicular ($V_\perp$) and axial ($V_\|$) component of electron beam velocity (V).

- $R(z)$ - Cavity radius vector.

- R_0 - Radius of the cavity for the uniform section.

- B_0 - Magnetic field.

- f_0 - Initial RF field profile vector. Initial field profile can be considered as white noise.
- $freq_{opt}$ - Optimal frequency of the RF field.
- N_{el} - Number of electrons used in the simulation.
- n - Harmonic number. It is equal to 1 in this case.
- U_c - Beam voltage which gives rise to electron kinetic energy.
- I_b - Beam current [A].

Intermediate variables

- $\omega = 2\pi \,.\, freq_{opt}$ - Optimum angular frequency of the resonator.
- $\omega_{cut} = c \,.\, \nu_{m,k}/R(z)$ - Cutoff angular frequency of the resonator.
- $\beta_\perp = V_\perp/c$ - Normalized electron perpendicular velocity.
- $\beta_{||} = V_{||}/c$ - Normalized electron axial velocity.
- $\omega_{cyc} = \dfrac{eB_0}{m_e\gamma}$ - Electron cyclotron frequency.
- $\varsigma = \dfrac{\beta_\perp^2 \cdot \omega}{2 \cdot \beta_\perp \cdot c}$ - Dimensionless longitudinal coordinate z.
- $R_b = \dfrac{\nu_{m\pm n}, 1 \cdot c}{2\pi \cdot freq_{opt}}$ - Electron beam radius
- $\delta(z) = \dfrac{8 \cdot (\beta_{||}^2) \cdot (\beta_\perp^{-4})}{\omega_{cyc}} \cdot (\omega_{cut} - \omega_{cut(z)})$ - Normalized frequency mismatch.
- $k_{zend} = \dfrac{2 \cdot c \cdot \beta_{||} \cdot \beta_\perp^{-2}}{\omega_{cyc}} \cdot \sqrt{\dfrac{\nu_{m,k}^2}{R_0^2} - \dfrac{\nu_{m,k}^2}{R_{end}^2}}$ - Wave factor at the end of the resonator.

- $\triangle = \frac{2}{\beta_{\perp}^{2}} \cdot \frac{\omega - n \cdot \omega_{cyc}}{\omega_{cyc}}$ - Normalized cyclotron frequency mismatch.
- $\eta_{el} = \frac{(1+\gamma) \cdot \alpha^{2}}{2 \cdot \gamma \cdot (1+\alpha^{2})}$ - Electron compression efficiency.
- $\tau = \frac{\beta_{\perp}^{4} \cdot \omega_{cyc}}{8 \cdot \beta_{\parallel}^{2}} \cdot t$ - dimensionless or Normalized time.

Initial conditions for solving the problem

1. At the beginning, only white noise is existing in the resonator. Therefore, as initial condition, $f_0(\varsigma) = 0.1 \cdot e^{<0 \div 2\pi i>}$ at time $\tau = 0$ for all ς

2. Gyrotrons produce hollow spiralling beam in which electrons are gyrating with larmor radius R_L and moving along the z axis with beam radius R_b. When the beam enters into the resonator space ($\varsigma = 0$), the initial phase of electrons is random. So in the simulation, it can be assumed that θ is equally spaced in the range $< 0 \div 2\pi >$

The parameters adopted in the solution are provided in Table 3.2. The coupled equation (3.10) and (3.11) are solved in MATLAB ode45 solver. The growth of output powers and temporal evolution of RF field energy in the interaction cavity as obtained in MATLAB are provided in Fig. 3.7. The α value is kept constant at 1.7 and the magnetic field values (B) of 1.055 T, 1.05 T and 1.0425 T are considered.

It is observed that as the magnetic field value is decreased, longer time is taken to attain a steady output power. However, the value of of output power is greater at lower magnetic field. Lower magnetic field causes greater RF frequency and cyclotron frequency mismatch which pushes the operating point towards hard saturation region. Output power of 18.4 kW with 46% efficiency is achieved by employing the magnetic field of 1.0425 T. However, if the the magnetic field value is reduced further, the output power is not generated due to greater frequency mismatch. Fig. 3.7(d) shows the temporal evolution of RF field energy in the cavity. Initially, the energy distribution was considered to be constant. The Gaussian kind of distribution is evolved

Table 3.2: Parameters adopted in the solution.

Parameters	**Value**
Operating mode	TE_{02}
Harmonic Number	1
Number of Electrons	64
α	1.7
Resonator Radius	11.97
Resonator Angle	2; 0; 3 deg
Resonator Length	48; 70; 75 mm
Step in axial direction	0.05 mm
Frequency	28 GHz
Cathode Voltage	40 kV
Frequency	28 GHz
Magnetic Field	1.055, 1.05, 1.0425 T
Electron Beam Radius	3.13 mm
Time Step	0.05 ns
Cathode Voltage	40 kV
Beam Current	1.0 A

over the time. The field energy is maximum in the middle of the cavity. The field energy is zero at the input taper end as this acts as cut off section for the operating mode.

3.4 Particle-in-cell Simulation

Particle-in-cell (PIC) simulations are needed to determine various input parameters, such as, beam voltage, beam current, velocity ratio, beam diameter and magnetic field for achieving maximum output power and efficiency of a VED. In the current study the PIC simulation is carried out in CST Particle Studio (CST PS) to study beam-wave interaction of the medium power TE_{02} mode gyrotron. CST PS is a commercially available tool specialized for the fast and accurate 3D analysis of charged particle dynamics in electromagnetic fields. The PIC solver includes the effect of space charges, relativistic factors and the self-magnetic field of the charge particles propagating in the electro-static, magneto-static and RF field or combinations of all those fields. Various output parameters are obtained, such as, output power, efficiency, spent electron beam energy spectrum, self-consistent mode and frequency of gyrotron.

The interaction cavity is considered for simulation region for PIC. A truncated conical virtual electron emitter is placed at the at the beginning of the cavity to inject electron beam with

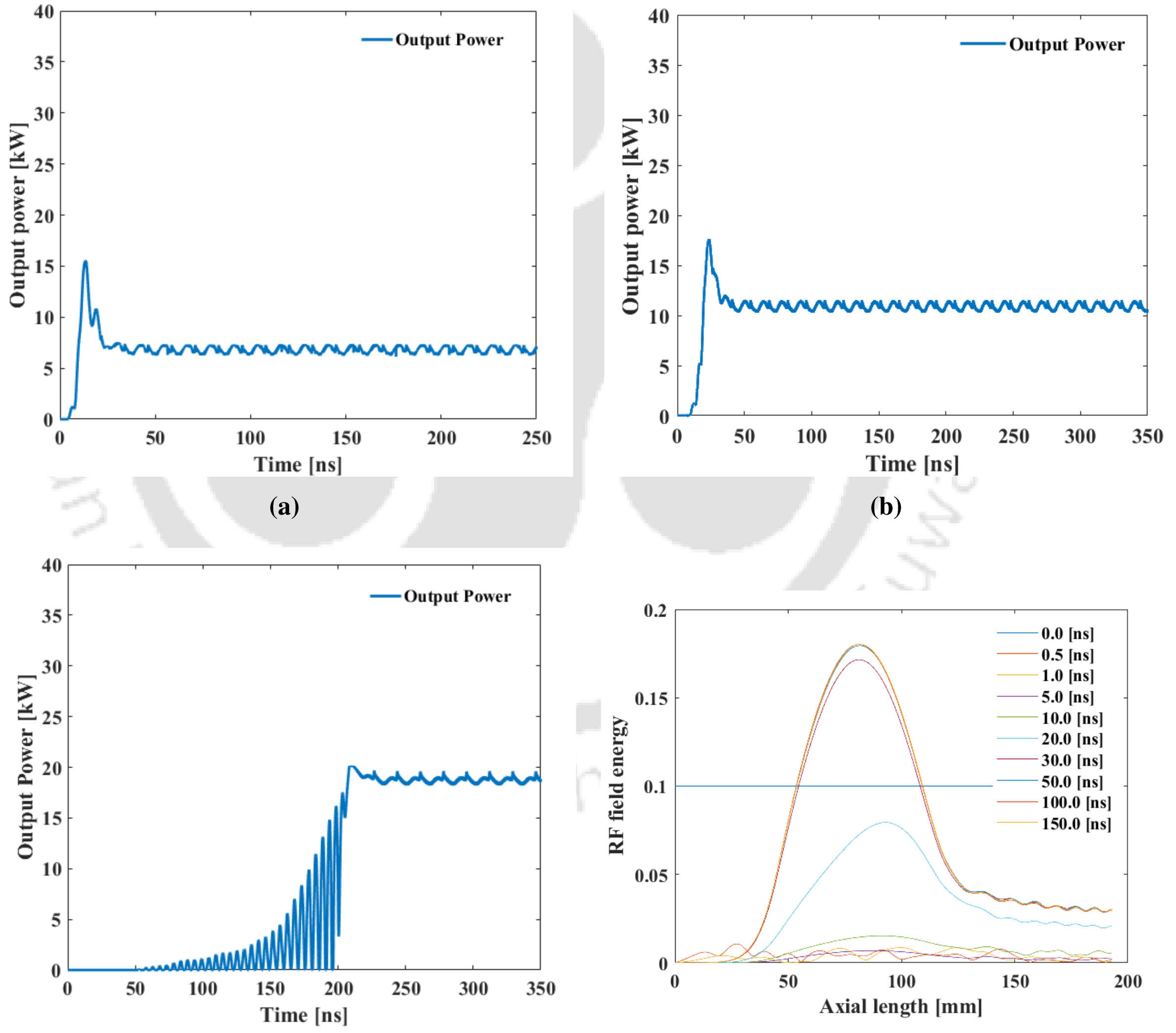

(a) (b) (c) (d)

Fig. 3.7: The growth of output powers and temporal evolution of RF field energy in the interaction cavity: (a) growth of output power for B =1.055 T, (b)growth of output power for B =1.05 T, (c) growth of output power for B =1.0425 T, and (d) Temporal evolution of RF field energy from white noise with respect to axial distance of cavity.

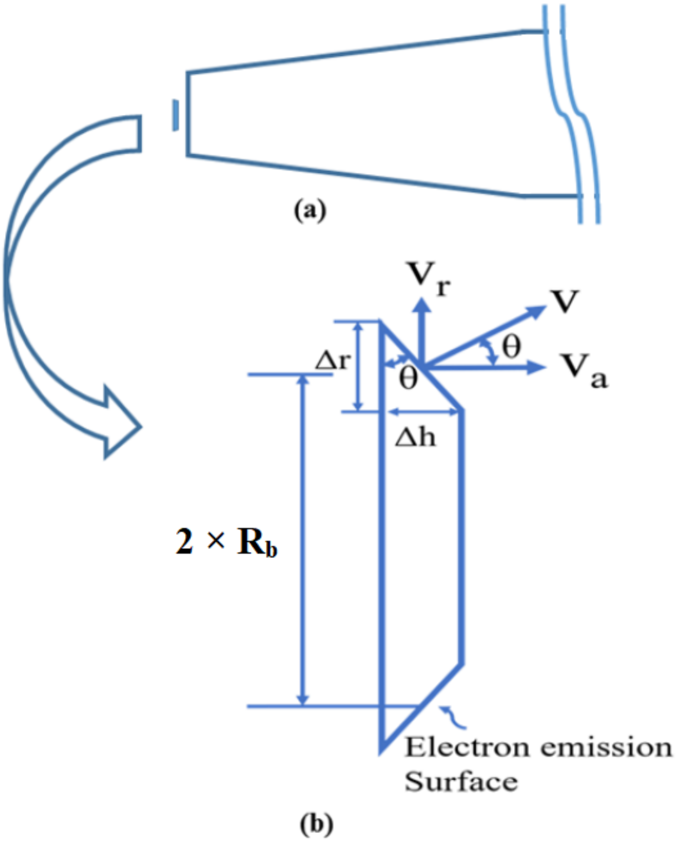

Fig. 3.8: Position of virtual cathode and magnifying view depicting velocity ration (α).

specified diameter, beam current and velocity ratio (α). Fig. 3.8 shows the virtual cathode which is placed concentrically at the entrance of the cavity. The electrons eject perpendicularly from the emitting surface of the virtual cathode. The electron velocity (υ) has both radial component (υ_r), and axial component (υ_a). Therefore, based on the Fig. 3.8, (3.12) can be written.

$$\alpha = \frac{\upsilon_r}{\upsilon_a} = \frac{\upsilon \times \sin(\theta)}{\upsilon \times \cos(\theta)} = \tan(\theta) = \frac{\Delta r}{\Delta h} \tag{3.12}$$

It may be noted from (3.12) that the α can be varied simply by changing the angle θ. In the current study, PIC simulation is carried out to evaluate and optimize various output parameters of the 28 GHz medium power TE$_{02}$ mode gyrotron. A DC emission model with 1 A beam current is assigned for the electron beam. The electron energy is assigned to be 40 keV that an electron will acquire after 40 kV accelerating voltage. A uniform magnetic field is applied through analytical source field in CST PS. A time signal is recorded at the waveguide port assigned at the output end of the cavity from which the output power can be calculated. A

PIC position monitor is applied to observe the electron beam at a specified time interval of the simulation duration. The evaluation of electron bunch over the time can be observed in the position monitor. Electric field monitor is applied to see the self-consistent electric field. A phase-space monitor is employed to record the energy of various electrons with respect to the axial distance.

Initially, the parameters of the PIC simulation are adopted based on the single mode time dependent approach so that the output power obtained by the two methods can be compared. Considering magnetic field value of 1.0425 T, and α value of 1.7, the output power obtained in the PIC simulation is 18.4 kW whereas the output power for the same set of magnetic field and α is estimated to be 18.2 kW. Therefore, both the techniques are found to be in good agreement.

3.4.1 Effect of Magnetic Field on Output Power

Magnetic field determines the cyclotron frequency of electron. Therefore, it is a critical parameter in a gyrotron. There should be a optimum mismatch between cyclotron frequency and the frequency of the RF field for obtaining maximum power output. The effect of magnetic field (B) on the output power is studied in CST PS. Initially, the values of α and B are taken as 1.4 and, 1.055 T, respectively. The I_{soc} of TE_{02} mode becomes minimum for at B value of 1.055 T. The mode competition is found to be negligible as output power in TE_{02} mode saturates within 100 ns of simulation. The same is expected from the plot of I_{soc} which can be seen in Fig. 3.5, because the I_{soc} of nearest TE_{22} mode is too high to excite it at that magnetic field. The output power is obtained to be 9.35 kW with a poor efficiency of 23.375%. Therefore, the magnetic field is decreased in steps of 0.005 T from 1.055 T to 1.04 T for improving the efficiency. The output power is found to be very sensitive to magnetic field. The power output is increased as the value of magnetic field is decreased. It is observed that the output power saturates after longer simulation time as the duration of mode competition (delay, δ_t) between TE_{02} and TE_{22} is prolonged. The operating magnetic value lower than I_{soc} pushes the gyrotron to operate in hard excitation region to yield more power and efficiency. The output power and the (δ) for saturated output with respect to magnetic field is plotted in Fig. 3.9. The maximum output power of 16.92 kW is achieved at B=1.04 T. However, the power saturates at 1200 ns of

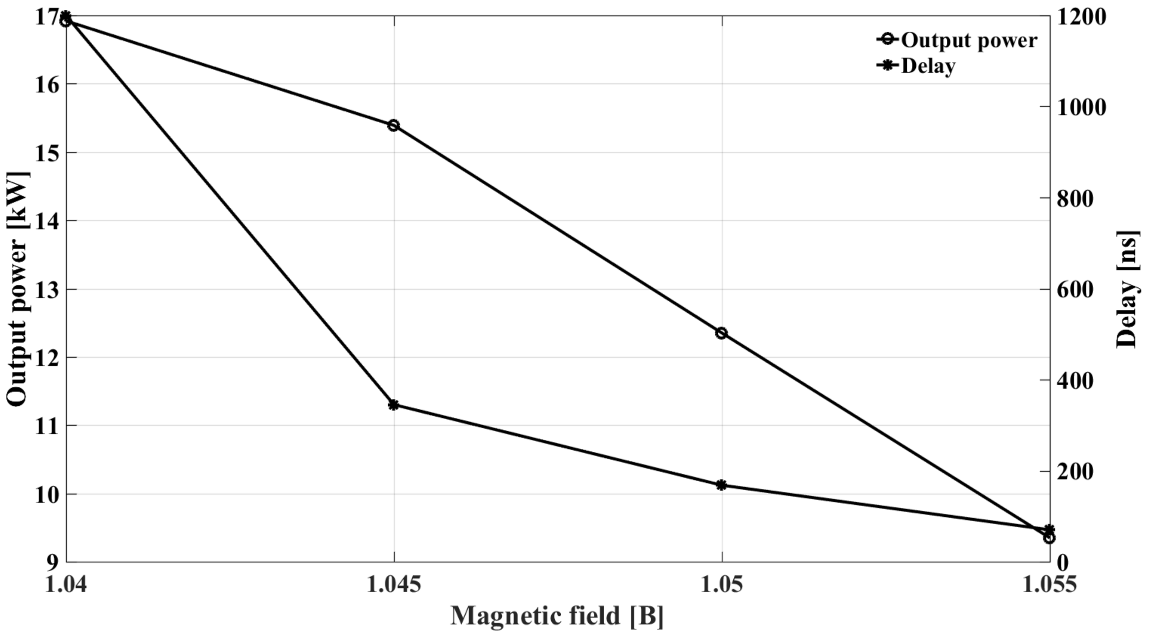

Fig. 3.9: Variation of output power and time delay with respect to magnetic field.

simulation time after a prolong competition with TE_{22} mode.

3.4.2 Effect of Velocity Ratio on Output Power

In a gyrotron, the radial component of electron velocity participates in energy exchange. The radial velocity component can be increased by increasing α. Hence, an attempt is made to increase the value of power output by increasing α in steps from 1.4 to 2.2. It is observed that the greater value of α leads to higher output power and reduction in the duration of mode competition. However, beyond the α value of 1.9, the output power falls sharply. The output power P_0 is obtained to be 20.08 kW at α value of 1.7. After which the power is increased slightly till the α value of 1.9 and thereafter the output power falls. Therefore, the α is chosen to be 1.7 in view of stable operation. In this case, the (δ) is obtained to be 550 ns.

Higher the value of α, more the radial velocity component of electron beam for beam-wave energy transfer. However, after a certain value of α, the output power is decreased as electron beam does not remain in synchronism with the phase of RF field in the cavity. Fig. 3.10 shows the variation of P_0 and δ_t with respect to (α).

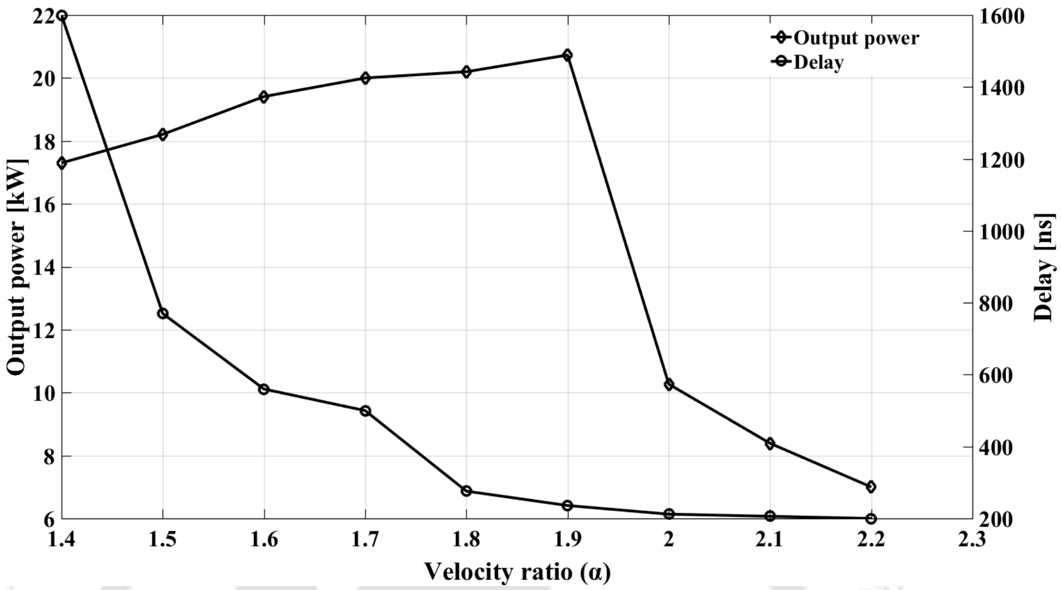

Fig. 3.10: Variation of output power and time delay with respect to (α).

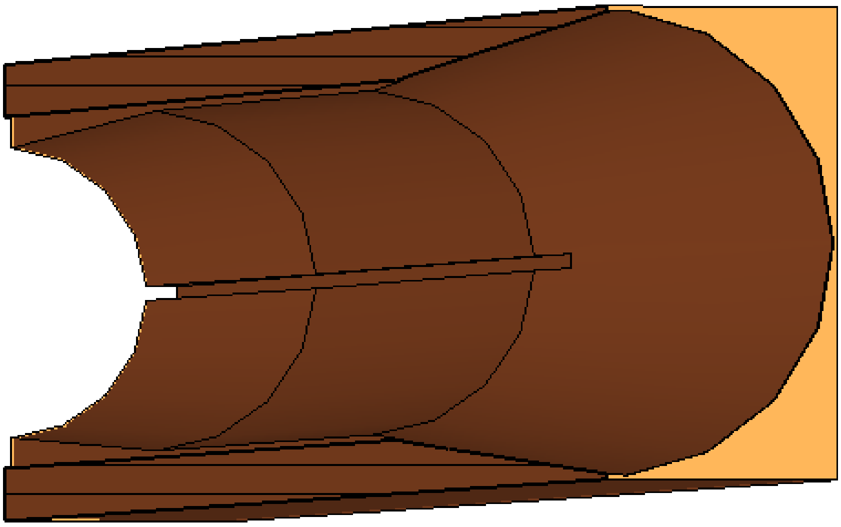

Fig. 3.11: 3D Section view of slotted cavity.

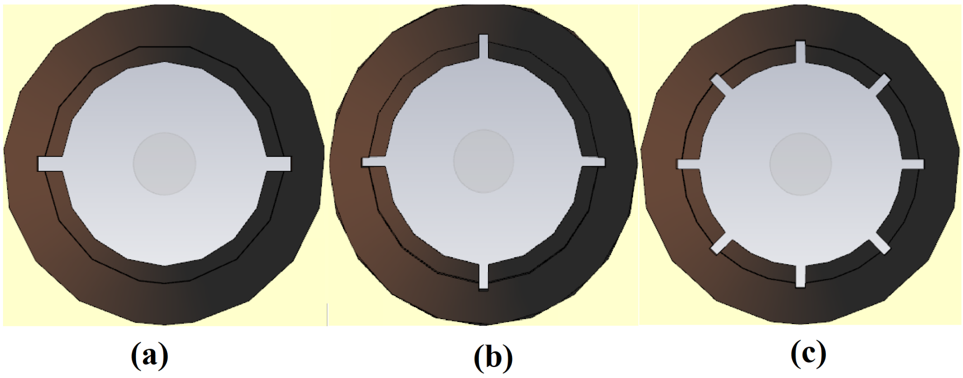

Fig. 3.12: Top view slotted cavity, (a) 2 slots, (b) 4 slots, and (c) 8 slots

Table 3.3: Output power and delay for 2-slot case

d_s (mm)	w_s (mm)	δ_t (ns)	Power output P_0 (kW)
0.25	0.5	540	19.7
0.25	1	335	20.06
0.25	1.5	303	19.2
0.5	0.5	500	19.01
0.5	1	336	20
0.5	1.5	310	18.62
0.75	0.5	290	19.9
0.75	1	226	19.54
0.75	1.5	218	19.2

3.4.3 Elimination of Mode Competition

Mode competition is highly undesirable as they severely hamper the smooth operation of gyrotron. The output section of the device, such as, mode launcher, internal mode converter, and dielectric window are designed for the operating mode only. The undesired mode may cause multiple reflection after getting trapped in the structure. This will cause overheating and arcing in the device. Therefore, the duration mode competition should be curtailed for smooth operation of the device. In the medium power gyrotron under study, axially directed slots are introduced in the inside wall of the cavity. The primary objective of the slots is to disturb the path of the wall current of competing modes. The operating TE_{22} mode being axi-symmetric mode does not contain wall current. Therefore, the operating mode does not get disturbed by the carefully engineered slots. However, the slots add extra path for the wall current of neighbouring TE_{22} mode which reduces the Q value and alters its eigen frequency of the same.

The width and depth of the slots are varied to curtail the duration of mode competition without sacrificing output power. Fig.3.11, and Fig.3.12 show the longitudinal section and top views of the slotted cavity, respectively. The number of equispaced slots are considered to be 2, 4, and 8 in the study. The depth d_s of the slots are varied from 0.25 to 0.75 in 3 steps whereas

Table 3.4: Output power and delay for 4-slot case

d_s (mm)	w_s (mm)	δ_t (ns)	Power output P_0 (kW)
0.25	0.5	417	19.9
0.25	1	285	19.84
0.25	1.5	250.7	20.1
0.5	0.5	310	19.99
0.5	1	250.3	19.7
0.5	1.5	249	18.7
0.75	0.5	279.9	20.04
0.75	1	231.13	18.33
0.75	1.5	163.41	16.15

Table 3.5: Output power and delay for 8-slot case

d_s (mm)	w_s (mm)	δ_t (ns)	Power output P_0 (kW)
0.2	0.25	450	20
0.2	0.5	368	19.8
0.2	0.75	298	19.4
0.4	0.25	334	20.16
0.4	0.5	273.9	19.8
0.4	0.75	195	18.62
0.6	0.25	335	20.02
0.6	0.5	266	19.2
0.6	0.75	218	18.2
0.8	0.25	290.23	20
0.8	0.5	188	17.67
0.8	0.75	162	16.2

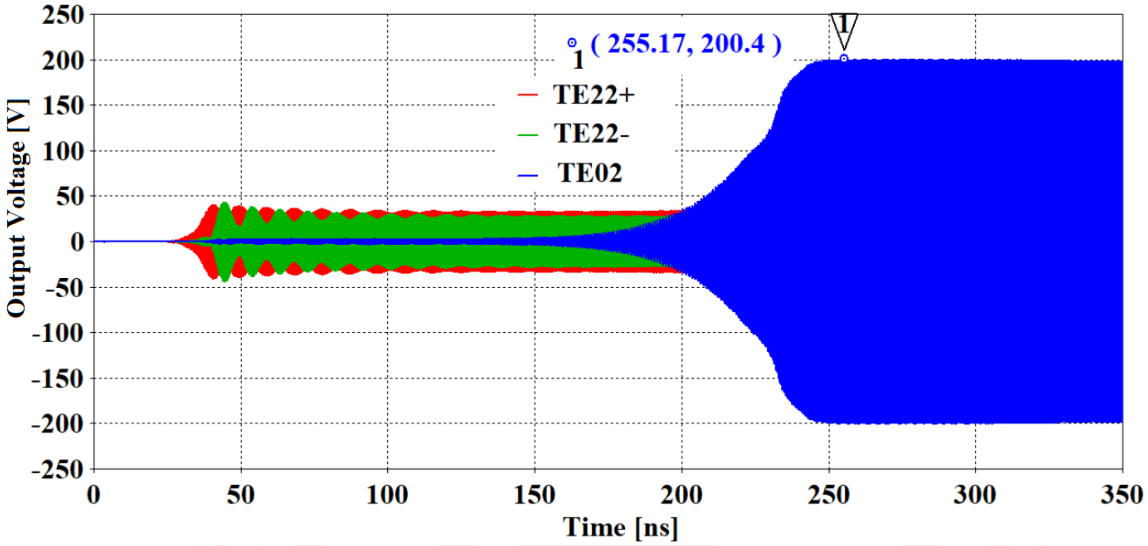

Fig. 3.13: Temporal growth of output power

the width w_s is varied from 0.5 to 1.5 in 3 steps for both 2-slot and 4-slot cases. However, in the case of 8-slot, d_s is varied from 0.2 to 0.8 in 4 steps and w_s is varied from 0.25 to 0.75 mm in 3 steps.

The output power P_0 and delay δ_t for 2-slot, 4-slot, and 8-slot cases are provided in Table 3.3, 3.4, and 3.5, respectively. It is observed that for a fixed d_s, if the w_s is increased, δ_t decreases. However, in view of output power, there should be a right combination of d_s and w_s.

In the PIC simulation, the growth of RF voltage for all the supported modes are recorded in the output port. However, only TE$_{22}$ co-rotating and counter rotating modes excite in the beginning which is suppressed by TE$_{02}$ mode after the delay time. The output power stabilized at 20 kW within 280 ns for 4-slot case when the value of d_s, and w_s are 0.75 mm, and 0.5 mm, respectively. The corresponding delay for conventional cavity is 550 ns. The frequency spectrum is shown in Fig. 3.14. The growth of RF voltage for TE$_{02}$ and TE$_{22}$ mode in the gyrotron are shown in Fig.4.9.

The second peak of the Fig. 3.14 indicates TE$_{22}$ mode which appears at 27.864 GHz. However, the relative magnitude of the same is 40 dB below that of TE$_{02}$ mode. Therefore, the amount of power in the competing mode is negligible.

All the electrons enter the cavity with constant energy of 40 keV. The electrons form phase-bunch due to beam-wave interaction and splits in energies. There should be lower energy elec-

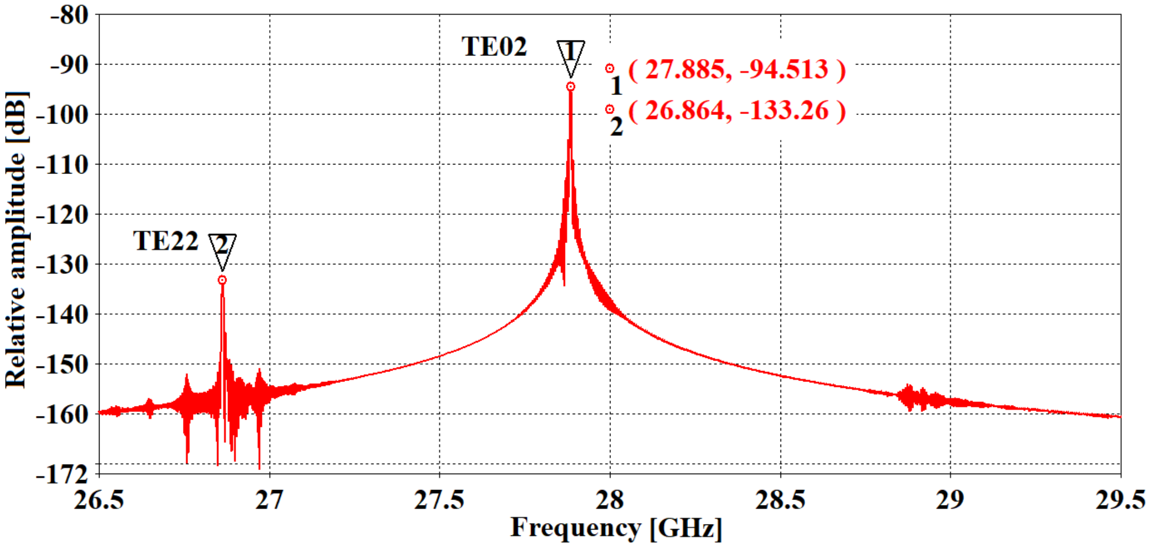

Fig. 3.14: Frequency spectrum of output mode of the cavity.

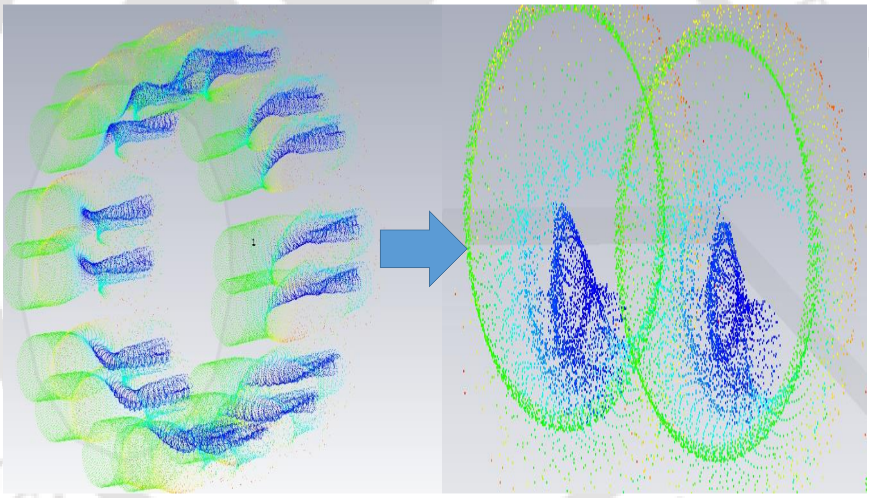

Fig. 3.15: Formation of phase bunch electron after beam wave interaction at the cavity end.

trons as much as possible at the end of interaction region to obtain maximum power transfer from beam to field. The interacted electron beam and magnified beam-lets showing the bunch formation is shown in Fig. 3.15. The energy of electrons is depicted as the spectrum of light. The blue and red colours indicate lowest and highest energies, respectively. However, one should know the quantitative data of spent electron energies like percentage of electrons at a particular energy levels. This will help to design the collector of the gyrotron. The spent beam energy data along with the collector current enable to calculate the efficiency of the depressed collector which is discussed in Section 2.4. The spent beam energy with respect to cavity axis is obtained in CST phase space monitor which is plotted in Fig. 3.16.

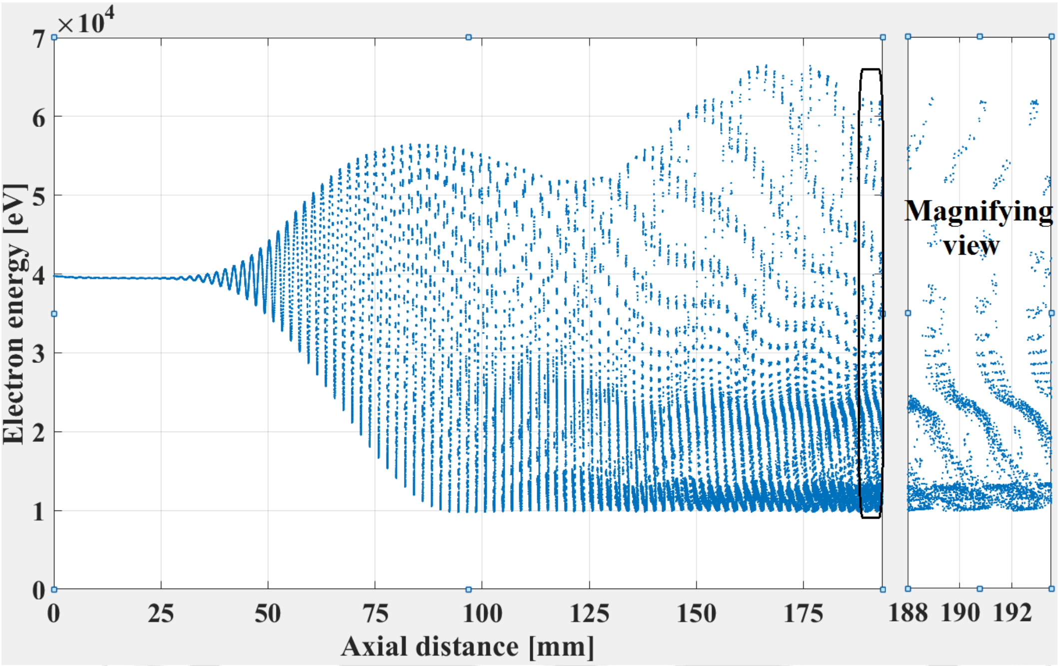

Fig. 3.16: Electron beam energies with respect to cavity axial length.

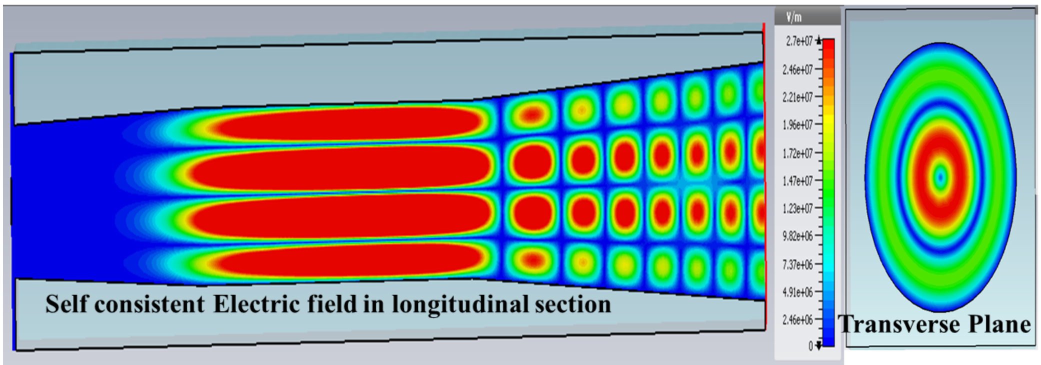

Fig. 3.17: Self consistent electric field in the cavity.

The electric field monitor in CST provides the data for the self-consistent electric field in the interaction cavity. The electric field at both longitudinal and transverse plane is shown in Fig.3.17, which clearly indicates TE_{02} mode operation of the gyrotron. So far, the output powers are computed by considering ideal beam without velocity spread. However, velocity spread in electron beam is inevitable in practice due to non-uniform temperature on the emitting surface, surface roughness and non-uniform magnetic field. Hence, the effect of velocity spread Δv on output power is analyzed by assigning spread in kinetic energy in the electrons emitted from the virtual cathode. As expected, the output power is decreased with the increase of velocity spread. The output power with respect to Δv is plotted in Fig.3.18. A beam velocity spread of

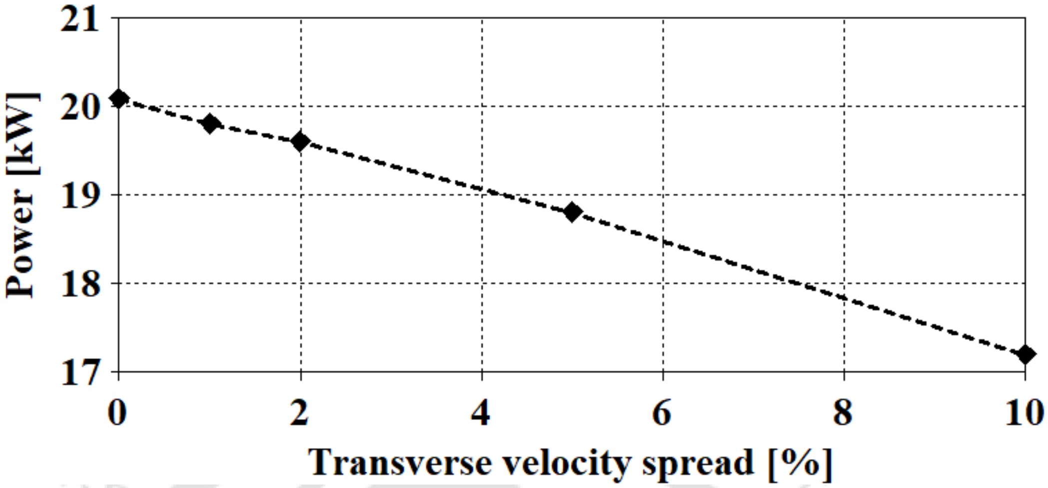

Fig. 3.18: Power output with velocity spread

Table 3.6: Performance comparison.

Parameters	Proposed design	Mitsubishi	GYCOM
Frequency (GHz)	28	28	24
Mode	TE_{02}	TE_{02}	-
Beam Current (A)	1	1	0.75
Beam Voltage (kV)	40	30-21	17.5
Output Power (kW)	18-20	10	6
Efficiency without DC (%)	45-50	30-38.5	45
Efficiency with DC (%)	60-67	-	60

5%, and 10% gives rise to reduction of output power by 6%, and 13.5%, respectively.

The performance of the proposed gyrotron is compared with the medium power experimental Ka-band gyrotrons designed for industrial applications [111], [112] in Table 3.6.

All the industrial gyrotrons in Table 3.6 operate in the frequency range 24-28 GHz. The proposed and Mitsubishi gyrotron operates in TE_{02} mode. However the operating mode in GYCOM gyrotron is not reported. The output power is 6 kW which is minimum in the comparison whereas the proposed design has maximum output power of 18-20 kW. The efficiency with depressed collector of the proposed design is 60-67%, which is maximum in the comparison. However, it may be noted that the output parameters for the proposed gyrotron are estimated at simulation condition.

3.5 Summary

Beam-wave interaction of a 20 kW Ka-band gyrotron is studied. The output power and efficiency of the gyrotron is evaluated by solving single mode time dependent analytical equations. The electronic efficiency is calculated to be 46% using this approach. 3D PIC simulation is carried out in CST to study the beam-wave interaction of the gyrotron. In order to obtain high efficiency, the gyrotron is operated in hard excitation region by lowering the operating magnetic field. The higher value of velocity ratio is chosen to have more transverse energy of electrons which contributes to energy exchange. The electronic efficiency is estimated to 50% in the PIC simulation at a magnetic field 1.0385 T. The operation with lower magnetic field value leads to prolong undesired mode competitions between the operating and neighbouring TE_{22} mode. Therefore, axially directed slots in the cavity wall are introduced to disturb the wall current of the competing mode mode. The depth, width and numbers of the slot are studied for optimizing the power output. The duration of mode competition is eliminated by 50% using this technique. The effect of velocity spread on the output power is studied. The electronic efficiency is reduced to 45% when the transverse velocity spread is considered to be 5%. The self-consistent electric field is plotted which shows TE_{22} mode operation of the gyrotron. The data for the spent electron beam energies are obtained by means of a phase space monitor. The data are analysed for the design and optimization of a depressed collector. The efficiency of the gyrotron using depressed collector is found to be 67.06% which is more than the reported experimental gyrotrons for industrial processing.

4

Width modulated Sine-Waveguide Slow Wave Structure (SWGSWS) for THz TWT

Contents

4.1 Introduction

There was a common perception that Vacuum Electron Devices (VED) will eventually be replaced by solid state devices. However, VEDs still find numerous applications when it comes to high power operation. VEDs are still unmatchable due to their inherent merits such as, higher gain, ruggedness, higher output power, better heat dissipation and radiation resistance in comparison to solid state devices [1]. Researchers explored higher frequency band, such as, Ka-band, V-band, and W-band for TWT operation. However, the THz gap areas ranging from 100 GHz to 10 THz is still remain relatively unexplored. The G-band atmospheric window around 200-250 GHz has various potential applications, such as, high-speed data communications [5]- [8], high-resolution imaging, remote sensing, radars and space observation. The solid state devices even with Group III-V semiconductors can produce only few mWs of power at sub-THz band, which is inadequate for practical applications [1]. At this frequency band, the conventional helix TWT is un-realizable. Therefore, the researchers have shifted focus towards various other interaction structures, such as, planner helical structures [86], [87] diamond supported helix [88] and waveguide SWS structures.

The all-metal slow wave structures (SWSs), [22]- [24], [89] are capable of handling much higher power in this frequency range. They can be fabricated using conventional machining techniques. FWGTWT has a separate beam tunnel for transporting cylindrical beam. The DCW structure exhibits moderate interaction impedance and also supports cylindrical beam. Although, the cylindrical beam technology is very mature, a sheet or a rectangular beam is preferred at elevated frequency, due to higher current carrying capability. The SWG structure is probably the simplest interaction structure to fabricate which does not contain additional beam tunnel. It can support both cylindrical and sheet beams. The structure has become very popular due to lower loss and reflection [130]. The interaction impedance of SWG structure is enhanced by incorporating ridge loading [91]. However, ridge loading inevitably adds fabrication difficulty for the structure. The single-section SWGTWT without an attenuator is reported to produce undesirable reflections during high power operations. The reflected power can even exceeds the input power [89], which is highly undesirable for practical applications. Width-modulation [131] is done on SWS to enhance the interaction impedance by confining the axial electric filed. Sinusoidal width-modulation in SWGSWS is introduced enhancement of interaction impedance.

In the current study, a novel sinusoidal width-modulated single and two-section structures are studied and analyzed. The structure is envisaged to have various advantages, such as (a) enhanced value of interaction impedance resulting higher gain per length characteristics, (b) easy fabrication using conventional machining technique, such as, nano CNC or CNC wire-EDM, (c) elimination of reflected power during hot condition, (d) increase in the surface area because of sinusoidal undulation in the broader side of the waveguide SWS favouring faster heat dissipation.

4.2 Cold Circuit Analysis

The interaction structure of TWT is periodic one where continuous beam-wave interaction happens for amplification of broad band RF input power. The various cold circuit parameters [132] of width-modulated G-band SWG structure are obtained and optimized in CST Microwave Studio [25]. The geometry is basically a conventional SWG structure with sinusoidal variation of the broader side of the rectangular waveguide. A single period SWS with periodic boundary condition is considered in the CST simulation, where Eigen mode solver is used for obtaining dispersion diagram, phase velocity and interaction impedance of the structure. The dimensional parameters of the SWS are optimized to serve the following objectives; (a) to achieve flat dispersion curve for 200-250 GHz frequency, (b) to obtain greater values of interaction impedances, which are required for an intense beam-wave interaction for making the device compact, and (c) larger beam tunnel area for transporting the beam current with minimum beam-metal interception. The unit section of the structure is shown in Fig. 4.1.

The front view shows rectangular cross section ($a \times b$) and position of cylindrical beam of diameter d is provided in Fig. 4.1(a). The sinusoidal variation of the SWS with sine-wave amplitude h is shown in Fig. 4.1(b). The sinusoidal variation of the broader side of the rectangular

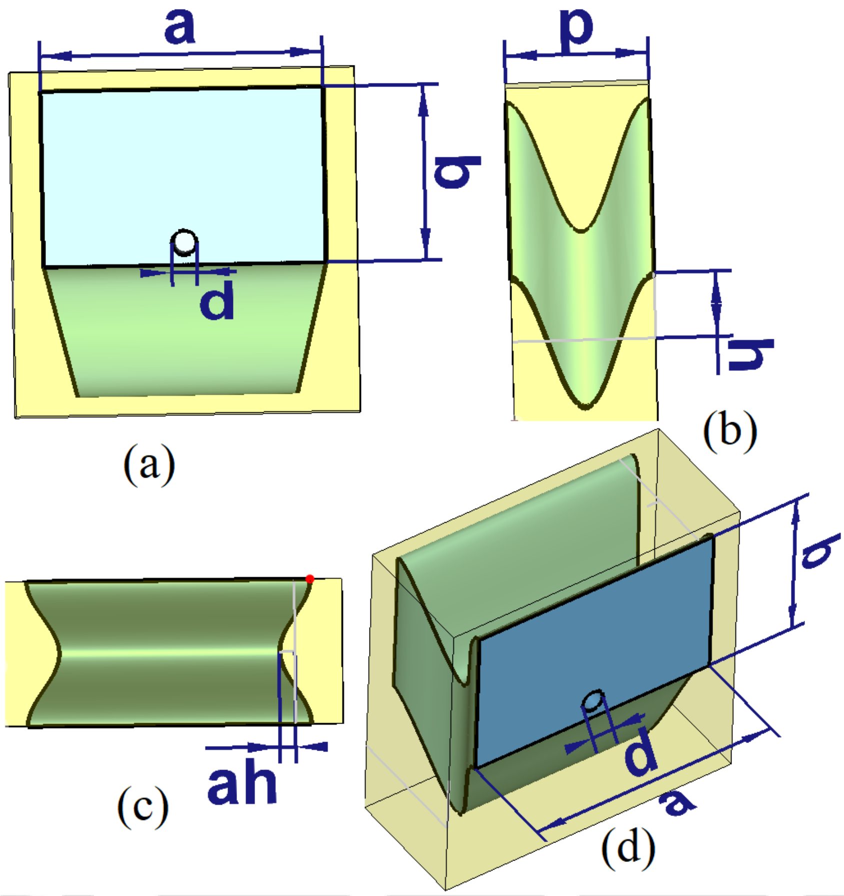

Fig. 4.1: Geometry of the single period SWGSWS, (a) Front view (b) Side view (c) Top view (d) Isometric view.

waveguide due to width-modulation is shown in Fig. 4.1(c) and the perspective view of the unit length is shown in Fig. 4.1(d) The key dimensions of the structure are provided in Table-4.1.

The waveguide SWSs are generally operate in first spatial harmonics region. Hence, the dispersion diagram of the structure is obtained by parametrically varying the phase shift through the single period from 2π to 3π [23] and evaluating the corresponding frequencies. The dispersion diagram of the operating and next higher order mode along with the beam lines are plotted in Fig. 4.2.

It is seen that the 19.7 kV beam-line remains synchronous with the operating mode for the entire frequency range. However, the beam velocity should be higher than the axial phase velocity to have effective amplification. The phase shift per period β is given by(4.1), in which, ϕ is the phase in radian and p is length of period in meter.

Table 4.1: Dimensional parameters of the SWS

Parameters	Value (μm)
Broader dimension of waveguide (a)	900
Smaller dimension of waveguide (b)	560
Length of single period (p)	460
Amplitude of sine wave (h)	210
Width-modulation amplitude (ah)	50
Diameter of the electron beam (d)	45

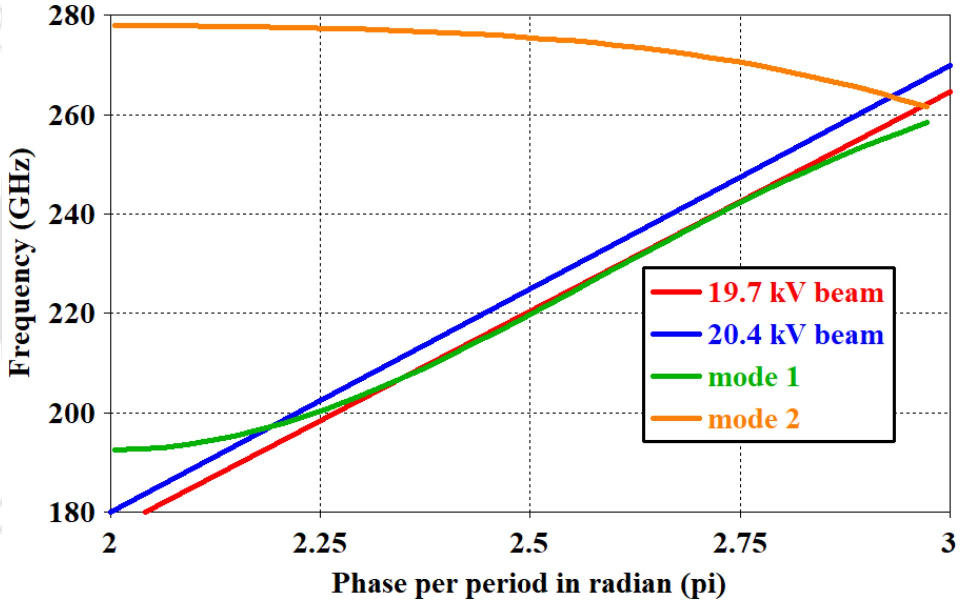

Fig. 4.2: Dispersion curves with beam-lines.

$$\beta = \frac{\phi}{p} \tag{4.1}$$

The axial phase velocity v_p is given by (4.2)

$$v_p = \frac{\omega}{\beta} = \frac{2\pi f}{\beta} \tag{4.2}$$

The axial phase velocity of the structure in terms of velocity of light in free space (c) with respect to frequency is evaluated in CST and plotted in Fig. 4.3.

The phase velocity increases as width-modulation amplitude (ah) increases. The increase

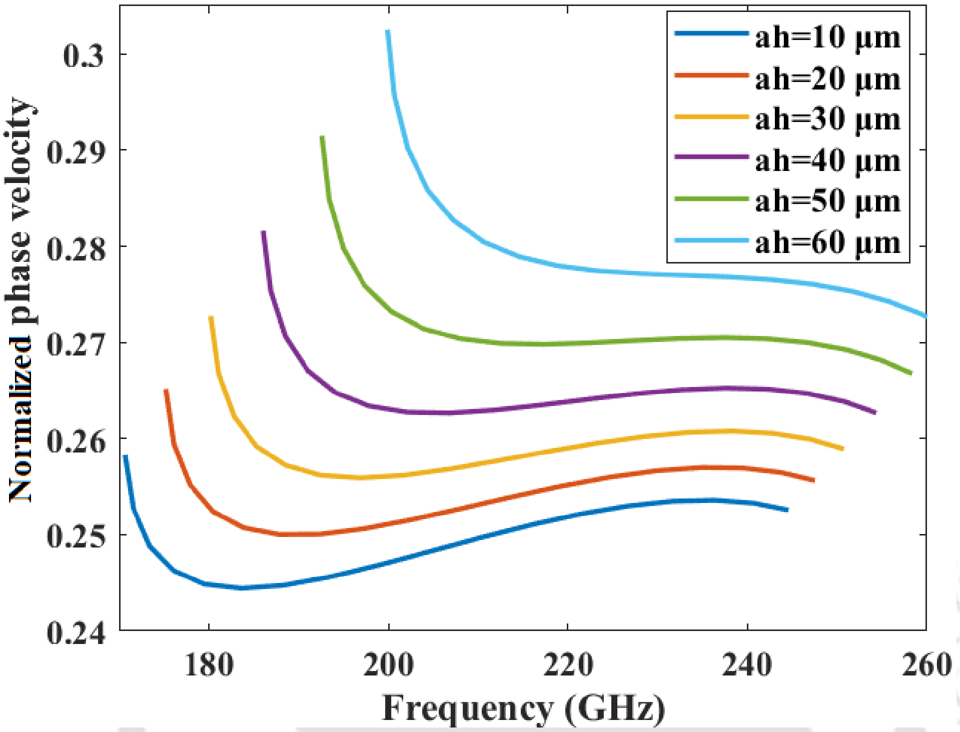

Fig. 4.3: Variation of phase velocities with respect to width-modulation.

of *ah* value pushes the waveguide SWS towards the cut off region. The phase velocity should remain constant over the entire frequency range for wideband operation. The *ah* value of 50 μm gives rise to a flat dispersion over 200-250 GHz range.

Interaction impedance [133] k_n is given by (4.3) .

$$k_n = \frac{1}{2\beta_n^2 P}\left|E_{z,n}(0)\right|^2 \tag{4.3}$$

where, $E_{z,n}(0)$, β_n, and P are the on-axis longitudinal electric field of the n^{th} space harmonic, axial phase shift constant of the n^{th} space harmonic, and the power flow through the structure, respectively. $E_{z,n}(0)$ can be obtained by performing Fourier analysis on the total on-axis axial electric field, which is expressed as (4.4):

$$E_{z,n} = \frac{1}{p}\int_0^p E_z(0)e^{j\beta_n z}dz \tag{4.4}$$

(4.4) can be broken into two parts, which is expressed as 4.5

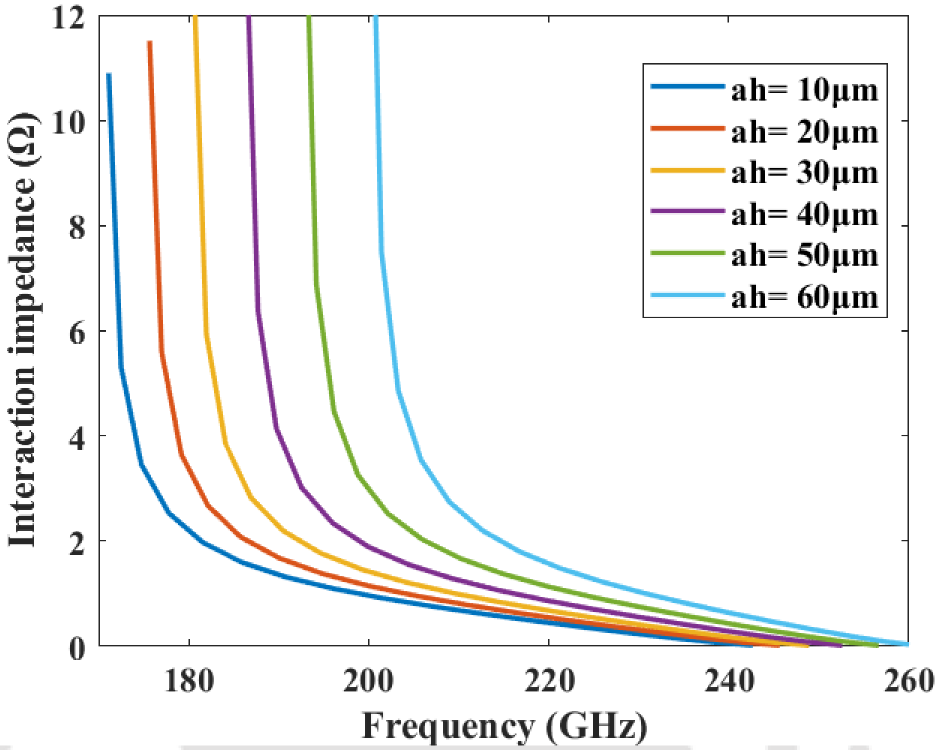

Fig. 4.4: Variation of interaction impedance with width-modulation.

$$E_{z,n} = \frac{1}{p}\int_0^p (R_e[E_z(0)]\cos(\beta z) - I_m[E_z(0)]\sin(\beta z))dz + j\frac{1}{p}\int_0^p (R_e[E_z(0)]\sin(\beta z) + I_m[E_z(0)]\cos(\beta z))dz \tag{4.5}$$

Both the integrals are evaluated by applying template based post processing in CST.

The axial phase constant β_n, and power flow P are given by (4.6), and (4.6), respectively.

$$\beta_n = \beta + \frac{2\pi n}{p} \tag{4.6}$$

$$P = W \times \vartheta_g \tag{4.7}$$

Where β is the fundamental axial phase constant, W is the stored energy per unit length, and ϑ_g is the group velocity RF wave through the structure.

The stronger interaction between electron beam and RF field can be realized by the greater value of the interaction impedance. Therefore, greater value of interaction impedance leads to more gain per unit length which is essential for making the structure compact. The interaction impedance is estimated by template-based post processing in CST for different value of sinusoidal H-plane loading amplitude. Fig. 4.4 shows the variation of k_n with respect to frequency for the different values of ah. The k_n increases as ah increases for a particular frequency as greater value of width-modulation amplitude helps better confinement of the axial electric field in the structure. The higher frequency components exhibit lower k_n as they are far from the cut off frequency which is a common characteristic of SWS.

4.3 Design of Two-section SWGSWS

In general, the interaction structure of TWT consists of three sections, such as, input section, sever section, and output section. The sever section attenuate the backward wave and therefore prevents oscillation in the device. The backward wave or reflection from the input port are detrimental for the input power driver source. The reported SWGTWTs in [24], [91] consist of a signal section, without any sever. Single-section SWGTWT reported in [89] exhibits strong reflection of power during high power operation. The reflected power even exceeds the input power that is highly undesirable for smooth functioning of TWT. Therefore, in the current work, an attempt is made to study a two-section SWG interaction structure, in which the first section consists of input coupler, first SWS (pre-bunch section), intermediate coupler and attenuator, whereas the second section consists of second SWS and output coupler. The interaction structure is shown in Fig. 4.5.

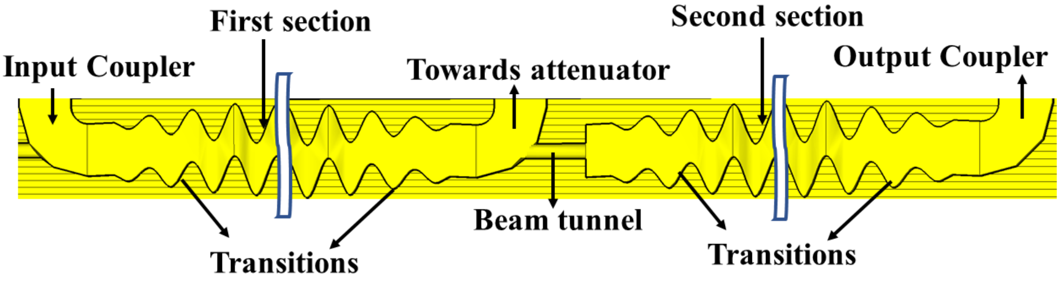

Fig. 4.5: Geometry of the two-section SWG interaction structure.

There are 65 periods in the first section of the SWS to provide weak bunching of the electron beam. The sinusoidal variations at both plane are gradually increased from the rectangular port to the SWS region for obtaining smooth transmission of RF power. The electrical conductivity of OFHC copper is taken to be $\frac{\sigma_{cu}}{3}$, where, σ_{cu} is the conductivity of OFHC copper given by 5.8×10^7 S/m. It may be noted that the machine surface exhibits lower effective conductivity [134] given by (4.8).

$$\sigma_{eff} = \sigma_D \{1 + \frac{2}{\pi} \arctan \langle 1.4 (\frac{h}{\delta})^2 \rangle \}^{-2} \tag{4.8}$$

Where, σ_D is the conductivity of the un-machined or smooth surface, σ_{eff} is the effective conductivity of the machined surface, h_s is the RMS height of the surface, and δ_s is the skin depth in the case of the flat surface. The skin depth in the current study is calculated based on highest frequency of operation 250 GHz. A Ra value of 400 nm corresponds to the normalised effective conductivity value of 1/3. Although Ra value < 300 nm can be achieved in practice, it is considered to be 400 nm in the study in view of a worst-case scenario.

An intermediate coupler with attenuator is introduced so that the power generated in the first section is absorbed. The attenuator is to be made separately and placed at the specified position as shown in Fig. 4.6. This helps to electrically isolate both the sections. The first section acts as pre-bunch section and the second section intensifies the electron bunch and yield the output power. An attenuator is designed in the frequency-domain solver of CST.

Lossy dielectric material BeO-SiC composite [135], [136] is chosen as an absorbing material. The dielectric constant and loss tangent values are considered to be 6.5 and 0.5, respectively. The position and geometry of the attenuator are shown in Fig. 4.6.

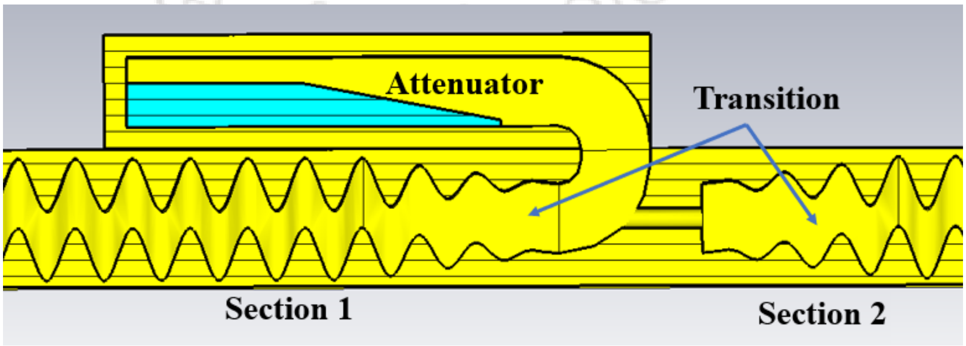

Fig. 4.6: Geometry and position of the attenuator.

The attenuator has a taper section and a straight section, which exhibits wideband frequency response. The return loss of the attenuator is achieved such that a little reflection is experi-

Table 4.2: Dimensional parameters of the Attenuator

Parameters	Value (μm)
Width of the waveguide	900
Height of the waveguide	560
Length of the taper section	1600
Length of the Straight section	1400
Total length of the attenuator	3500
Thickness of the dielectric-tip	50
Thickness of the dielectric (t_{di})	200

enced and the power get absorbed gradually by the lossy dielectric material. The dimensional parameters are provided in Table-4.2.

The S_{11} of the attenuator for various thickness value of dielectric (t_{di}) is shown in Fig. 4.7. The t_{di} value can be chosen as 0.35 mm in view of better return loss value over the frequency range. The minimum value of S_{11} is 17 dB at 200 GHz. However, the reflection improves as the frequency increases.

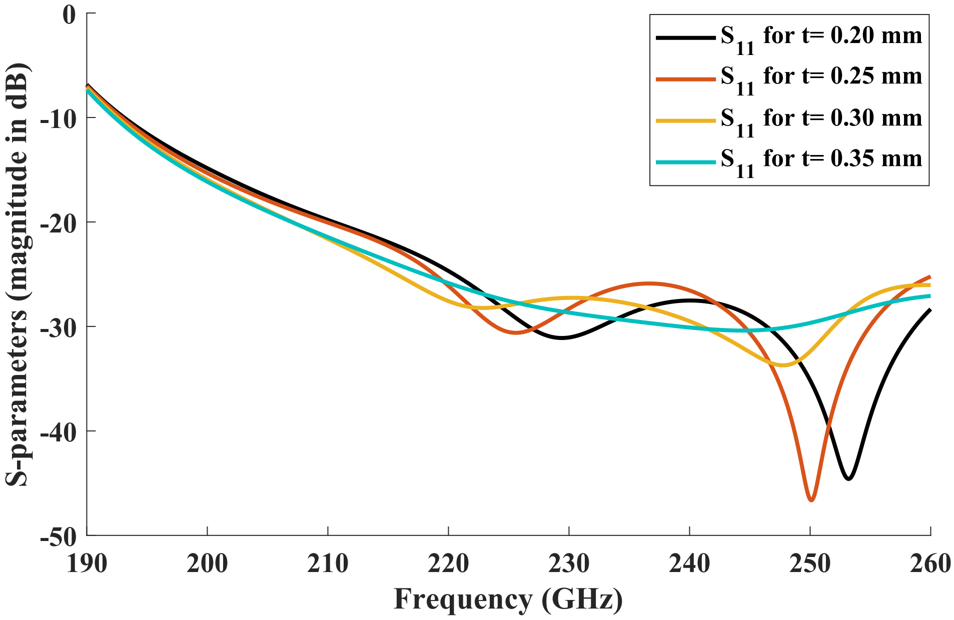

Fig. 4.7: S-parameters of the attenuator.

The reflection coefficient (S_{11}) of the attenuator along with the first section considering the

t_{di} value of 0.35 mm is provided in Fig. 3.11. The S_{11} value is found to be close to 20 dB for the frequency range 195- 256 GHz, except a few points.

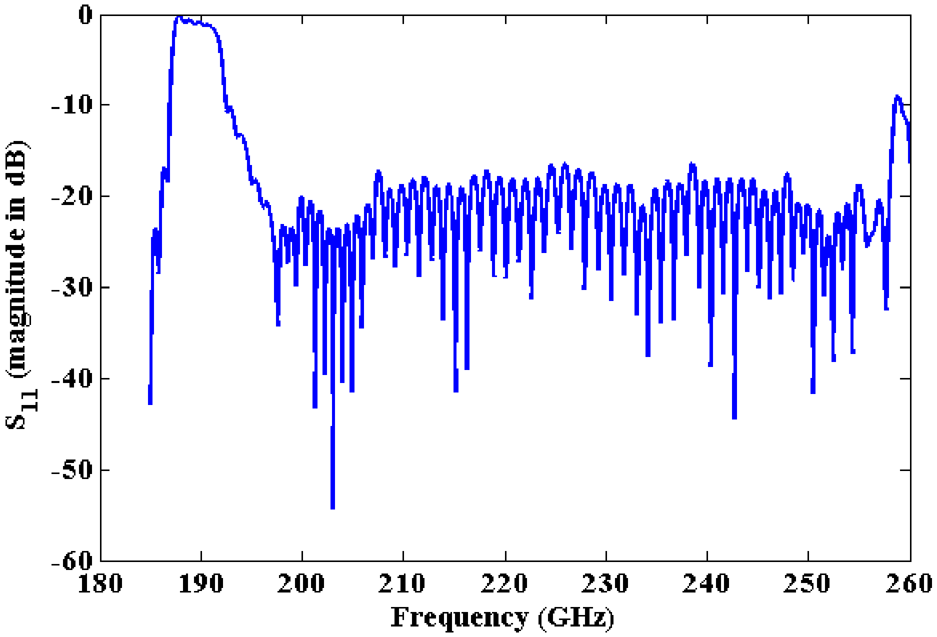

Fig. 4.8: S-parameters of the first section of the interaction structure.

The two-section approach effectively minimise the reflection at hot condition which is illustrated in the Section 4.4.

4.4 Particle-in-Cell Simulation of Width Modulated TWT

The high power behaviour of the width modulated single-section as well as two-section structure are analyzed in Particle-in-Cell (PIC) solver of CST Particle Studio. The RF Input is supplied through the rectangular waveguide port of the input coupler in the dominant TE_{10} mode. A waveguide port at the input coupler is assigned to excite a sinusoidal signal of specified frequency and power. The sinusoidal undulation of the SWS, converts the TE_{10} mode into hybrid mode. In this process the axial electric field components arises in the interaction region, which is essential for energy exchange with linear beam. A virtual cathode is placed at the input side of the TWT to generate electron beam of specified current and voltage. DC emission model is adopted in CST PS. In the beginning, the single section structure is simulated. The beam voltage is considered to be 19.7 kV, as the beam line synchronize with the RF axial-phase, as shown in Fig. 4.2. There is no significant output power recorded at the output port as the net beam-field energy transfer happens to be negligible. The beam velocity should be higher than the RF axial-phase velocity to realize net transfer of energy from beam to field. Therefore, the beam voltage is increased gradually. The interaction impedance of the structure decreases with the increase of frequency which is shown in Fig. 4.4. As a consequence, the electron beam for the lower frequency side of the operating band gets bunched at relatively shorter interaction length. In fact, further increase of interaction length causes de-bunching leading to reduced output power. At the same time, longer interaction length is required for higher frequency components for the formation of optimum bunching. Therefore, the length of the interaction structure should be chosen judiciously to satisfy mutually contradictory requirements. Similarly, lower frequency required lower input power in comparison to the high frequency counterpart for achieving highest saturated gain. In the current study, beam voltage and length of the output section are gradually increased for maximizing the amplification of the entire frequency band. The single section structure provides 53 W output power with a gain of 30.25 dB at 210 GHz for a circuit length of 160 periods. The reflected power recorded at the input port is 38.5 mW which is 77% of the input power.

After optimizing the single section structure, a PIC simulation of the two-section structure is carried out. In this case, the aim of the first section is to have a weak beam-wave interaction for producing pre-bunched electron beam. The combination of the applied input power and number of periods in the input section, determine the quality of bunching for the entire frequency range. The higher frequencies require higher power or longer interaction length due to lower interaction impedance value and vice-versa. The length of the input section is determined to be 60 periods after number of iterations. The RF power generated in the first section gets absorbed in the attenuator discussed in Section 4.3. The pre-bunched electron beam enters the second section of the TWT through the beam tunnel for the final amplification process of the RF signal. Although, the input signal does not enter the second section, the velocity modulated beam carries the information of the input signal. The beam voltage and the length of the output section are gradually increased for optimization of gain for the entire frequency range. The optimized

Table 4.3: PIC Parameters

Parameters	Values
Beam Voltage	20.4 kV
Beam current	50 mA
Beam diameter	45 μm
Magnetic field	0.6 T
Power input	50 mW
No. of periods in the first section	60
No. of periods in the second section	120

value of the length of the output section and beam voltage are found to be 120 periods and 20.4 kV, respectively. The various parameters of the PIC simulation are given in Table 4.3.

The output power and gain of the two-section structure for various input power levels are plotted in Fig. 4.9 at 215 GHz.

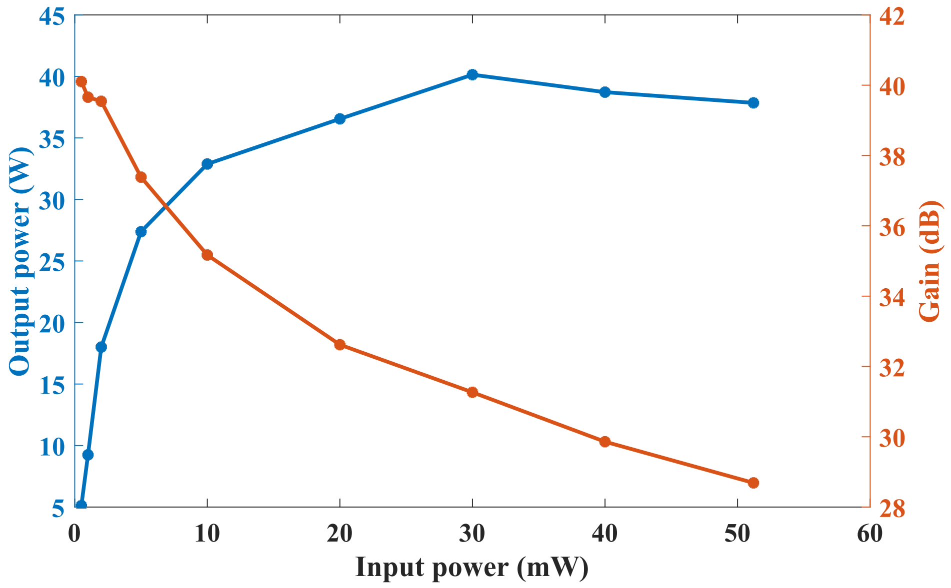

Fig. 4.9: Gain and output power versus input power at 215 GHz.

Initially, the output powers are increased linearly with respect to input powers. However, after a certain point, the gain reduces due to non-linearity of the TWT amplifier. However, the output power reached a maximum value of 40.2 W for 30 mW power input. After that the output power slightly reduced. This happens as the beam bunches continue to improve till

30 mW of input power after which, due to de-bunching the output falls. However, in view of higher frequencies which experience relatively lower interaction impedance, the input power is set at 50 mW after going through a few iterations. The solid state power amplifier (SSPA) or backward wave oscillator (BWO) can be used as a RF source. The large signal gain for the two-section structure is estimated to be 28.9 dB. The output powers are obtained at various frequency points in the 198-245 GHz band. The maximum power of 38.9 W is estimated at 213 GHz with an efficiency of 3.81%. The half-power bandwidth of the two-section TWT is found to be 32.5 GHz from the frequency range of 200-232.5 GHz. A power output greater than 10 W is achieved for the entire frequency range 198-245 GHz. The output powers of single section and two-section structures with respect to frequency are plotted in Fig. 4.10.

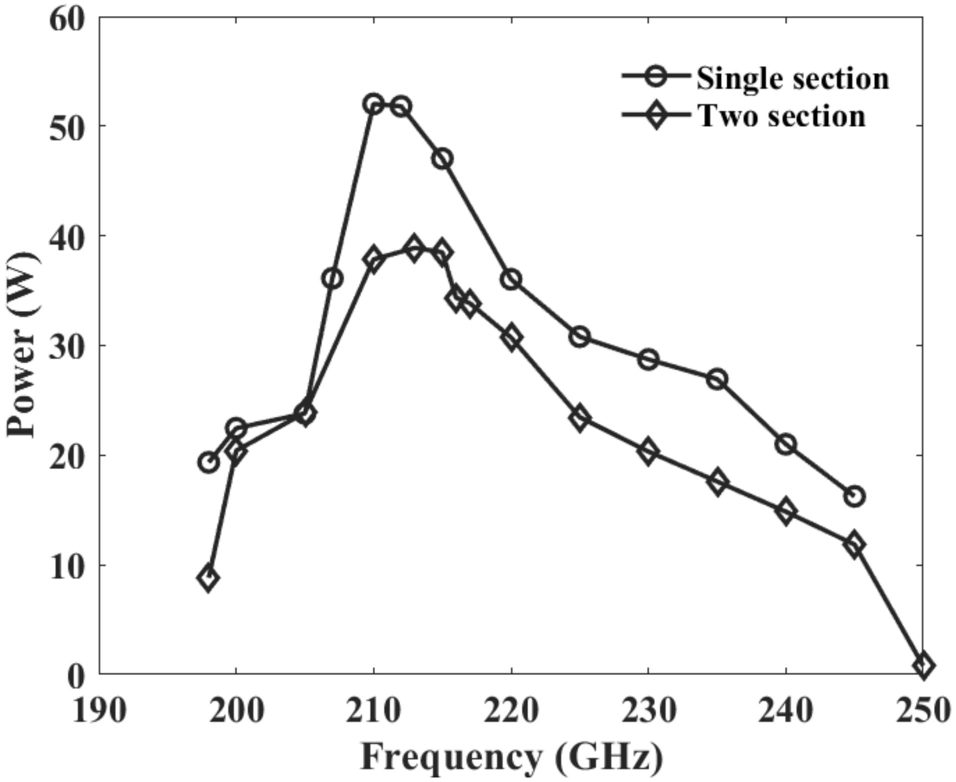

Fig. 4.10: Output powers of single and two-section with frequency.

It is noted that the single structure exhibits higher output power for the entire frequency range in comparison to the two-section structure. The gain per unit length of the single section and two-section structure is found to be 4.11 dB/cm, and 3.49 dB/cm, respectively. The fact of the matter is the two-section structure sacrifices some gain acquired in the first section as the generated power in this section get absorbed by the attenuator. However, this helps to isolate both the sections in terms of propagation of RF wave. The reflected power of the two-section structure is only 0.659 mW, which amounts 1.31% of the input power. Thus, the two-section structure eliminates the reflection by $\frac{(38.5 - 0.66)}{38.5} \times 100 \approx 98.29\%$. The two-section structure certainly has reduced gain characteristics when compared to the single-section structure, it is very effective to minimize the reflection of the RF power during high power operation. The temporal growth of reflected and forward powers for the single-section as well as two-section SWGTWT are provided in Fig. 4.11.

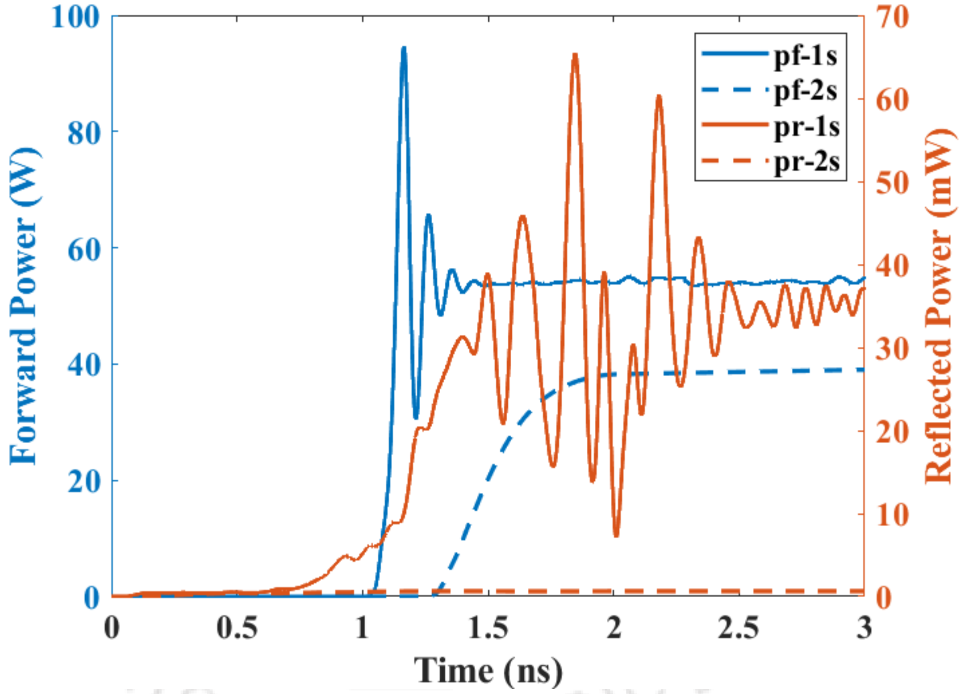

Fig. 4.11: Growth of forward and reflected power with time. Pf-1s and Pf-2s are forward powers of one-section and two-section structures, respectively. Pr-1s and Pr-2s are reflected powers of one-section and two-section structures, respectively.

The TWT acts as amplifier that does not shift the spectrum of the input signal. In the PIC simulation, sinusoidal tone signal is employed as input. The spectrum of output signals are evaluated by taking Fast Fourier (FFT) in CST post processor. The spectrum of input and amplified output signals for different frequencies are provided in Fig. 4.12. As expected, the spectrum of the output signal appears at the same frequency point that of input signal with a finite gain revealing TWT operation.

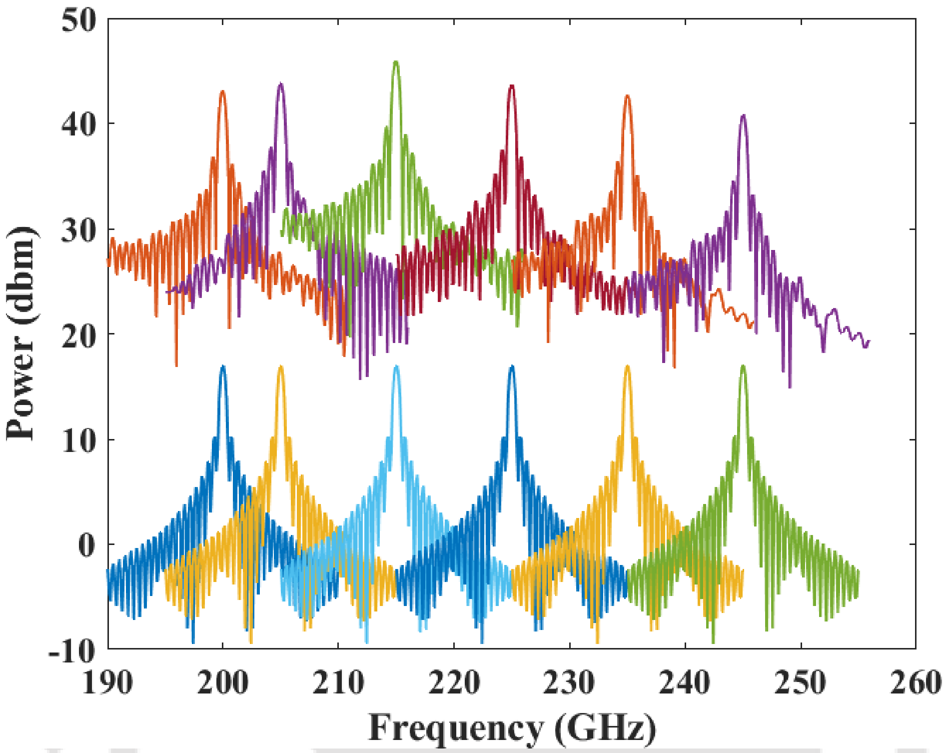

Fig. 4.12: Input and output spectrum for the discrete frequency points in the operating frequency band

The pencil beam enters the interaction space with constant energy 20.4 keV due to accelerating anode voltage. The electrons facing accelerating phase of the RF signal get accelerated whereas the electrons facing retarding phase get decelerated. The velocity modulation leads to density modulation and formation of beam bunches as the beam travels through the SWS. The net beam to field energy transfer will happens provided the beam loss its energy. A phase-space monitor is applied in CST to monitor the electron energy with respect to axial distance. The energy distribution of the velocity modulated electron beam over the interaction length is shown in Fig. 4.13. The initial energy of electron beam is shown by the yellow line. Majority of electrons lose their energy as the beam reached the final section of the SWS which corroborates a net beam-field energy transfer.

The formation of beam bunches for last 60 periods of the SWS are shown in the inset of Fig. 4.13. The energy of electrons is coded as per the spectrum of light in which the red colour indicates highest energy and blue indicates lowest energy.

In order to study the relative performance of the proposed two-section (2S) and single-section (SS) width-modulated SWGTWT, the various parameters of the reported G-band waveg-

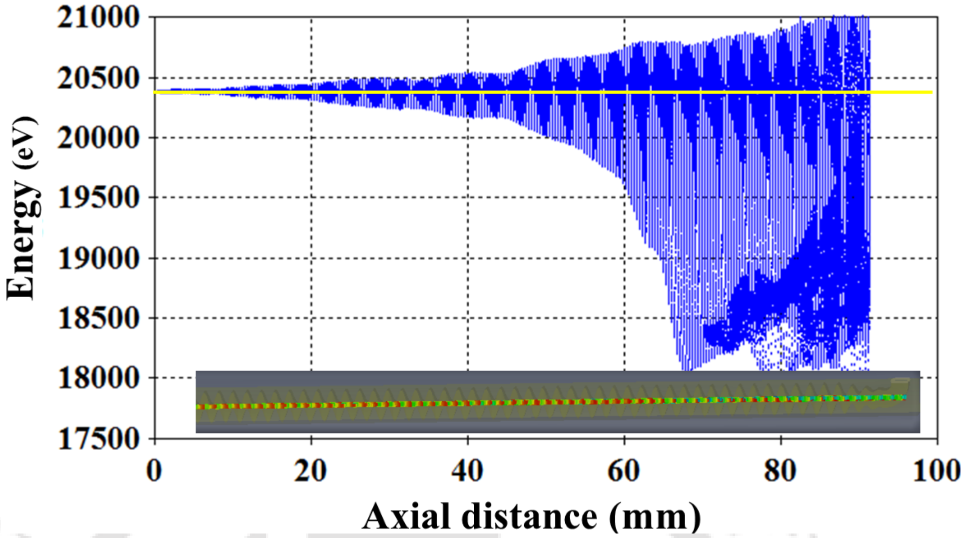

Fig. 4.13: Distribution of beam energies over the axial length. Inset: beam-bunch for last 60 periods of the SWS.

uide based TWT are compared with width-modulated TWT structures in Table 4.4.

Table 4.4: Comparison of Proposed TWT with Existing Literature

Structure Type (SWS)	P_{out} (W)	V_a (kV)	I_b (mA)	B (T)	η %	P_r (mW)	BW (GHz)	G.p.U (dB/cm)
Proposed design (2S)	39.5	20.4	50	0.6	3.81	0.66	32.5	3.49
Proposed design (SS)	53.0	20.4	50	0.6	5.19	38.5	30.0	4.11
DCW [23]	1	13	20	0.6	1	-	30	3.27
RLSWG [91]	52.1	20.9	45	0.7	5.54	-	25	3.71
Plane SWG [89]	300	20.8	150	1.4	9.6	200	44	-

A plain SWG structure reported in [89] provides 9.6% efficiency, which is maximum in the caparison. However, the electrical conductivity of copper in the paper is considered to be 5.8×10^7 S/m which might have led to higher efficiency. Also, the TWT employs a sheet electron beam with relatively higher beam current of 150 mA. The requirement of magnetic field is reported to be 1.4 T, which is very high in comparison to the other reported literature. The SWGSWS being a single-section design, concedes 200 mW reflected power at the input port. On the other hand, the proposed two-section structure has a negligible reflection of 0.66 mW. The single-section width-modulated structure in the current study provides greater gain per unit length in comparison to DCW [23] and RLSWG [91]. However, the two-section design has slightly less gain but broader bandwidth in comparison to RLSWG [91].

4.5 Fabrication of the Scaled Version of Width-modulated Structure

The width-modulated structure has a relatively easy fabrication as the same can be made using conventional machining technique. However, the machining precision required to fabricate the structure at G-band is not achievable in-house. In addition, the characterization equipments like Vector Natwork Analyser (VNA) and coaxial-to-waveguide adaptors are also not available. Therefore, scaled version of the width-modulated structure is fabricated to study the fabrication intricacies and also to measure the cold parameters of the structure. In view of the availability of VNA and adaptors, all the dimensions of the G-band structure provided in Table 4.1 is scaled with a factor 14.66, so that the G-band frequency (220 GHz) is shifted to Ku-band (15 GHz). The structure is simulated in Ku-band for 20 periods with standard input and output rectangular waveguide ports WR62. Proper transition sections are designed for minimizing the reflection. The material of construction is considered to be copper with electrical conductivity σ_{cu}. The simulation model is converted into fabrication model comprising of two equal halves with width-modulated SWG profile at each half. Both the halves can be stacked at the middle of the broader waveguide wall to form the width-modulated SWG structure. In this case, the flow of wall current will not be hampered. The provisions are made for dowel pin arrangement and flanges for precision alignment. Initially, CNC milling is done to make the E-plane profile on the OFHC copper slabs whereas the final H-plane profile is done using EDM techniques. Similar methodology can be adopted to fabricate the structure at G-band. However, miniature tooling and greater machining precision are required at higher frequency. The fabricated parts are cleaned in ultrasonic cleaner using acetone. The oxides and the black spot from EDM are removed by dipping the parts into a solution of hydrogen peroxide, formic acid and distilled water. The cleaned parts are shown in Fig. 4.14.

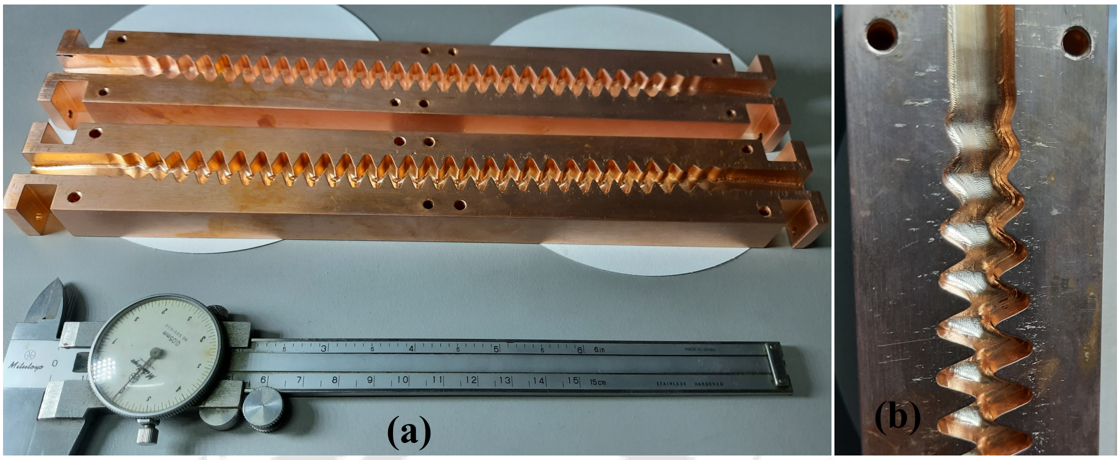

Fig. 4.14: Scaled version of the proposed SWS at Ku-band. (a) Two equal halves with dowel pin arrangement for alignment. (b) Magnifying view showing sinusoidal corrugation at both E and H-planes.

4.5.1 Measurement of S-parameters

The transmission property of the structure is measures after assembling the parts and attaching WR62 co-axial to waveguide adaptors at both ends. A Keysight PNA-L VNA is used for the measurement. Full two port calibration from 12 to 18 GHz covering the entire Ku-band is done till the waveguide ends of the adaptors. The experimental setup is shown in Fig. 4.15.

The SWGSWS exhibits a transmission window covering the frequency range 14.5-17.5 GHz, where the S_{11} and S_{21} are found to be better than -17 dB and -0.5 dB, respectively.

However, one cannot expect exactly same reflection and transmission results in G-band as the results at elevated frequency would be more sensitive towards mechanical tolerance and surface finish. In Fig. 4.16, the simulated and measured results are displayed. A very good agreement is found between the two results. The minor deviations arise due to the fabrication inaccuracy and finite surface finish.

4.5.2 Experimental Measurement of Dispersion Characteristic

The phase angle information of the transmission (S_{21}) signal is processed to obtain the dispersion characteristics of the device [137] by using the following steps:

(a) The phase angle information of S_{21} signal of the SWG structure along with the coaxial to waveguide adapters is obtained. The phase plot is shown in Fig. 4.17. The phase plot looks like a saw tooth waveform as the phase jumps 360 degree as the frequency increases.

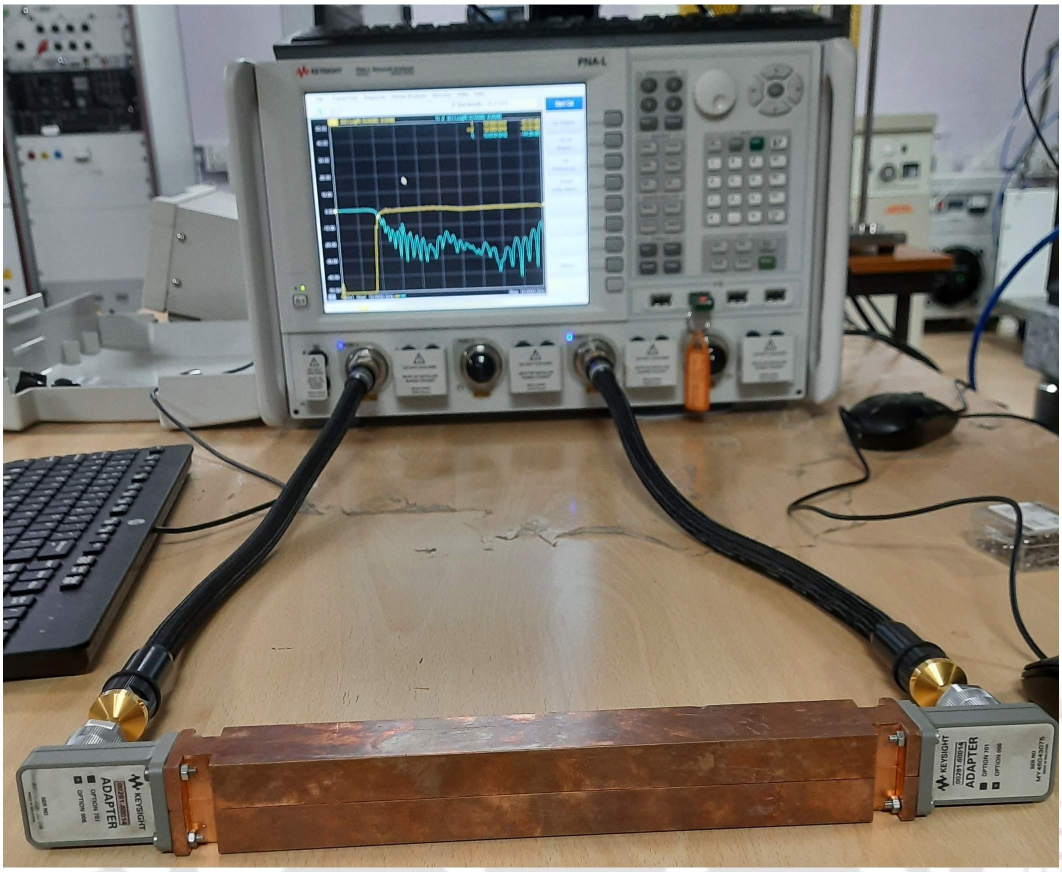

Fig. 4.15: Experimental setup for measuring S-parameters using VNA.

(b) The phase angle information of S21 signal of the waveguide adapters connected back-to-back is obtained which is shown in Fig. 4.18.

(c) The continuous phase function with respect to frequency of measured phase signal is obtained [137] for both the above cases.

(d) The continuous phase plot for the device is obtained by subtracting the phase of the adapters from the phase of DUT-adapters composite. Similar plot is obtained for the same model in CST simulation. The continuous phase for the measured and simulated condition is compared in Fig. 4.19.

(e) The axial wave number versus frequency for the measured and simulated width-modulated SWS is compared in Fig. 4.20.

It is seen that both the plots are in good agreement.

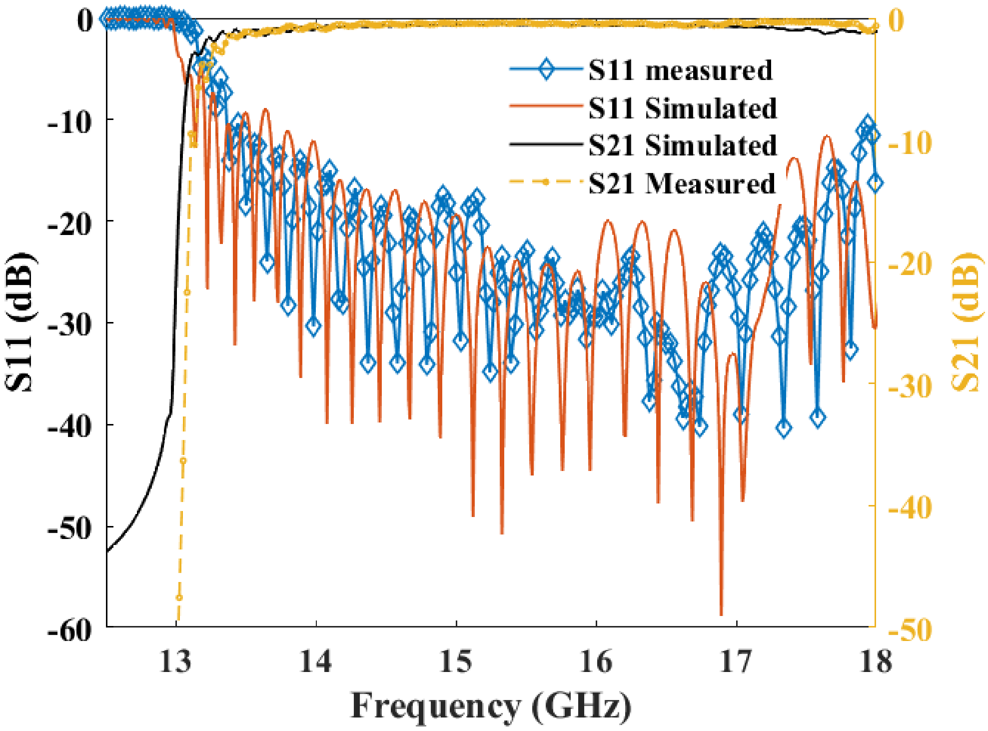

Fig. 4.16: Comparison of simulated and experimental S-parameters.

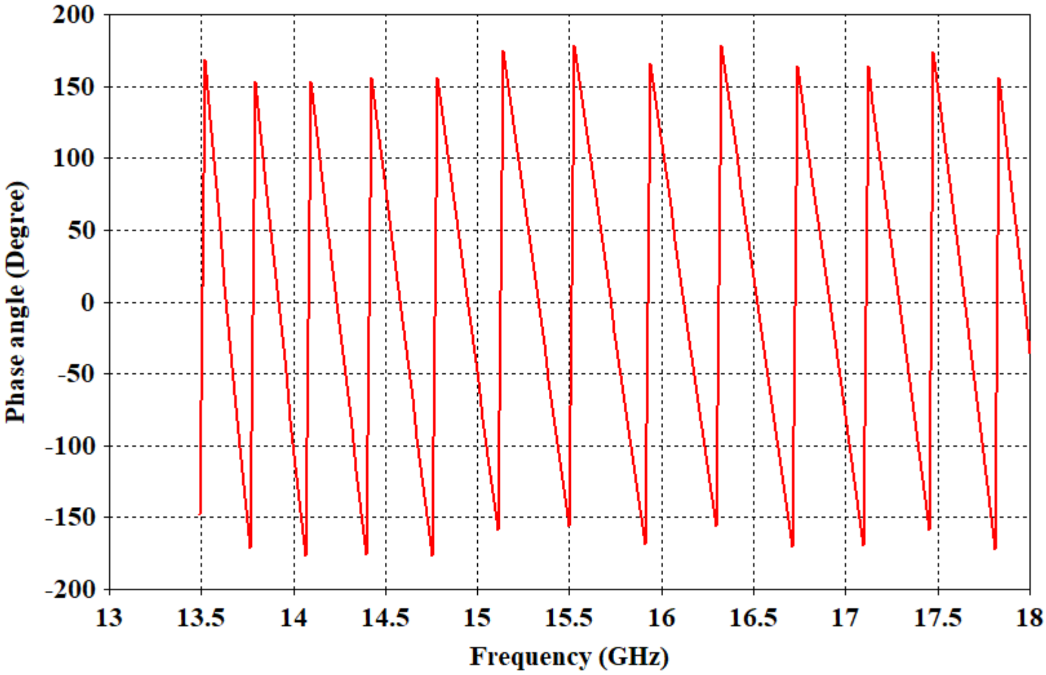

Fig. 4.17: Phase angle of S_{21} signal of the SWG structure along with the coaxial to waveguide adapters.

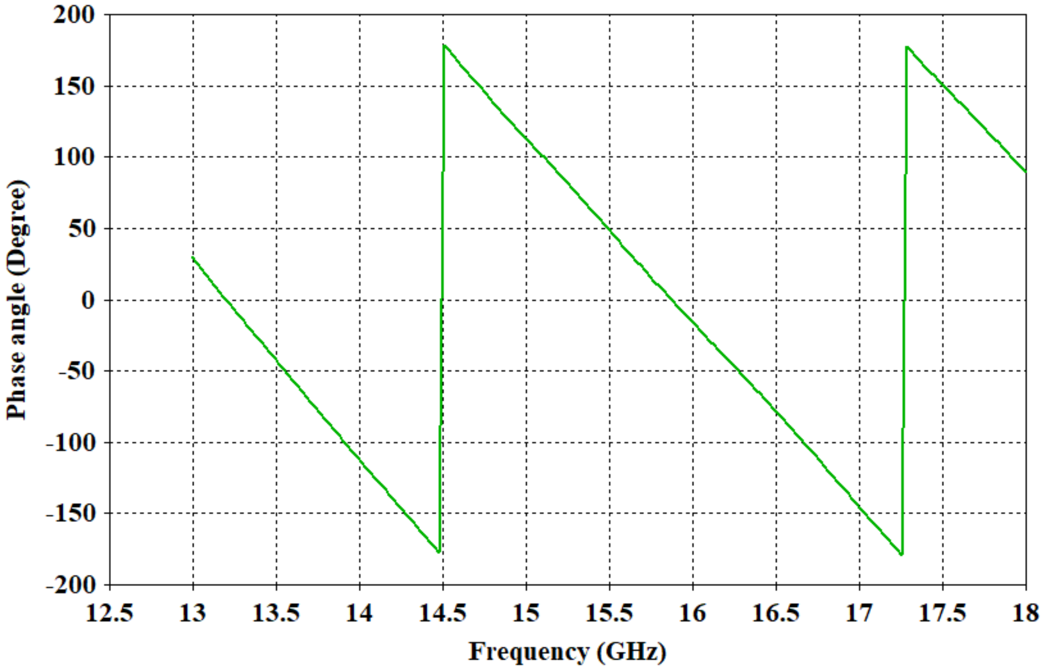

Fig. 4.18: Phase angle of S21 signal of the coaxial to waveguide adapters when connected back-to-back.

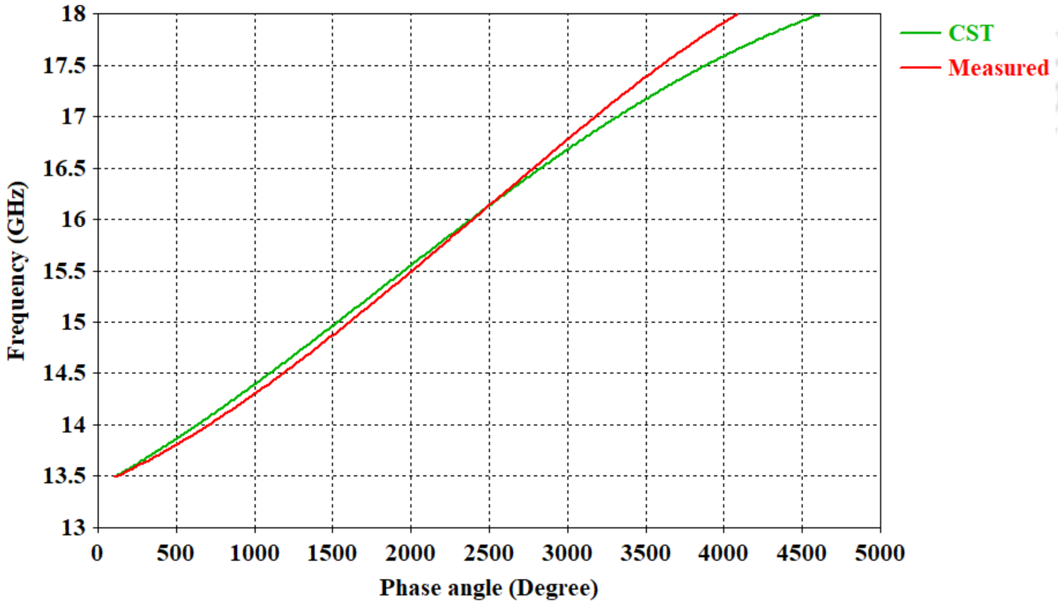

Fig. 4.19: The continuous phase for the DUT with respect to frequency in measured and simulated condition.

4.6 Summary

A G-band width-modulated SWG structure is analyzed for wideband TWT operation. The various cold circuit parameters, such as, dispersion, phase velocity and interaction impedance are evaluated and optimized. Parametric simulations are carried out for varying width-modulation

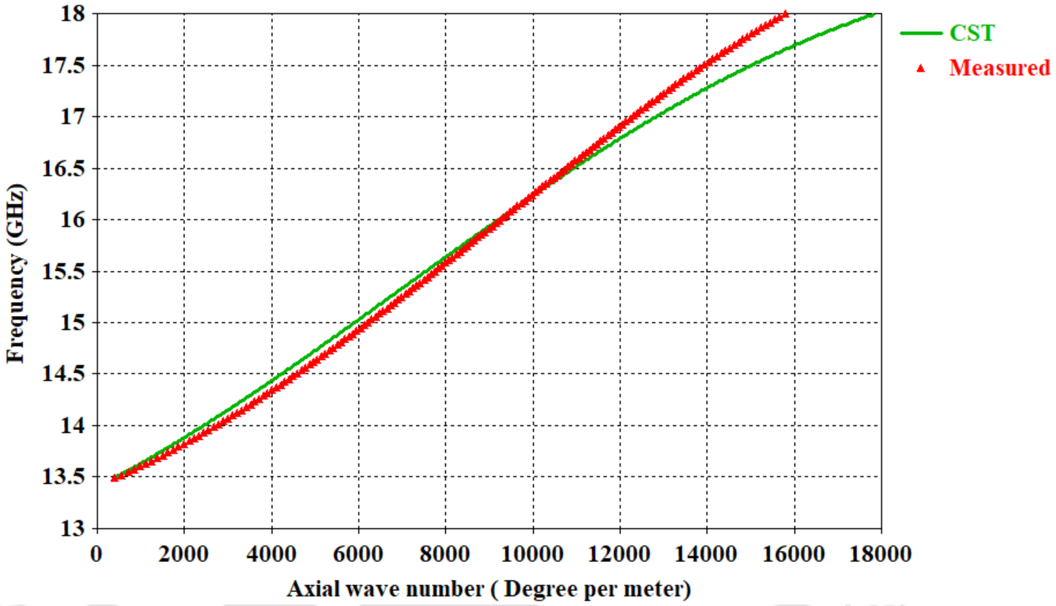

Fig. 4.20: The axial wave number versus frequency for the DUT in measured and simulated condition.

amplitude to achieve a flat dispersion and higher interaction impedance. The width-modulation amplitude of 50 μm is chosen based on above. Transition sections at both ends of the SWS is designed in CST frequency domain solver where the sinusoidal profile is gradually increased for reducing reflection. The simulated structure provides a wideband transmission window. High power behaviour of the device is studied by using Particle-in-Cell simulation in CST. The width-modulated single-section as well as two-section TWT structure are studied. The single-section design provides greater gain and efficiency in comparison to two-section design. However, the single-section design concedes substantial reflection of power at the input port during high power operation. The two-section structure is realized by introducing an intermediate coupling section with attenuator to isolate the input and output sections of the proposed TWT. The two-section design is proved to be useful to minimize back propagation of power during beam on condition. The structure reduces the reflected power level by 98.29% in comparison to single-section structure. The two-section design shows a wideband operation with significant output power of 10 W for 200-246 GHz frequency range. The maximum output power for the single-section and two-section structures are found to be 53.0 W, and 38.5 W, respectively. The corresponding gains are 30.25 dB, and 28.56 dB, respectively at 213 GHz. The half-power bandwidth of the two-section structure is estimated to be 32.5 GHz covering

200-232.5 GHz. The scaled version of the structure is fabricated at Ku-band. The S-parameters of the SWS are measured using VNA. The dispersion curve of the experimental structure is obtained by employing the angle information of the measured S_{21} data. A very good agreement is found between the simulated and experimental S-parameters as well as dispersion results. Simple fabrication, wideband operation and negligible reflection make width-modulated SWG structure a promising TWT candidate in G-band.

5

Design of Truncated SWG for THz TWT

Contents

5.1 Introduction

In chapter 4, a width-modulated SWG structure is studied to obtain a reasonably high output power over a wideband frequency in G-band. The width-modulated structure exhibits higher gain per length than the other reported SWS in the similar band. A cylindrical beam is employed for the TWT. The frequency beyond G-band makes the dimension of the SWS more tiny. Therefore, the fabrication of width-modulated structure for those frequency band becomes more challenging. The truncated SWG structure exhibits lower attenuation [130] in comparison to plain SWG. The truncated or flat roof SWS structure is also easy for fabrication. In this chapter, a wideband truncated SWG structure is analyzed to operate in the frequency range 580-730 GHz. The value of truncation is optimized to satisfy the following needs, (a) to obtain a suitable space for transmission of electron beam which is vital in THz band, (b) to achieve high value of interaction impedance for realizing sufficient gain per period, and (c) to yield a flatter dispersion required for broadband operation.

In THz band, the VEDs require higher beam current to overcome the high attenuation resulting from surface resistance. However, there are limitation in emission current density of the practical emitters [139], [140]. Therefore, the structure is analyzed by using cylindrical beam as well as four numbers of sheet beams with different aspect ratios. The interaction impedance for the beam-tunnel cross section area is obtained for 5 $\mu m \times 5$ μm grid points to understand beam-wave interaction potential at various points of the cross section area, which helps to determine an appropriate shape of the electron beam.

5.2 Cold Test Analysis

The SWS of a TWT is a low Q periodic structure which provides continuous beam-wave interaction to obtain amplification over wide range of frequencies. Therefore, analysing a single period of SWS with periodic boundary condition is sufficient to obtain various cold test parameters of the SWS. The cold test parameters of the truncated SWG SWS is obtained in the eigen mode solver of CST. The various views of the single period of truncated SWGSWS are shown in Fig. 5.1.

The unit section of the structure is shown in Fig. 4.1.

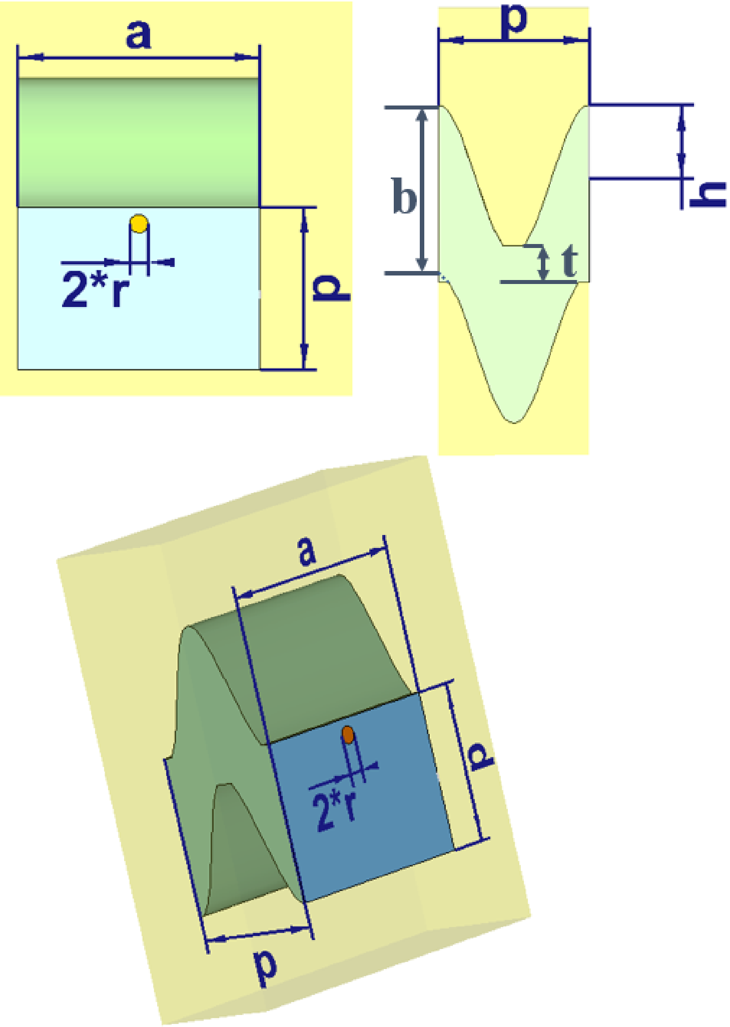

Fig. 5.1: Geometry of the single period SWGSWS, (a) Front view (b) Side view and (c) Isometric view.

The front view of the single period is provided in Fig. 5.1(a) which shows a rectangular cross section ($a \times d$) and the position of cylindrical beam of diameter $2 \times r$. The sinusoidal variation of the SWS with sine-wave amplitude h is shown in Fig. 5.1(b), and the perspective view of the unit length is shown in Fig. 5.1(c). It can be noted that, the width of the rectangular cross section d, shown in Fig. 5.1(a) is greater than the smaller dimension of the rectangular waveguide b due to flat top structure and related by the equation 5.1

$$d = \frac{b+t}{2} + h \tag{5.1}$$

The dimensional parameters of the flat roof SWG structure are provided in Table 5.1.

Table 5.1: Dimensional parameters of the SWS

Parameters	Value (μm)
Broader dimension of waveguide (a)	260
Smaller dimension of waveguide (b)	168
Length of single period (p)	149
Amplitude of sine-wave profile (h)	73
Thickness of beam-tunnel (t)	36
Diameter/thickness of the electron beam ($2 \times r$)	20

The interaction structure of the TWT is shown in Fig. 5.2. There are input and output couplers section which provide gradual sinusoidal undulation for minimizing reflection of RF power.

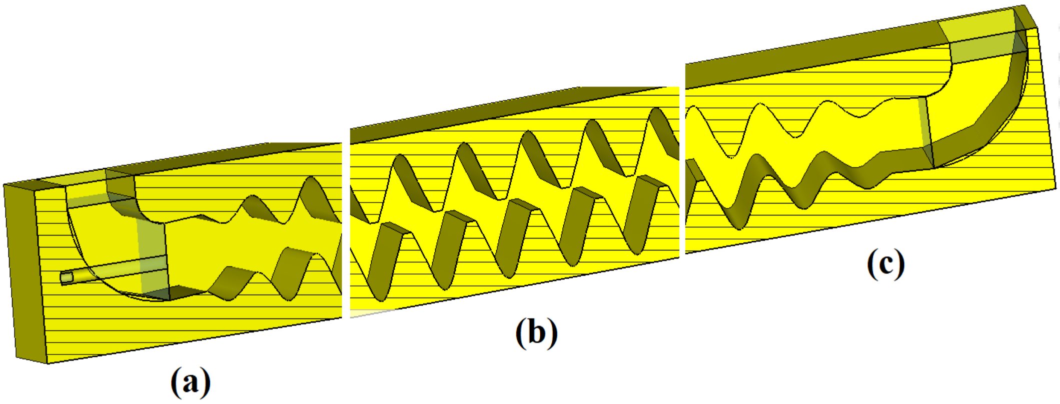

Fig. 5.2: Interaction structure of flat top SWGTWT, (a) Input coupler (b) SWS (c) Output coupler.

The sub-THz TWT works in the region of first spatial harmonic, which implies that the phase shift per period changes from 2π to 3π [106], to keep the beam voltage at a moderate value. Dispersion diagram of the structure for the operating mode along with the beam lines are plotted in Fig. 5.3.

The 18.3 kV beam line remains synchronous with the operating mode for 580-750 GHz frequency. However, in order to have effective amplification, the beam velocity should be higher than the axial phase velocity. Therefore, the optimum beam voltage is determined to be 18.6 kV through PIC simulation, discussed in Section 5.3.

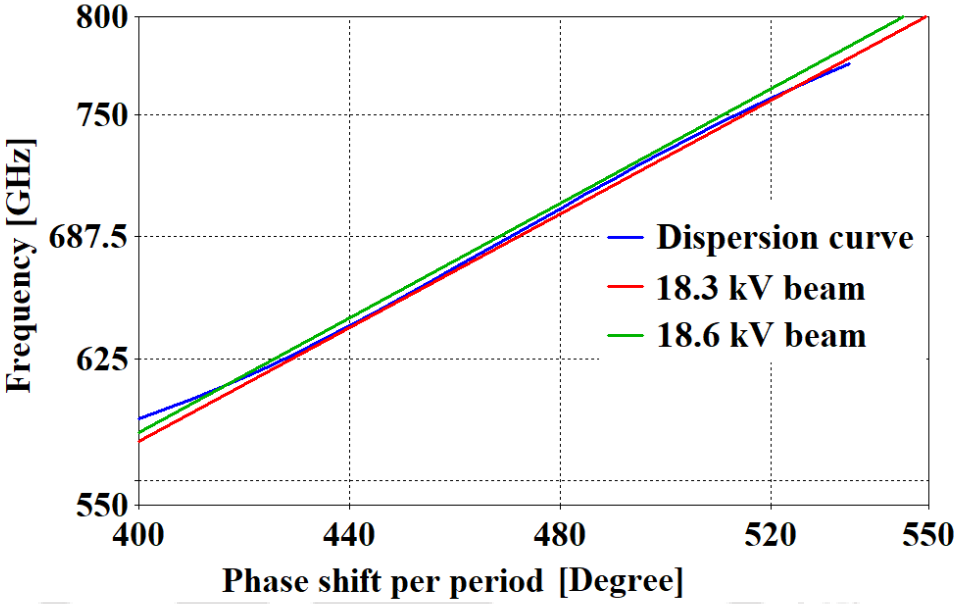

Fig. 5.3: Dispersion diagram of the SWGSWS along with beam lines.

Interaction impedance k_n is a vital cold test parameter which quantify the capability of beam-wave interaction of a SWS. The value of k_n should be sufficiently high to ensure fruitful interaction between electron beam and RF field. The interaction impedance of the of the truncated SWG structure is evaluated by using template based post processing technique in CST which is discussed in 4.2. The on-axis interaction impedance of the structure at 650 GHz is plotted in Fig. 5.4 for various values of t.

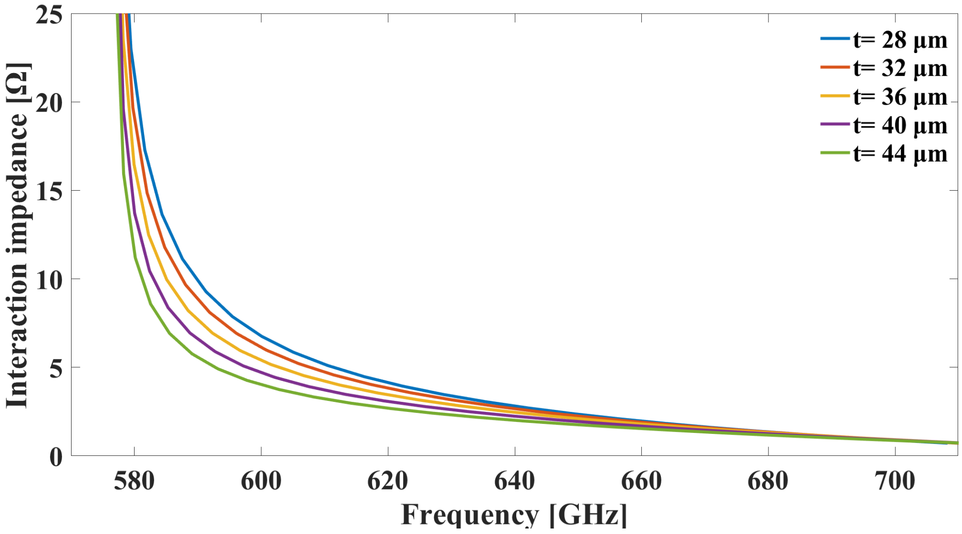

Fig. 5.4: Interaction impedance for various values of truncation of SWGSWS.

It is seen that as the value of t decreases the interaction impedance increases. The narrowing of beam tunnel area causes stronger axial field and hence greater value of interaction impedance and vice versa. However, there should a sufficient beam tunnel area for transportation of electron beam without beam-wall interception. The axial phase velocity of the structure with respect to frequency is plotted in Fig. 5.5 for various values of *t*.

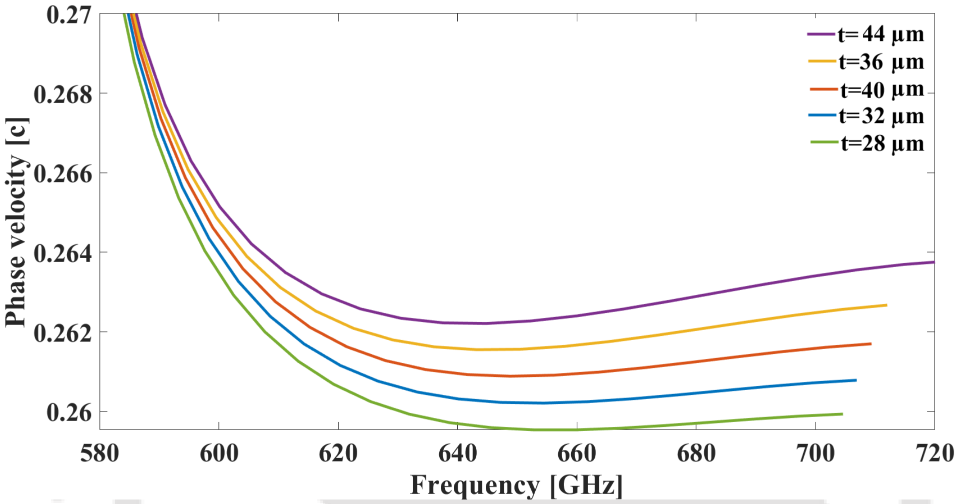

Fig. 5.5: Phase velocities for various values of truncation of SWGSWS.

As the value of *t* decreases the phase velocity is also decreases and vice versa. The reason is that the thinner beam tunnel leads to longer path for RF wave to travel which reduces the axial phase velocity. In view of having suitable space for beam transportation, sufficient interaction impedance and a flat dispersion, the value of *t* is chosen to be 36 μm. The higher value of attenuation demands higher beam current in THz frequencies for realizing desired gain. However, the meagre space available for beam transportation results an impractical value of current density [139], [140]. The application of rectangular or sheet beam is one of the most practical solutions to address the issue [141], [142]. The interaction impedance is not uniform over the beam tunnel area. Therefore, it is important to know the variation of interaction impedance over the beam tunnel cross section area for choosing a suitable shape of electron beam. Therefore, the interaction impedance at various points of the available beam tunnel area is obtained. A cylindrical beam and sheet beams of four different aspect ratios are initially considered for the TWT. The single period SWS, beam tunnel area, positions of cylindrical beam, position of sheet beams- 1,2,3 and 4 are depicted as zone-1,2,4,5,6,7 and 8, respectively and shown in Fig. 5.6

(a). The interaction impedance for 600 GHz, 650 GHz and 700 GHz at $5\mu m \times 5\mu m$ grid points

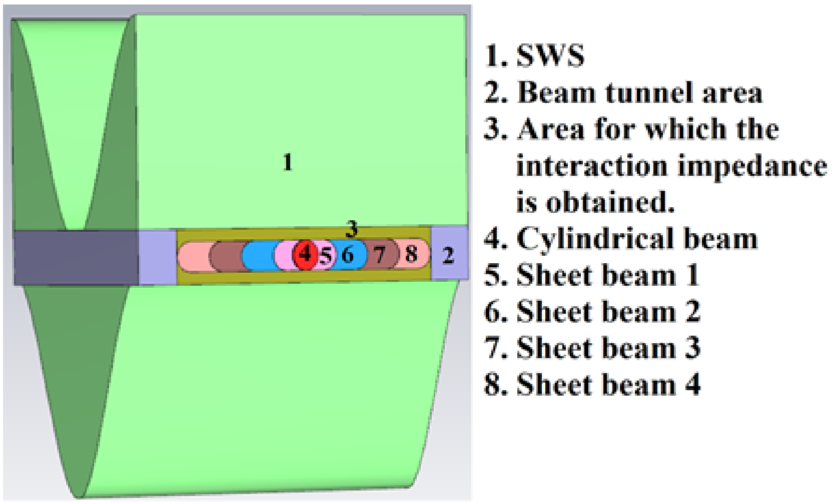

(a) One period of SWS

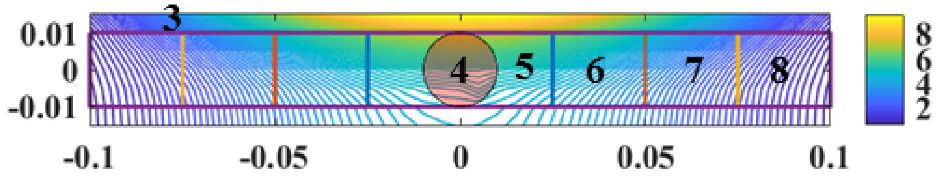

(b) 600 GHz

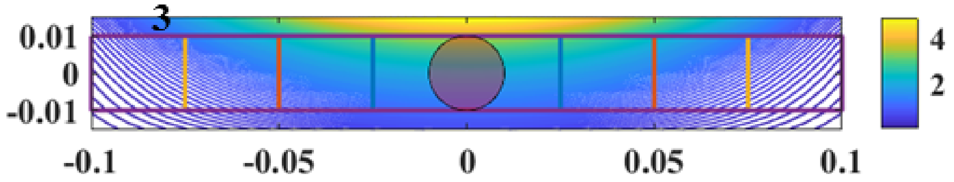

(c) 650 GHz

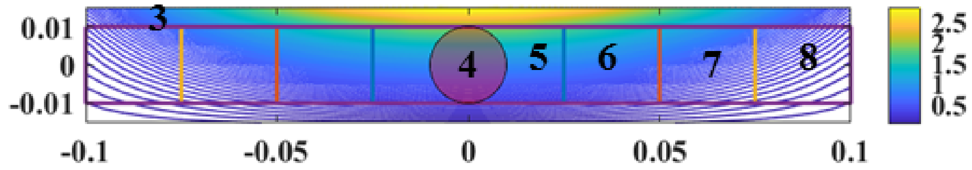

(d) 700 GHz

Fig. 5.6: Interaction impedance at various points in the beam tunnel area (a) Single period SWS showing beam-tunnel area and the positions of electron beams, (b) Interaction impedance of the beam-tunnel area at 600 GHz, (c) at 650 GHz, (d) at 700 GHz.

of the beam-tunnel area (zone 3) are obtained and plotted in Fig. 5.6 (b), Fig. 5.6 (c), and Fig. 5.6 (d), respectively. The interaction impedance is maximum at 600 GHz and minimum at 700 GHz. It is also seen that the interaction impedance is maximum at the central position and reduced gradually towards side walls. The beam-wave interaction with various beams are discussed in Section 5.3.

5.3 PIC Simulation

Hot analysis of the truncated SWG structure is performed using Particle-in-Cell (PIC) solver of CST Particle Studio [25] to estimate various output parameters, such as, output power, bandwidth and gain. At elevated frequencies, the effective electrical conductivity of OFHC copper is less due to non-ideal machine surface and skin effect [134], the electrical conductivity of OFHC copper is considered to be 1×10^7 S/m, whereas the conductivity of OFHC copper σ_{cu} is given by 5.7×10^7 S/m. The PIC simulation is carried out by considering the SWS to be of uniform period p equals to 149 μm. It is very important to determine the number of periods of the SWS to obtain amplification for the entire frequency band of operation. The interaction impedance is gradually decreased from lower to higher frequencies of the frequency band. Therefore, the lower frequency region requires shorter interaction length than the higher frequency region. Hence, four SWS lengths are considered as 126, 133, 136, and 140 periods for each case of PIC simulation. The input parameters for the PIC simulation are provided in Table 5.2

Table 5.2: Input parameters considered in PIC

Parameters	Value
Beam voltage	18.6 kV
Beam current	20 mA
Magnetic field	0.6 Tesla
Input power	20 mW

The input power of 20 mW is considered in simulation which can be provided from a Backward Wave Oscillator (BWO). The output powers estimated for a cylindrical beam is plotted in Fig. 5.7.

In Fig. 5.7, it is seen that the output power at higher frequencies are more for higher number of periods. Higher frequency component requires longer interaction length due to lower interaction impedance. The maximum output power is found to be 4.5 W with cylindrical beam at

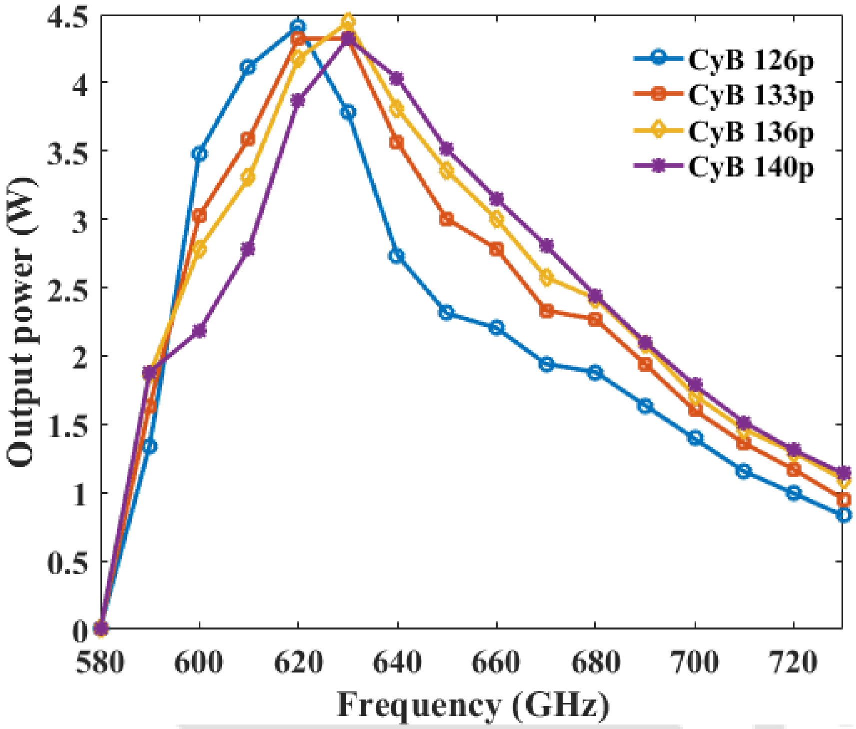

Fig. 5.7: Output power with respect to frequency using cylindrical beam.

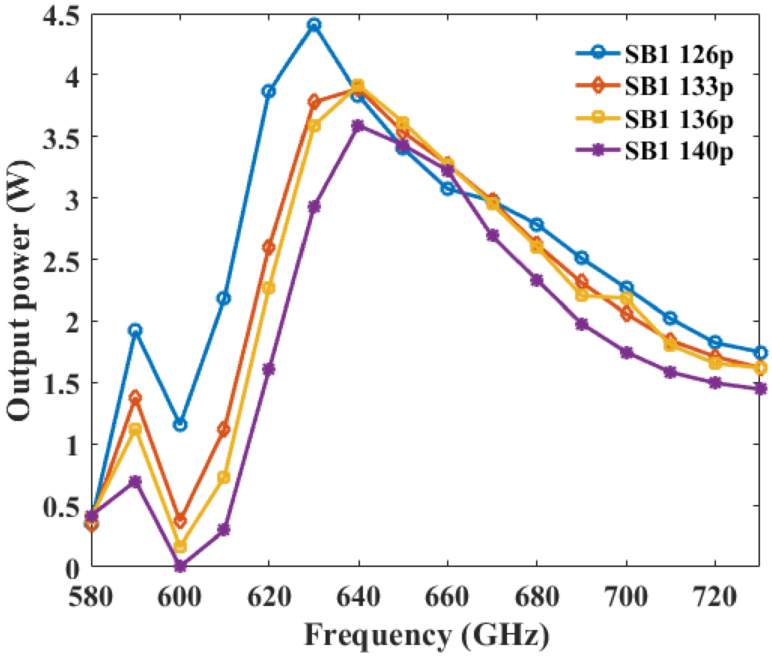

Fig. 5.8: Output power with respect to frequency using sheet beam 1.

620 GHz for SWS length of 126 periods. On the other hand, maximum output power of 4.5 W is obtained at 630 GHz for SWS length of 136 periods.

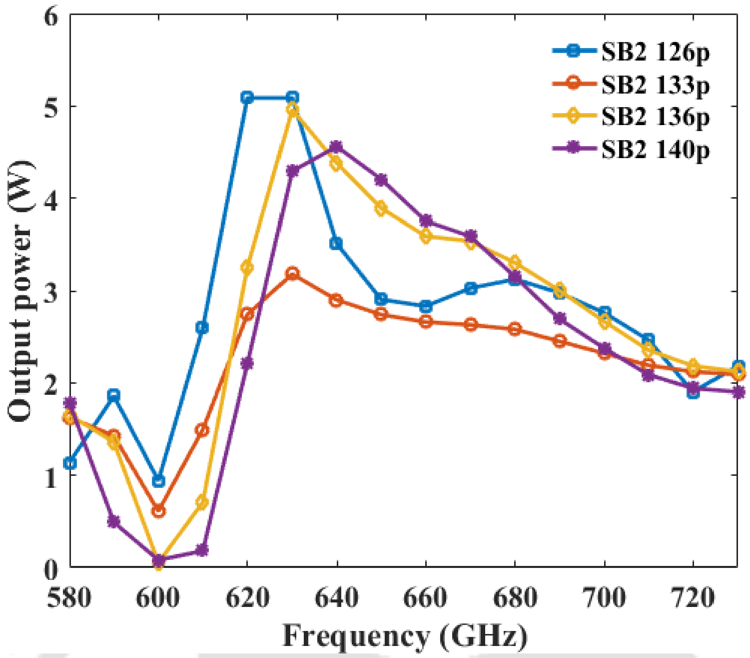

Fig. 5.9: Output power with respect to frequency using sheet beam 2.

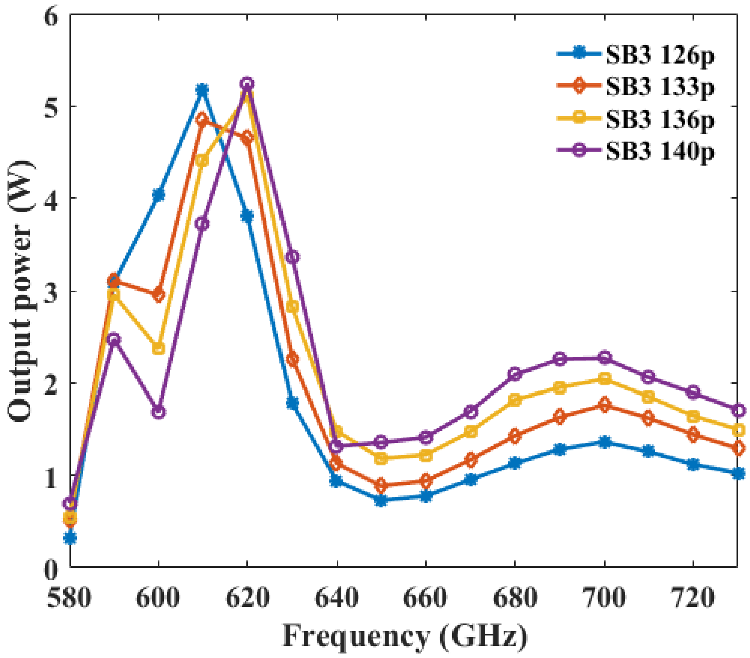

Fig. 5.10: Output power with respect to frequency using sheet beam 3.

At THz frequency, sheet electron beam is preferred over cylindrical beam as the cross-section area of the sheet beam can be made higher by increasing the width of the beam. This satisfies the need of high current density at THz band. Therefore, four different sheet beams namely SB1, SB2, SB3, and SB4 are considered having widths of 50 μm, 100 μm, 150 μm, and

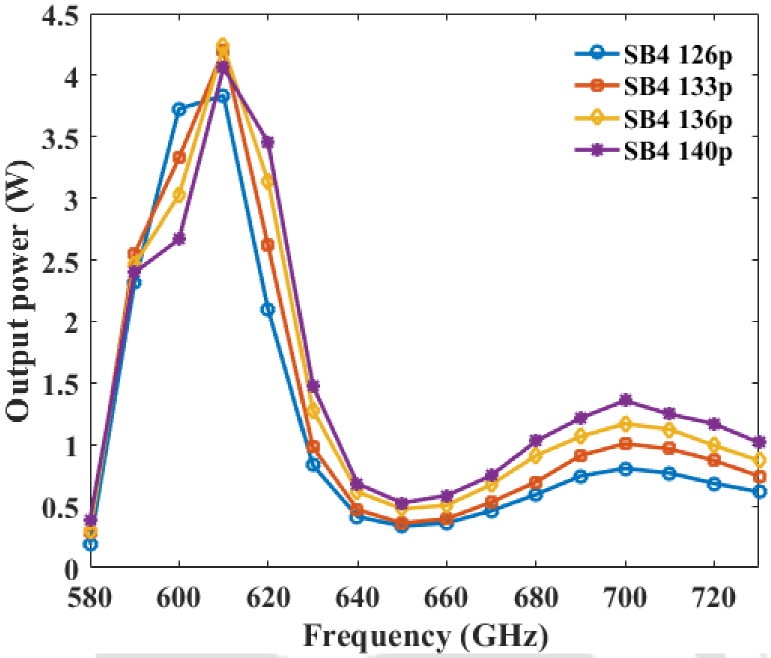

Fig. 5.11: Output power with respect to frequency using sheet beam 4.

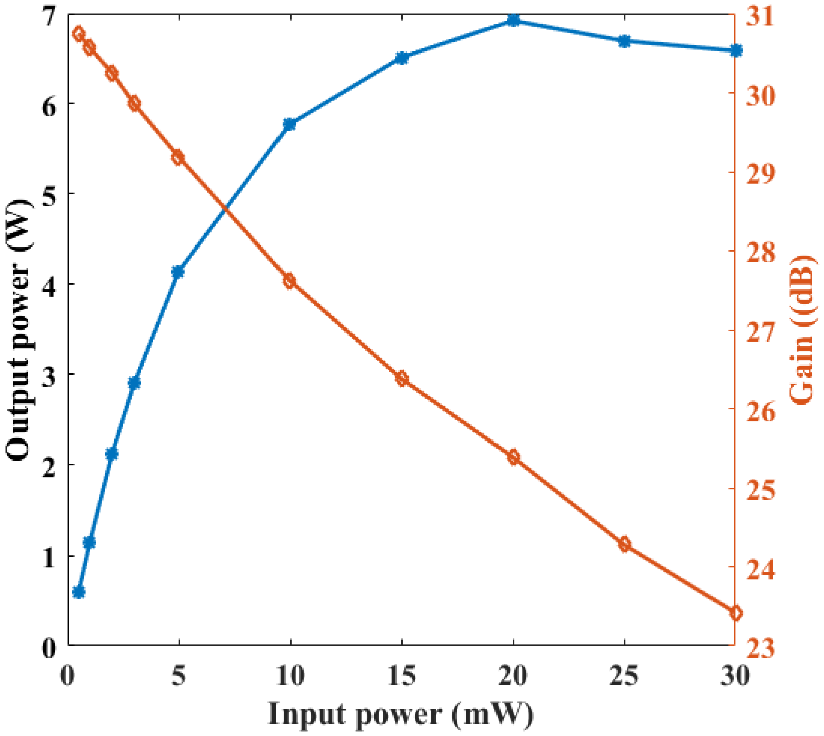

Fig. 5.12: Output power and gain with respect to input power.

200 μm, respectively. However, the thickness of each beam is considered to be 20 μm. The output powers obtained through PIC simulation for the rectangular beams are plotted in Fig.

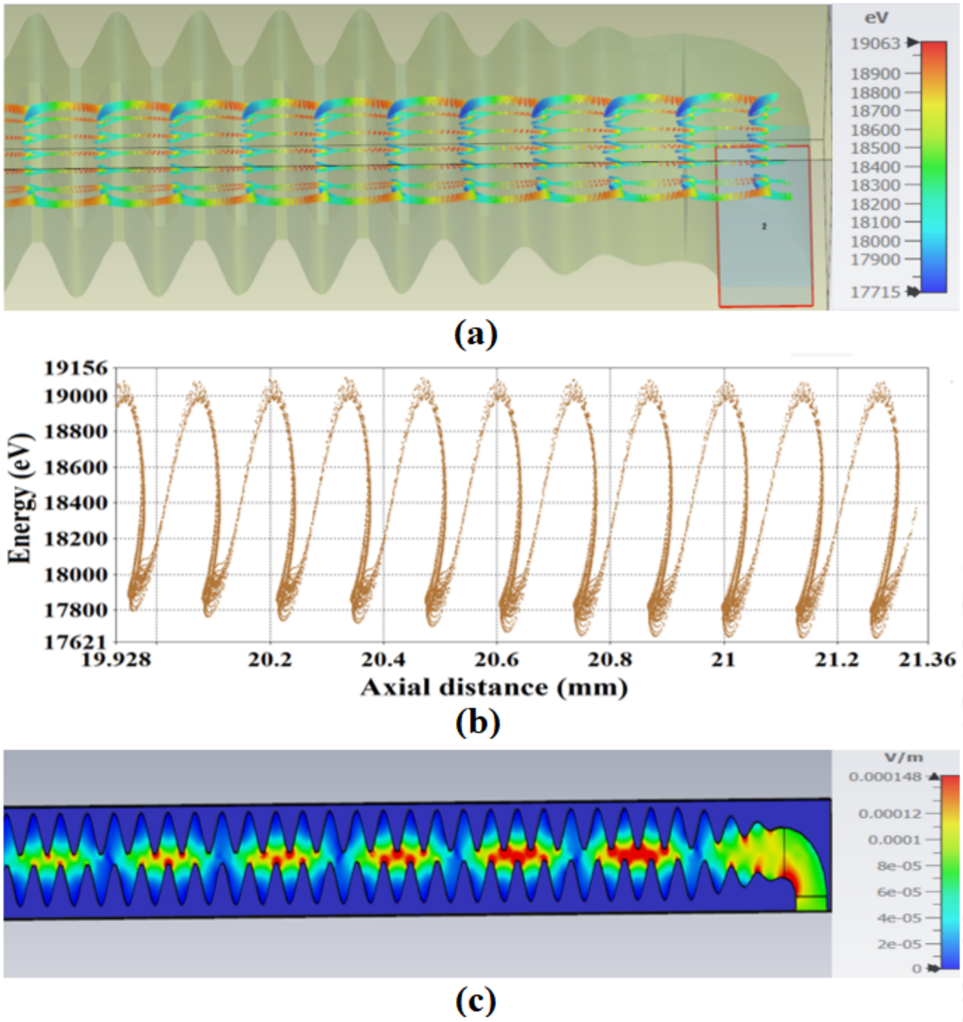

Fig. 5.13: (a) Formation of beam bunch (b) Splitting of energy of the spent electron beam (c) RF field at the final section of the SWG structure.

5.8, Fig. 5.9, Fig. 5.10 and Fig. 5.11, respectively. For all the cases, the output power gradually falls beyond 640 GHz. However, the high frequency components exhibit comparatively greater power output for longer SWS. In Fig. 5.10, and Fig. 5.11, it is seen that the output power is reduced for 630-670 GHz range which is due to the large mismatch of electron beam velocity with RF axial phase velocity. It can be noted in Fig. 5.5, the axial phase velocity is not flat with respective to frequency. The value of phase velocity of the SWS is decreased in the frequency range of 630-670 GHz. However, the effect of lowering of output power is evident in SB3, and SB4 due wide beam widths. The beam experienced wide variety of interaction impedance as observed in Fig. 5.6 unlike the case of SB1, and SB2, where the width of beam cross-section is less. The maximum output power and bandwidth obtained for SB2 using 126 periods is 5.1 W

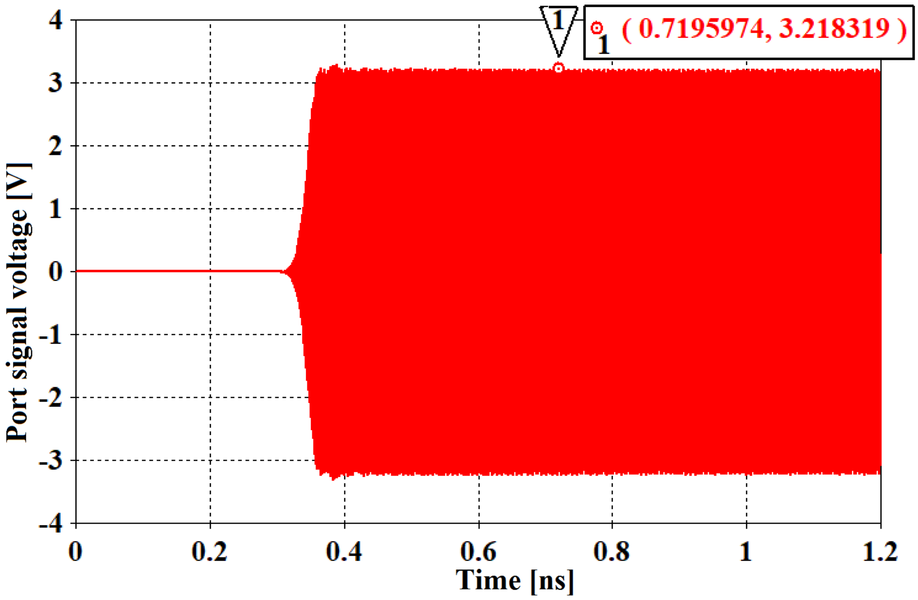

Fig. 5.14: Growth of RF signal

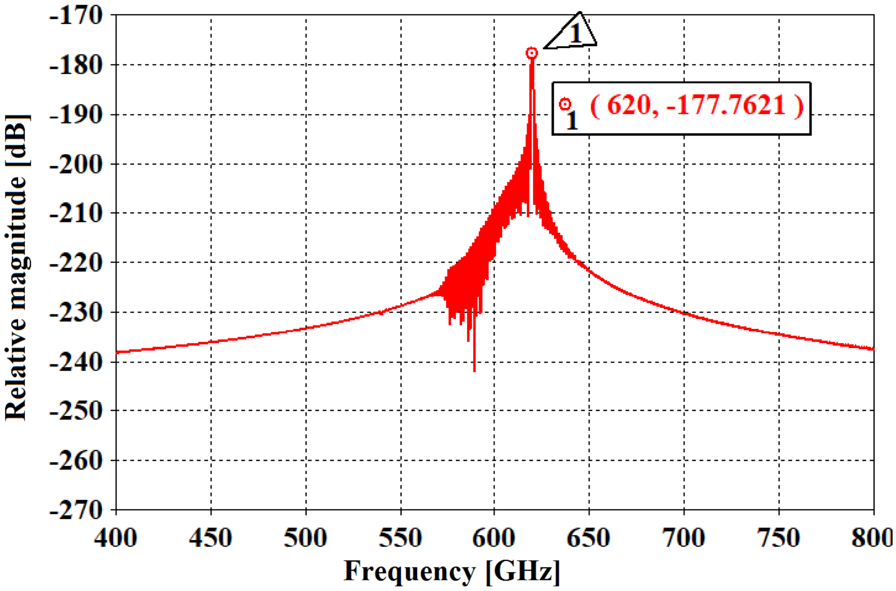

Fig. 5.15: Power spectral density of the output signal

and 105 GHz, respectively.

The formation of beam bunch due to density modulation, the phase space diagram showing the splitting of energy, and the growth of RF field for the final section of the structure are shown in Fig. 5.13. More numbers of electron losses their energy than the electrons which gain, that causes net energy transfer and growth of RF field of the device. The growth of time signal at the output port of the SWS is shown in Fig. 5.14. After the transit time of the electron beam the output signal starts growing. The power spectrum density (PSD) of the output signal is plotted in Fig. 5.15. The spectrum shows a single frequency operation for the input tone signal.

5.4 Summary

A truncated SWG structure is studied to produce wideband TWT operation in the frequency around 600 GHz. The various cold circuit parameters, such as, dispersion diagram, phase velocity and interaction impedance are evaluated and optimized through the parametric simulations. A flat dispersion, coupled with greater value of interaction impedance is achieved. The PIC simulation is carried out to demonstrate high power operation of the device. Cylindrical beam as well as sheet beam of various widths are considered in PIC simulation. The maximum output power is achieved to be 5.1 W at 620 GHz using SB2 with 126 period SWS. The 3-dB bandwidth is estimated to be nearly 16.9% amounting 105 GHz. A significant output power of 2 W is achieved for 605-730 GHz frequency band using the same SWS. Wideband operation, reasonably higher power, gain and efficiency make truncated SWGTWT a promising TWT candidate in THz frequencies.

6

Conclusions and Future Work

Contents

6.1 Thesis Conclusions

In this thesis, three different interaction structures are studied and optimized to obtain performance enhancement over the reported analogous interaction structure operating in similar frequency band. The interaction structures include a gyrotron cavity operating in Ka-band and two different sine waveguide based slow wave structures for travelling wave tubes operating in THz band.

The beam generation and guidance system of a 20 kW CW gyrotron is designed for operating at 28 GHz in TE_{02} mode. Two triode type magnetron injection guns (MIG) are designed in EGUN. The performance of the MIGs are validated in the 3D simulation using CST particle tracking solver. The critical electron beam parameters are obtained.

The magnetic focusing system of of the gyrotron is designed in EGUN. There are 7 magnets in the design which are placed at gun, cavity and collector region. A three-staged depressed collector is designed by means of 3D electro-magneto static analysis in CST particle tracking studio for enhancement of efficiency of the gyrotron. In CST particle tracking simulation it is demonstrated that the highest energy electrons are collected at highest depressing potential and vice versa. The depressed collector contributes to enhance the overall efficiency from 50 % to 67%. It is expected that the higher efficiency of the CW gyrotron if demonstrated experimentally, will be attractive for industrial applications.

The interaction cavity of the Ka-band gyrotron is studied by using single mode time dependent analytical equations as well as PIC simulations. The start oscillation current and coupling coefficient are calculated for determining the operating magnetic field, and beam diameter, respectively. The output power of the gyrotron is calculated by employing single mode time dependent approach. The beam-wave interaction of the gyrotron is also studied by using 3D particle-in-cell solver in CST. The gyrotron is operated at below per magnetic field to push the operating point towards the hard excitation region. The higher value of velocity ratio is considered to have more transverse energy of electrons. The combined effect of lower magnetic field and higher velocity ratio prove to be useful to realize high electronic efficiency. However, the operation with lower magnetic field value leads to prolong undesired mode competitions between the operating and neighbouring mode. Hence, axially directed slots in the cavity wall are introduced to disturb the wall current of the competing mode. The depth, width and numbers of the slot are optimized through parametric simulations. The duration of mode competition is eliminated by 50% without sacrificing the output power by using properly engineered slots. The output power of the gyrotron is estimated to be 20 kW at 27.885 GHz. The effect of velocity spread on the output power is studied.

A width-modulated two-section sine waveguide structure is studied to obtain wideband TWT operation in G-band. The various cold circuit parameters, such as, dispersion diagram, phase velocity and interaction impedance are evaluated in CST. A flat dispersion is achieved by keeping the value of interaction impedance reasonably high. The transition sections of the slow wave structure is designed to realize smooth transmission of RF power through the SWS. The high power operation of the device is studied through PIC simulation. The single section width modulated SWG structure exhibits higher gain per unit length. However, the two-section design proves to be effective in eliminating the reflected power during hot condition. The maximum output power and saturated gain are estimated to be 39 W and 28.9 dB, respectively at 215 GHz whereas, the half-power bandwidth is estimated to be 32.5 GHz. The scaled version of the width-modulated SWS is fabricated and characterised at Ku-band. The S-parameters and dispersion of the structure are measured and compared with simulated results.

A truncated SWG structure is studied for producing wideband TWT operation in the frequency range 580-730 GHz. The cold test parameters, such as, dispersion diagram, phase velocity and interaction impedance are evaluated and optimized in CST. The interaction impedance at different points in the beam tunnel area is obtained and plotted to study the beam-wave interaction potential of the structure for electron beams of various shape. The high power behaviour of the structure is studied in presence of cylindrical as well as sheet beams of various aspect ratios. The simple truncated SWG structure delivers more than 2 W power for 100 GHz frequency ranging from 600-700 GHz. The truncated SWG structure is found to be a promising TWT candidate in THz band due to simple fabrication, wideband operation and reasonably high output power.

6.2 Future work

This thesis focusses on the study and design of advanced interaction structures for mm wave and THz vacuum electron devices. However, there are ample scope of extending the current work. The possible areas in which future works can be taken up are summarised below:

(i) Efficiency enhancement of a Ka-band medium power gyrotron is discussed in the thesis. The mode competition between the operating and neighbouring mode is eliminated using slotted cavity. The output power is estimated by using single mode analytical equations as well as by means of PIC simulation. The MIG and depressed collector of the gyrotron are designed using particle tracking simulation in CST. Therefore, future work can be taken up for experimental demonstration of gyrotron operation.

(ii) The width-modulated SWS structure is studied and analyzed in G-band for TWT operation using simulation. The scaled version of the width-modulated structure is fabricated and experimentally characterized in Ku-band. The fabrication and experimental characterization work of the actual structure in G-band can be taken up in future studies.

(iii) A truncated SWG structure is studied and designed to obtain TWT operation in 590-730 GHz frequencies. Both cold test and hot test parameters of the structure are estimated in simulation. As an extension of the current work, the other subsystem of the TWT, such as, electron gun, cavity, magnetic focussing system, and dielectric window can be designed and analyzed.

Bibliography

[1] B. N. Basu and S. K. Datta, " Microwave tubes and applications", *Journal of Electromagnetic Waves and Applications*, 31:17, 1771-1774, 2017, DOI: 10.1080/09205071.2017.1375646

[2] V. Srivastava, "Microwave tubes: A necessity for high power applications," *Proceedings of International Conference on Recent Advances in Microwave Theory and Applications*, pp. 183-184, 2008, doi: 10.1109/AMTA.2008.4763263.

[3] S. Gold and G. Nusinovich, "Review of high-power microwave source research," *Review of Scientific Instruments*, vol. 68, no. 11, pp. 3945–3974, 1997, https://doi.org/10.1063/1.1148382

[4] H. Minamide, "Development of high-Power Terahertz-wave sources for finding novel applications," *IEEE Transactions on Terahertz Science and Technology*, vol. 5, no. 6, pp. 1104-1109, Nov. 2015

[5] Graeme L. Stephens et al, "A new dimension of space-based observation of clouds and precipitation," NASA Goddard Inst. Space Stud., New York, NY, USA, Tech. Rep. REPT-02-02, 2001, https://doi.org/10.1175/BAMS-83-12-1771

[6] S. Rangan, T. S. Rappaport and E. Erkip, "Millimeter-wave cellular wireless networks: potentials and challenges," *Proceedings of the IEEE*, vol. 102, no. 3, pp. 366-385, March 2014, doi: 10.1109/JPROC.2014.2299397.

[7] E. A. Nanni, A. B. Barnes, R. G. Griffin and R. J. Temkin, "THz dynamic nuclear polarization NMR," *IEEE Transactions on Terahertz Science and Technology*, vol. 1, no. 1, pp. 145-163, Sept. 2011, doi: 10.1109/TTHZ.2011.2159546.

[8] G. L. Stephens et al., "The cloudsat mission and the EOS constellation: A new dimension of space-based observation of clouds and precipitation," NASA Goddard Inst. Space Stud., New York, NY, USA, Tech. Rep. REPT-02-02, 2001, https://doi.org/10.1175/BAMS-83-12-1771.

[9] M. Thumm, "Recent applications of millimeter and submillimeter wave gyrotrons," *25th International Conference on Infrared and Millimeter Waves (Cat. No.00EX442)*, 2000, pp. 99-102, doi: 10.1109/ICIMW.2000.892953.

[10] M. Thumm, "Recent advances in the worldwide fusion gyrotron development," *IEEE Transactions on Plasma Science*, vol. 42, no. 3, pp. 590-599, March 2014, doi: 10.1109/TPS.2013.2284026.

[11] G. Link, L. Feher, M. Thumm, H. . -J. Ritzhaupt-Kleissl, R. Bohme and A. Weisenburger, "Sintering of advanced ceramics using a 30-GHz, 10-kW, CW industrial gyrotron," *IEEE Transactions on Plasma Science*, vol. 27, no. 2, pp. 547-554, April 1999, doi: 10.1109/27.772284.

[12] A. W. Fliflet et al., "A study of millimeter-wave sintering of fine-grained alumina compacts," *IEEE Transactions on Plasma Science*, vol. 28, no. 3, pp. 924-935, June 2000, doi: 10.1109/27.887755.

[13] S. Miyake, "Millimeter-wave materials processing in Japan by high-power gyrotron," *IEEE Transactions on Plasma Science*, vol. 31, no. 5, pp. 1010-1015, Oct. 2003, doi: 10.1109/TPS.2003.818401.

[14] S. Takayama, G. Link, M. Sato and J. Jelonnek, "Possibility for iron production using high-Power millimeter waves," *IEEE Transactions on Plasma Science*, vol. 43, no. 10, pp. 3517-3521, Oct. 2015, doi: 10.1109/TPS.2015.2420682.

[15] Azam S, Wahab Q. "Advanced microwave and millimeter wave technologies: semiconductor devices, circuits and systems." Vukovar: InTech. DOI:10.5772/8749.

[16] Nicol EF, Mangus BJ, Grebliunas JR, et al. "TWTA versus SSPA: a comparison update of the Boeing satellite fleet on-orbit reliability." IVEC-2013, Paris.

[17] Gilmour AS Jr. "Principles of traveling wave tubes." Norwood, Artech House, 1994.

[18] Gilmour AS Jr. "Klystrons, traveling wave tubes, magnetrons, crossed-field amplifiers, and gyrotrons." Boston (MA), Artech House, 2011.

[19] V. A. Flyagin, A. V. Gaponov, M. I. Petelin, and V. K. Yulpatov, “The gyrotron,” *IEEE Trans. Microw. Theory Techn.*, vol. MTT-25, no. 6, pp. 514–521, Jun. 1977.

[20] M. V. Kartikeyan, E. Borie, and M. Thumm, Gyrotrons: high-power microwave and millimeter wave technology. Springer Science Business Media, 2013.

[21] V. L. Granatstein, B. Levush, B. G. Danly, and R. K. Parker, “A quarter century of gyrotron research and development,” *IEEE Transactions on Plasma Science*, vol. 25, no. 6, pp. 1322–1335, Dec 1997.

[22] M. Sumathy, K. J. Vinoy and S. K. Datta, "Analysis of ridge-loaded folded-waveguide slow-wave structures for broadband traveling wave tubes," *IEEE Transactions on Electron Devices*, vol. 57, no. 6, pp. 1440-1446, June 2010, doi: 10.1109/TED.2010.2045680.

[23] C. Paoloni and M. Mineo, "Double corrugated waveguide for G-band traveling wave tubes," *IEEE Transactions on Electron Devices*, vol. 61, no. 12, pp. 4259-4263, Dec. 2014, doi: 10.1109/TED.2014.2364636.

[24] X. Xu et al., "Recent advancements in sine waveguide for terahertz vacuum electron devices," *International Conference on Microwave and Millimeter Wave Technology (ICMMT)*, pp. 1-3, 2012, doi: 10.1109/ICMMT.2012.6229964.

[25] CST AG, Germany, CST Studio suite, https://www.cst.com.

[26] ANSYS HFSS, USA, https://www.ansys.com.

[27] Northrop Grumman, USA, MAGIC 3D, https://www.northropgrumman.com/space/magic-tool-suite/.

[28] Frank Gustrau, "RF and microwave engineering: fundamentals of wireless communications", WILEY.

[29] Claudio Paoloni, Diana Gamzina, Rosa Letizia, Yuan Zheng Neville C. Luhmann Jr. (2021) "Millimeter wave traveling wave tubes for the 21^{st} Century", *Journal of Electromagnetic Waves and Applications*, 35:5, 567-603, DOI: 10.1080/09205071.2020.1848643

[30] Gamzina D, Himes LG, Barchfeld R, et al, "Nano-CNC machining of sub-THz vacuum electron devices", *IEEE Trans Electron Devices*, 2016;63(10):4067–4073, DOI:10.1109/TED.2016.2594027

[31] Baig A, Gamzina D, Kimura T, et al, "Performance of a nano-CNC machined 220-GHz traveling wave tube amplifier" *IEEE Trans Electron Devices.* 2017;64(5):2390–2397.

[32] André F, Racamier J-C, Zimmermann R, et al. "Technology, assembly, and test of a W band traveling wave tube for new 5G high-capacity networks.", *IEEE Trans Electron Devices*, 2020;67(7):2919–2924. DOI:10.1109/TED.2020.2993243

[33] Elmer JW, Klingmann J, Van Bibber K. "Diffusion bonding and brazing of high purity copper for linear collider accelerator structures.", *Phys Rev ST Accel Beams.* 2001;4:053502.

[34] Paoloni C, Di Carlo A, Bouamrane F, et al. "Design and realization aspects of 1-THz cascade backward wave amplifier based on double corrugated waveguide, *IEEE Trans Electron Devices.* 2013;60(3):1236–1243.

[35] C. Ruan, S. Wang, Y. Han, Q. Li and X. Yang, "Theoretical and experimental investigation on intense sheet electron beam transport with Its diocotron instability in a uniform magnetic field," *IEEE Transactions on Electron Devices,* vol. 61, no. 6, pp. 1643-1650, June 2014, doi: 10.1109/TED.2014.2299286.

[36] K. T. Nguyen, J. A. Pasour, T. M. Antonsen, P. B. Larsen, J. J. Petillo and B. Levush, "Intense sheet electron beam transport in a uniform solenoidal magnetic field," *IEEE Transactions on Electron Devices,* vol. 56, no. 5, pp. 744-752, May 2009, doi: 10.1109/TED.2009.2015420.

[37] Elizabeth J. Kowalski, Michael A. Shapiro, and Richard J. Temkin, "An overmoded W-band coupled-cavity TWT", *IEEE Transactions On Electron Devices*, Vol. 62, No. 5, May 2015, pp. 1609-1616

[38] B. K. Shukla et al., "42-GHz 0.5-MW ECRH system for tokamaks SST-1 and aditya," *IEEE Transactions on Plasma Science*, vol. 40, no. 4, pp. 1234–1238, Apr. 2012.

[39] P. C. Kalaria, M. V. Kartikeyan, and M. Thumm, "Design of 170 GHz, 1.5-MW conventional cavity gyrotron for plasma heating," *IEEE Transactions on Plasma Science*, vol. 42, no. 6, pp. 1522–1528, Jun. 2014.

[40] V. Erckmann et al., "ECRH and ECCD with high power gyrotrons at the stellarators W7-AS and W7-X," *IEEE Transactions on Plasma Science*, vol. 27, no. 2, pp. 538–546, Apr. 1999.

[41] M. K. Hornstein, V. S. Bajaj, R. G. Griffin, and R. J. Temkin, "Efficient low-voltage operation of a CW gyrotron oscillator at 233 GHz," *IEEE Transactions on Plasma Science*, vol. 35, no. 1, pp. 27–30, Feb. 2007.

[42] A. C. Torrezan, M. A. Shapiro, J. R. Sirigiri, R. J. Temkin, and R. G. Griffin, "Operation of a continuously frequency-tunable second harmonic CW 330-GHz gyrotron for dynamic nuclear polarization," *IEEE Transactions on Electron Devices*, vol. 58, no. 8, pp. 2777-2783, Aug. 2011, doi: 10.1109/TED.2011.2148721.

[43] S. T. Han, W. J. Lee, K. S. Park, S. W. Choi, J. H. Yoon and J. S. Yoo, "Application of T-ray gyrotron developed for real-time non-destructive inspection to enhanced regeneration of cells," *2015 40th International Conference on Infrared, Millimeter, and Terahertz waves (IRMMW-THz)*, 2015, pp. 1-2, doi: 10.1109/IRMMW-THz.2015.7327867.

[44] T. Idehara and S. P. Sabchevski, "Development and application of gyrotrons at FIR UF," *IEEE Transactions on Plasma Science*, vol. 46, no. 7, pp. 2452-2459, July 2018, doi: 10.1109/TPS.2017.2775678.

[45] M. Y. Glyavin, A. G. Luchinin, M. V. Morozkin, A. S. Sedov, and G. S. Nusinovich, “Development of THz-range gyrotrons for detection of concealed radioactive materials,” *Proc. 21st Int. Crimean Conf. Microw. Telecommun. Technol.*, Sep. 2011, pp. 325–326.

[46] V. Granatstein et al., “Remote detection of radioactive materials using a near-terahertz gyrotron,” *Proc. Abstr. IEEE Int. Conf. Plasma Sci.*, Jul. 2012. p. 5.

[47] U. Singh, A. Bera, N. Kumar, L. P. Purohit and A. K. Sinha, "Three-dimensional simulation of MIG for 42-GHz 200-kW gyrotron," *IEEE Transactions on Plasma Science*, vol. 38, no. 7, pp. 1546-1550, July 2010, doi: 10.1109/TPS.2010.2049748.

[48] W. Jiang, Y. Luo and R. Yan, "Computational design and optimization of a magnetron injection gun," *IEEE Transactions on Electron Devices*, vol. 61, no. 7, pp. 2547-2551, July 2014, doi: 10.1109/TED.2014.2322975.

[49] S. Yuvaraj, D. A. Jose, M. S. Chauhan, M. V. Kartikeyan, S. Illy and M. K. Thumm, "Design studies of a magnetron injection gun for a 2MW, multi-frequency (220/251.5/283 GHz) triangular corrugated coaxial cavity gyrotron," *2018 IEEE International Vacuum Electronics Conference (IVEC)*, 2018, pp. 307-308, doi: 10.1109/IVEC.2018.8391653.

[50] J. Yu, T. M. Antonsen and G. S. Nusinovich, "Effects of beam velocity spread on the excitation of backward waves in beam tunnels of high-power gyrotrons," *2010 Abstracts IEEE International Conference on Plasma Science*, 2010, pp. 1-1, doi: 10.1109/PLASMA.2010.5534353.

[51] G. P. Latsas, Z. C. Ioannidis and I. G. Tigelis, "Dependence of parasitic modes on geometry and attenuation in gyrotron beam tunnels," *IEEE Transactions on Plasma Science*, vol. 40, no. 6, pp. 1538-1544, June 2012, doi: 10.1109/TPS.2012.2192294.

[52] I. G. Chelis, K. A. Avramidis, Z. C. Ioannidis and I. G. Tigelis, "Improved suppression of parasitic oscillations in gyrotron beam tunnels by proper selection of the lossy ceramic material," *IEEE Transactions on Electron Devices*, vol. 65, no. 6, pp. 2301-2307, June 2018, doi: 10.1109/TED.2017.2784198.

[53] P. C. Kalaria, M. V. Kartikeyan and M. Thumm, "Design of 170 GHz, 1.5-MW conventional cavity gyrotron for plasma heating," *IEEE Transactions on Plasma Science*, vol. 42, no. 6, pp. 1522-1528, June 2014, doi: 10.1109/TPS.2014.2305251.

[54] S. Karmakar, R. Sudhakar, J. C. Mudiganti, R. Seshadri and M. V. Kartikeyan, "Electrical and thermal design of a *W* -band gyrotron interaction cavity," *IEEE Transactions on Plasma Science*, vol. 47, no. 7, pp. 3155-3159, July 2019, doi: 10.1109/TPS.2019.2918138.

[55] C. T. Iatrou et al., "Design and experimental operation of a 165-GHz, 1.5-MW, coaxial-cavity gyrotron with axial RF output," *IEEE Transactions on Plasma Science*, vol. 25, no. 3, pp. 470-479, June 1997, doi: 10.1109/27.597262.

[56] W. Wang, D. Liu, S. Qiao and S. Liu, "Study on the terahertz denisov quasi-optical mode convertor," *IEEE Transactions on Plasma Science*, vol. 42, no. 2, pp. 346-349, Feb. 2014, doi: 10.1109/TPS.2013.2294335.

[57] D. Liu, W. Wang, Q. Zhuang and Y. Yan, "Theoretical and experimental investigations on the quasi-optical mode converter for a pulsed terahertz gyrotron," *IEEE Electron Device Letters*, vol. 36, no. 2, pp. 195-197, Feb. 2015, doi: 10.1109/LED.2014.2385872.

[58] G. Ling, B. Piosczyk and M. K. Thumm, "A new approach for a multi-stage depressed collector for gyrotrons," *IEEE Transactions on Plasma Science*, vol. 28, no. 3, pp. 606-613, June 2000, doi: 10.1109/27.887683.

[59] B. Liu, C. Jiao, Y. Zhang, G. Yuan, W. Guo and L. Zheng, "Experimental study of a Ku-band gyrotron backward-wave oscillator with a single stage depressed collector," *IEEE Transactions on Plasma Science*, vol. 35, no. 4, pp. 1065-1069, Aug. 2007, doi: 10.1109/TPS.2007.902123.

[60] I. G. Pagonakis et al., "Numerical investigation on spent beam deceleration schemes for depressed collector of a high-power gyrotron," *IEEE Transactions on Electron Devices*, vol. 65, no. 6, pp. 2321-2326, June 2018, doi: 10.1109/TED.2017.2784185.

[61] A. Singh, S. Rajapatirana, Y. Men, V. L. Granatstein, R. L. Ives and A. J. Antolak, "Design of a multi-stage depressed collector system for 1-MW CW gyrotrons. I. Trajectory control of primary and secondary electrons in a two-stage depressed collector," *IEEE Transactions on Plasma Science*, vol. 27, no. 2, pp. 490-502, April 1999, doi: 10.1109/27.772278.

[62] M. Hruszowiec, E. F. Pliński and T. Więckowski, "The design of the gyrotron magnetic system," *2016 21st International Conference on Microwave, Radar and Wireless Communications (MIKON)*, 2016, pp. 1-3, doi: 10.1109/MIKON.2016.7492108.

[63] K. Singh, J. Itteera, R. R. Singh, S. Malhotra and D. Rathi, "Development of normal conducting cavity magnet for 42 GHz 200 kW long pulse gyrotron," *IEEE Transactions on Magnetics*, vol. 55, no. 11, pp. 1-6, Nov. 2019, Art no. 4004006, doi: 10.1109/TMAG.2019.2931864.

[64] N. Nayek, A. Naik and S. Das, "Development of face-cooled tunable double-disk sapphire window for 42-GHz 200-kW gyrotron," *IEEE Transactions on Plasma Science*, vol. 43, no. 4, pp. 1024-1028, April 2015, doi: 10.1109/TPS.2015.2403391.

[65] N. Nayek, K. Subhadra, A. Naik and S. Das, "Sapphire windows for high-power microwave and mm-wave applications," *2011 IEEE International Vacuum Electronics Conference (IVEC)*, 2011, pp. 339-340, doi: 10.1109/IVEC.2011.5747014.

[66] Y. Zhang et al., "Design and measurement of a W-band brewster window," *IEEE Microwave and Wireless Components Letters*, vol. 25, no. 12, pp. 826-828, Dec. 2015, doi: 10.1109/LMWC.2015.2495110.

[67] C. R. Donaldson, P. McElhinney, L. Zhang and W. He, "Wide-band HE_{11} mode terahertz wave windows for gyro-amplifiers," *IEEE Transactions on Terahertz Science and Technology*, vol. 6, no. 1, pp. 108-112, Jan. 2016, doi: 10.1109/TTHZ.2015.2495221.

[68] M. K. Joshi, N. Nayek, T. Tiwari and R. Bhattacharjee, "Design and analysis of overmoded RF window for high-power applications in X-band," *IEEE Transactions on Plasma Science*, vol. 48, no. 1, pp. 127-132, Jan. 2020, doi: 10.1109/TPS.2019.2956763.

[69] J. R. M. Vaughan, "Synthesis of a hollow-beam pierce gun," *IEEE Transactions on Electron Devices*, vol. 34, no. 2, pp. 468-472, Feb. 1987, doi: 10.1109/T-ED.1987.22948.

[70] Kompfner R. The invention of the traveling wave tube. San Francisco Press; 1964.

[71] Kim R, Dominski F., "ViSAR: a 235 GHz radar for airborne applications.", *2018 IEEE Radar Conference (RadarConf18)*, Oklahoma City, OK, 2018, pp. 1549–1554.

[72] Federici JF, Schulkin B, Huang F, et al., "THz imaging and sensing for security applications—explosives, weapons and drugs.", *Semicond Sci Technol.* 2005;20(7):S266–S280.

[73] Feng J, Tang Y, Gamzina D, et al., "Fabrication of 0.346 THz BWO for plasma diagnostics.", *IEEE Transactions on Electron Devices*, 8 p. March 2018.

[74] Li X, Huang X, Mathisen S, et al. "Design of 71-76 GHz double-corrugated waveguide traveling wave tube for satellite downlink.", *IEEE Trans Electron Devices*, 2018;65(6):2195–2200.

[75] V. Kesari and B. Basu, "Analysis of beam and magnetic field parameter sensitivity of a disc-loaded wideband gyro-TWT," *in IEEE Transactions on Plasma Science,* vol. 41, no. 5, pp. 1557-1561, May 2013, doi: 10.1109/TPS.2013.2256434.

[76] S. V. Mishakin, S. V. Samsonov and G. G. Denisov, "A helical-waveguide Gyro-TWT at the third cyclotron harmonic," *IEEE Transactions on Electron Devices,* vol. 62, no. 10, pp. 3387-3392, Oct. 2015, doi: 10.1109/TED.2015.2460265.

[77] D. R. Gillingham and T. M. Antonsen, "Linear theory of shot noise in harmonic gyroklystrons and gyro-TWT amplifiers," *IEEE Transactions on Plasma Science*, vol. 32, no. 3, pp. 987-993, June 2004, doi: 10.1109/TPS.2004.827583.

[78] M. Blank et al., "Development and demonstration of high-average power W-band gyro-amplifiers for radar applications," *IEEE Transactions on Plasma Science*, vol. 30, no. 3, pp. 865-875, June 2002, doi: 10.1109/TPS.2002.801658.

[79] P. M. Malouf, V. L. Granatstein, S. Y. Park, Gun-Sik Park and C. M. Armstrong, "Performance of a wideband, three-stage, mixed geometry gyrotwystron amplifier," *IEEE Transactions on Electron Devices*, vol. 42, no. 9, pp. 1681-1685, Sept. 1995, doi: 10.1109/16.405284.

[80] P. Hu et al., "Development of a 0.32-THz folded waveguide traveling wave tube," *IEEE Transactions on Electron Devices*, vol. 65, no. 6, pp. 2164-2169, June 2018, doi: 10.1109/TED.2017.2787682.

[81] M. Liao, Y. Wei, Y. Gong, J. He, W. Wang and G. Park, "A rectangular groove-loaded folded waveguide for millimeter-wave traveling wave tubes," *IEEE Transactions on Plasma Science*, vol. 38, no. 7, pp. 1574-1578, July 2010, doi: 10.1109/TPS.2010.2049866.

[82] J. He and Y. Wei, "Study of the slow-wave properties of a rectangular groove-loaded folded waveguide for millimeter traveling wave tubes," *IEEE Transactions on Plasma Science*, vol. 42, no. 1, pp. 55-61, Jan. 2014, doi: 10.1109/TPS.2013.2282612.

[83] Y. ShengMei, S. Wei, X. Ao and W. YaJun, "Analysis of higher order mode multi-beam folded waveguide TWT," *2015 IEEE International Vacuum Electronics Conference (IVEC)*, 2015, pp. 1-2, doi: 10.1109/IVEC.2015.7223849.

[84] R. Bhattacharjee, A. Srivastava and L. Christie, "Design of a W-band multi-beam folded waveguide TWT for high data-rate communication," *2019 International Conference on Intelligent Computing and Remote Sensing (ICICRS)*, 2019, pp. 1-3, doi: 10.1109/ICICRS46726.2019.9555848.

[85] Paul B. Larsen, David K. Abe, Simon J. Cooke, Baruch Levush, Thomas M. Antonsen, Jr., and Robert E. Myers, "Characterization of a Ka-band sheet-beam coupled-cavity slow-wave structure" *IEEE Transactions On Plasma Science*, Vol. 38, No. 6, June 2010, pp.1244-1254

[86] C. S. Chua, C. Zhao and S. Aditya, "Design and fabrication of a planar helix slow-wave structure for C/X -band TWT," *IEEE Transactions on Components, Packaging and Manufacturing Technology*, vol. 7, no. 10, pp. 1663-1669, Oct. 2017, doi: 10.1109/TCPMT.2017.2692303.

[87] A. Kumar M.M. and A. Sheel, "Simplified tape-helix analysis of the planar helix slow wave structure with straight-edge connections," *IEEE Transactions on Electron Devices*, vol. 65, no. 6, pp. 2280-2286, June 2018, doi: 10.1109/TED.2018.2797928.

[88] Y. Liu, H. Tian, Y. Lu and W. Shi, "Influences of diamond material on heat dissipation capabilities of helical slow wave structures," *IEEE Transactions on Electron Devices*, vol. 66, no. 12, pp. 5321-5326, Dec. 2019, doi: 10.1109/TED.2019.2945969.

[89] X. Xu et al., "Sine waveguide for 0.22-THz traveling wave tube," *IEEE Electron Device Letters*, vol. 32, no. 8, pp. 1152-1154, Aug. 2011, doi: 10.1109/LED.2011.2158060.

[90] Z. Lu, R. Wen, Z. Wang, H. Gong and Y. Gong, "Investigation of sine groove waveguide slow wave structure for terahertz traveling wave tube," *IEEE Transactions on Electron Devices*, vol. 68, no. 2, pp. 804-810, Feb. 2021, doi: 10.1109/TED.2020.3043219.

[91] L. Zhang et al., "A ridge-loaded sine waveguide for G -band traveling wave tube," *IEEE Transactions on Plasma Science*, vol. 44, no. 11, pp. 2832-2837, Nov. 2016, doi: 10.1109/TPS.2016.2605161.

[92] Huarong Gong , Qi Wang, Difu Deng, Xiang'ai Meng, Yao Dong, Jin Xu, Tao Tang, Xiaogang Su, Zhanliang Wang, Yubin Gong and Gil Travish, " Third-harmonic traveling wave tube multiplier-amplifier", *IEEE Transactions On Electron Devices*, Vol. 65, No. 6, June 2018, pp. 2189-2194

[93] Petr Makhalov and Alexey Fedotov, " Design and modeling of a slow-wave 260 GHz tripler", *IEEE Transactions On Terahertz Science And Technology*, Vol. 5, No. 6, November 2015, pp. 1048-1052

[94] C. L. Kory, M. E. Read, R. L. Ives, J. H. Booske and P. Borchard, "Design of overmoded interaction circuit for 1-kW 95-GHz TWT," *IEEE Transactions on Electron Devices*, vol. 56, no. 5, pp. 713-720, May 2009, doi: 10.1109/TED.2009.2015405.

[95] Y. Gong et al., "A 140-GHz two-beam overmoded folded-waveguide traveling wave tube," *IEEE Transactions on Plasma Science*, vol. 39, no. 3, pp. 847-851, March 2011, doi: 10.1109/TPS.2010.2100410.

[96] Vladimir L. Bratman, Alexey E. Fedotov, Petr B. Makhalov, and Vladimir N. Manuilov, "Design and numerical analysis of W-band oscillators with hollow electron beam", *IEEE Transactions On Electron Devices*, Vol. 61, No. 6, June 2014, pp. 1795-1799

[97] E. A. Myasin, M. B. Tseitlin and L. M. Nutovich, "Analysis of the electron-wave interaction in the orotron on the basis of the approximate analytic nonlinear theory," *IEEE Transactions on Electron Devices*, vol. 37, no. 12, pp. 2634-2637, Dec. 1990, doi: 10.1109/16.64545.

[98] D. E. Wortman, R. P. Leavitt and H. Dropkin, "Improved orotron performance in the 50- to 75-GHz frequency region," *IEEE Transactions on Electron Devices*, vol. 29, no. 10, pp. 1639-1640, Oct. 1982, doi: 10.1109/T-ED.1982.20930.

[99] Sergey S. Ponomarenko, Sergey A. Kishko, Viktor V. Zavertanniy, Eduard M. Khutoryan, Igor V. Lopatin, Boris P. Yefimov, and Alexei N. Kuleshov, "400-GHz continuous-wave clinotron oscillator", *IEEE Transactions On Plasma Science*, Vol. 41, No. 1, January 2013, pp.82-86

[100] Mihail V. Milcho, Viktor V. Zavertanny, Kostyantyn Ilyenko, and Anatoly S. Tishchenko, "Experimental proof-of-principle demonstration of Sub-MM clinotron-multiplier" *Proc. of 40th International Conference on Infrared, Millimeter, and Terahertz waves (IRMMW-THz)*, Year: 2015, pp.1 - 2

[101] Yurii S. Kovshov, Sergey S. Ponomarenko , Sergey A. Kishko, Eduard M. Khutoryan, and Alexei N. Kuleshov, "Numerical simulation and experimental study of Sub-THz and THz CW clinotron oscillators", *IEEE Transactions On Electron Devices*, Vol. 65, No. 6, June 2018, pp. 2177- 2182

[102] Changqing Zhang, Cunjun Ruan, Shuzhong Wang, Xiudong Yang and Ding Zhao, "The circuit design and particle-in-cell simulation for W-band high-power extended interaction klystron", *Proc. of IEEE 14th International Vacuum Electronics Conference (IVEC)*, Year: 2013, pp. 1 – 2

[103] D. Berry et al., "Practical aspects of EIK technology," *IEEE Transactions on Electron Devices*, vol. 61, no. 6, pp. 1830-1835, June 2014, doi: 10.1109/TED.2014.2302741.

[104] H. Wang, D. Zhao, Q. Xue, Z. Qu and H. Ding, "Design and simulation of high-aspect-ratio sheet beam EIK at 0.22 THz," *IEEE Transactions on Plasma Science*, vol. 49, no. 12, pp. 3811-3817, Dec. 2021, doi: 10.1109/TPS.2021.3125859.

[105] D. Zhao, W. Gu, X. Hou, G. Liu, Q. Xue and Z. Zhang, "Demonstration of a high-power Ka-band extended interaction klystron," *IEEE Transactions on Electron Devices*, vol. 67, no. 9, pp. 3788-3794, Sept. 2020, doi: 10.1109/TED.2020.3008881.

[106] C. Paoloni and M. Mineo, "Double corrugated waveguide for G-band traveling wave tubes," *IEEE Transactions on Electron Devices*, vol. 61, no. 12, pp. 4259-4263, Dec. 2014, doi: 10.1109/TED.2014.2364636

[107] Rosa Letizia, Mauro Mineo, and Claudio Paoloni, " Photonic crystal-structures for THz vacuum electron devices", *IEEE Transactions On Electron Devices*, Vol. 62, No. 1, January 2015, pp. 178-183

[108] Jason S. Hummelt, Sudheer Jawla, Elizabeth J. Kowalski, Michael A Shapiro and Richard J. Temkin, "Overmoded traveling wave tubes for mm and THz Applications" , *Proc. of 40th International Conference on Infrared, Millimeter, and Terahertz waves (IRMMW-THz)*, Year: 2015, pp. 1-2

[109] Guy Rosenzweig, Jason S. Hummelt, Michael A. Shapiro, and Richard J. Temkin, "Designs of W-band TWT amplifiers with large beam tunnels", *Proc. of IEEE International Vacuum Electronics Conference (IVEC-2016)*, Year: 2016, pp. 1 - 2

[110] Laxma Reddy Billa, Muhammad Nadeem Akram, and Xuyuan Chen, "H-plane and E-plane loaded rectangular slow-wave structure for terahertz TWT amplifier", *IEEE Transactions On Electron Devices*, Vol. 63, No. 4, April 2016, pp. 1722-1727

[111] K. L. Felch et al., "Characteristics and applications of fast-wave gyrodevices," *Proc. IEEE*, vol. 87, no. 5, pp. 752–781, May 1999.

[112] Y. V. Bykov et al., "Efficiency enhancement of gyrotron based setups for materials processing," *Proc. 34th Int. Conf. Infr., Millim.*, THz Waves, Sep. 2009, pp. 1–2.

[113] V. Srivastava, R. G. Carter, B. Ravinder, A. K. Sinha and S. N. Joshi, "Design of helix slow-wave structures for high efficiency TWTs," *IEEE Transactions on Electron Devices*, vol. 47, no. 12, pp. 2438-2443, Dec. 2000, doi: 10.1109/16.887034.

[114] X. Zhang, J. Feng, J. Cai, Y. Du, R. Dong and X. Wu, "Power enhancement in W-Band pulsed folded waveguide TWT," *IEEE Transactions on Electron Devices*, vol. 68, no. 5, pp. 2504-2508, May 2021, doi: 10.1109/TED.2021.3068692.

[115] L. R. Billa, X. Shi, M. N. Akram and X. Chen, "Improved design and microfabrication of *H* -Plane and *E* -plane loaded rectangular slow-wave structure for THz TWT amplifier," *IEEE Transactions on Electron Devices*, vol. 64, no. 5, pp. 2383-2389, May 2017, doi: 10.1109/TED.2017.2683399.

[116] R. L. Ives, L. R. Falce, G. Miram and G. Collins, "Advanced dispenser cathodes," *IEEE Transactions on Plasma Science*, vol. 40, no. 5, pp. 1299-1302, May 2012, doi: 10.1109/TPS.2011.2174386.

[117] A. K. Singh et al., "Study and development of active sintered controlled porosity dispenser cathode," *IEEE Transactions on Electron Devices*, vol. 62, no. 11, pp. 3837-3843, Nov. 2015, doi: 10.1109/TED.2015.2478970.

[118] A. Kumar, U. Singh, N. Kumar, N. Kumar, V. Vyas and A. K. Sinha, "Design of a triode magnetron injection gun for a 1-MW 170-GHz gyrotron," *IEEE Transactions on Plasma Science*, vol. 40, no. 9, pp. 2126-2132, Sept. 2012, doi: 10.1109/TPS.2012.2205710.

[119] T. Song et al., "Study on the effect of electron beam quality on a continuously frequency-tunable 250-GHz gyrotron," *IEEE Transactions on Electron Devices*, vol. 65, no. 4, pp. 1572-1577, April 2018, doi: 10.1109/TED. 2018.2809559.

[120] M. Konno et al., "Superconducting magnet system for high power gyrotron," *IEEE Transactions on Applied Superconductivity*, vol. 3, no. 1, pp. 551-554, March 1993, doi: 10.1109/77.233765.

[121] Y. Bykov et al., "Microwave source based on the 24 GHz 3 kW gyrotron with permanent magnet," *Infrared and Millimeter Waves, Conference Digest of the 2004 Joint 29th International Conference on 2004 and 12th International Conference on Terahertz Electronics, 2004.*, 2004, pp. 191-192, doi: 10.1109/ICIMW.2004.1422019.

[122] M. E. Read, R. L. Ives, J. Neilson, M. Mizuhara, D. Marsden and P. Borchard, "A THz gyrotron based on a pulse solenoid," *2009 IEEE International Vacuum Electronics Conference*, 2009, pp. 519-520, doi: 10.1109/IVELEC.2009.5193454.

[123] M. Y. Glyavin and A. G. Luchinin, "The experimental tests of THz range gyrotron with pulsed magnetic field," *2007 IEEE 34th International Conference on Plasma Science (ICOPS)*, 2007, pp. 809-809, doi: 10.1109/PPPS.2007.4346115.

[124] M. H. Beringer, S. Illy, J. Jin, S. Kern, C. Lievin and M. Thumm, "Design of major components for a 4 MW 170 GHz coaxial-cavity gyrotron," *2010 IEEE International Vacuum Electronics Conference (IVEC)*, 2010, pp. 35-36, doi: 10.1109/IVELEC.2010.5503615.

[125] C. T. Iatrou et al., "Design and experimental operation of a 165-GHz, 1.5-MW, coaxial-cavity gyrotron with axial RF output," *IEEE Transactions on Plasma Science*, vol. 25, no. 3, pp. 470-479, June 1997, doi: 10.1109/27.597262.

[126] Nusinovich, G.S., Thumm, M.K.A. Petelin, M.I. "The gyrotron at 50: historical overview"., *J Infrared Milli Terahz Waves*, 35, 325–381 (2014). https://doi.org/10.1007/s10762-014-0050-7

[127] A. Ashutosh and P. K. Jain, “Design and analysis of metallic photonic band gap cavity for a gyrotron,” *J. Microw., Optoelectron. Electromagn. Appl.*, vol. 11, no. 2, pp. 242–251, Dec. 2012.

[128] M.I. Airila, O. Dumbrajs, A. Reinfelds and U. Strautins. "Nonstationary oscillations in gyrotrons". *Physics of Plasmas*, vol. 8, no. 10, pp.4608-4612, 2001. https://doi.org/10.1063/1.1402173.

[129] K. Nowak, E. F. Plinski, T. Wieckowski, and O. Dumbrajs, “The gyrotron startup scenario in the single mode time dependent approach,” *Math. Model. Anal.*, vol. 24, no. 4, pp. 494–506, Oct. 2019.

[130] S. Fang et al., "Experimental verification of the low transmission loss of a flat-roofed sine waveguide slow-wave structure," *IEEE Electron Device Letters*, vol. 40, no. 5, pp. 808-811, May 2019, doi: 10.1109/LED.2019.2904080.

[131] L. R. Billa, M. N. Akram and X. Chen, "H-plane and E-plane loaded rectangular slow-wave structure for terahertz TWT amplifier," *IEEE Transactions on Electron Devices*, vol. 63, no. 4, pp. 1722-1727, April 2016, doi: 10.1109/TED.2016.2527824.

[132] J. H. Booske et al., "Accurate parametric modeling of folded waveguide circuits for millimeter-wave traveling wave tubes," *IEEE Transactions on Electron Devices*, vol. 52, no. 5, pp. 685-694, May 2005, doi: 10.1109/TED.2005.845798.

[133] C. L. Kory and J. A. Dayton, "Computational investigation of experimental interaction impedance obtained by perturbation for helical traveling wave tube structures," *IEEE Transactions on Electron Devices*, vol. 45, no. 9, pp. 2063-2071, Sept. 1998, doi: 10.1109/16.711375.

[134] M. P. Kirley and J. H. Booske, "Terahertz conductivity of copper surfaces," *IEEE Transactions on Terahertz Science and Technology*, vol. 5, no. 6, pp. 1012-1020, Nov. 2015, doi: 10.1109/TTHZ.2015.2468074.

[135] J. P. Calame, M. Garven, D. Lobas, R. E. Myers, F. Wood and D. K. Abe, "Broadband microwave and W-band characterization of BeO-SiC and AIN-Based lossy dielectric composites for vacuum electronics," *2006 IEEE International Vacuum Electronics Conference held Jointly with 2006 IEEE International Vacuum Electron Sources*, 2006, pp. 37-38, doi: 10.1109/IVELEC.2006.1666172.

[136] Y. Tian et al., "Investigation of ridge-loaded folded rectangular groove waveguide slow-wave structure for high-power terahertz TWT," *IEEE Transactions on Electron Devices"*, vol. 65, no. 6, pp. 2170-2176, June 2018, doi: 10.1109/TED.2018.2798059.

[137] Craig Ross Donaldson, “A W-band gyrotron backward wave oscillator with helically corrugated waveguide”, Phd. Thesis, Dept. of Physis, University of Strathclyde, Glasgow, UK, September, 2009

[138] T. W. Crowe, W. L. Bishop, D. W. Porterfield, J. L. Hesler and R. M. Weikle, "Opening the terahertz window with integrated diode circuits," *IEEE Journal of Solid-State Circuits*, vol. 40, no. 10, pp. 2104-2110, Oct. 2005, doi: 10.1109/JSSC.2005.854599.

[139] A. Baig et al., "Performance of a Nano-CNC machined 220-GHz traveling wave tube amplifier," *IEEE Transactions on Electron Devices*", vol. 64, no. 5, pp. 2390-2397, May 2017, doi: 10.1109/TED.2017.2682159.

[140] J. Zhao et al., “Scandate dispenser cathode fabrication for a highaspect-ratio high-current-density sheet beam electron gun,” *IEEE Transactions on Electron Devices*, vol. 59, no. 6, pp. 1792–1798, Jun. 2012.

[141] R. Yang et al., "Study on 1-THz sine waveguide traveling wave tube," *IEEE Transactions on Electron Devices*, vol. 68, no. 5, pp. 2509-2514, May 2021, doi: 10.1109/TED.2021.3069447.

[142] R. Letizia, M. Mineo and C. Paoloni, "Photonic crystal-coupler for sheet beam THz vacuum electron tubes," *IEEE Electron Device Letters*, vol. 37, no. 9, pp. 1227-1230, Sept. 2016, doi: 10.1109/LED.2016.2587903.